

UNIVERSITY OF KWAZULU-NATAL

**^{57}Fe Mössbauer studies of $^{57}\text{Mn}^*$
implanted III-V semiconductors InP and
InAs**

**Wendy Bonakele Dlamini
2011**

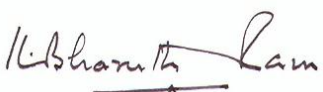
**^{57}Fe Mössbauer studies of $^{57}\text{Mn}^*$ implanted III-V
semiconductors InP and InAs**

Ms Wendy Dlamini

Submitted in fulfillment of the academic
requirements for the degree of
Master of Science in the
School of Physics
University of KwaZulu-Natal,
Durban

November, 2011

As the candidate's supervisor, I have approved this dissertation for
submission.

Signed: 

Name: Prof. K. Bharuth-Ram Date: 07.11.2011

Declaration

The work described in this dissertation was carried out at the Isotope Separator On-Line DEvice facility, ISOLDE at CERN, Geneva, Switzerland. The experiments were conducted in collaboration with scientists from Aarhus University (Denmark), University of the Witwatersrand, University of KwaZulu-Natal, Laboratorio MDM-INFM (Italy), and the Helmholtz Zentrum Berlin (Germany).

The data analysis and understanding of results are my original work and was carried out under the guidance of Professor K. Bharuth-Ram (supervisor) and Dr D. Naidoo (co-supervisor). The work of other scientists is duly acknowledged when used in the dissertation.

I declare that this dissertation has not been submitted before for any degree or diploma examination in any other tertiary institution.

Signed:.....Name:.....Date:.....

Dedicated to my late mother

Winnie T. Madela

Acknowledgements

I am grateful to my supervisor, Professor K. Bharuth-Ram for introducing me to the world of Nuclear Solid State Physics and bringing me into the ISOLDE collaboration. His insightful discussions during my research project and ideas proved to be paramount in putting my thesis together. It has been pleasing working under his supervision and I have benefited immensely from his expertise in Nuclear Solid State Physics. I also thank him for providing me with opportunities to work at CERN (European Center of Nuclear Research) and to attend the International Conference on Hyperfine Interactions on the 12th - 17th September 2010 at CERN in Geneva. This conference afforded me the opportunity to interact with other Nuclear Solid State scientists in particular, Mössbauer Spectroscopy researchers.

I would also like to express my gratitude to my co-supervisor, Dr. D. Naidoo for his guidance during measurements at ISOLDE/CERN, for his helpful comments during data analysis and for coordinating the visits to CERN for measurements at ISOLDE. His comments and relevant advice on the draft of this dissertation have helped in improving its quality. My thanks go to ISOLDE/CERN for allowing me to conduct experimental measurements in the facility.

I wish to express my sincere thanks to Mr. Hilary Masenda, for his assistance during the data analysis and for his support at all times. I thank all members of the Mössbauer Collaboration at CERN, especially Professor H.P. Gunnlaugsson and Mr. Torben MØlholt, for their assistance and helpful comments.

I extend my sincere thanks to the Department of Science and Technology for financial support for the visits to SA-CERN program.

I am grateful to my colleagues Dr. J. Govender, Dr. T. Baluki, Mr. E. Zhandire, Mr. M. Mafu and Ms. B. Keke for their support and words of encouragement. I would also like to thank my fiancé Mandla Mdlalose for his support.

Contents

ABSTRACT	XIII
CHAPTER 1	1
1.1 INTRODUCTION	1
1.1.1 Semiconductors: A brief Overview	2
1.1.2 Creation of n-type and p-type Semiconductors	3
1.1.3 Defects and impurities in solids	5
1.1.4 Growth of semiconductor materials	6
1.2 III-V SEMICONDUCTORS	8
1.2.1 Physical properties of III-V semiconductors	9
1.3 SPINTRONICS IN SEMICONDUCTORS	10
1.4 ION IMPLANTATION	12
1.4.1 Ion stopping	13
1.4.2 Range and Dose Distributions	14
1.4.3 Radiation Damage	15
1.4.4 Annealing of the Radiation Damage	16
1.4.5 Diffusion of an impurity atom in a solid	17
1.5 LITERATURE REVIEW OF MÖSSBAUER STUDIES ON III-V SEMICONDUCTORS	19
1.6 MOTIVATION FOR CURRENT WORK	20
CHAPTER 2	23
2.1 PRINCIPLES OF MÖSSBAUER SPECTROSCOPY	23

2.2 THE MÖSSBAUER EFFECT.....	24
2.2.1 Resonant emission and absorption of gamma photons.....	24
2.2.2 Spectral line shapes.....	25
2.2.3 Natural line-width of the gamma ray emitted by a nucleus.....	27
2.2.4 Recoil energy.....	27
2.2.5 Recoil-free fraction.....	30
2.3 HYPERFINE INTERACTIONS.....	32
2.3.1 Electric Monopole Interaction: Isomer Shift (δ).....	32
2.3.2 Electric Quadrupole Interaction: Quadrupole Splitting (ΔE_Q).....	35
2.3.3 Magnetic Hyperfine Interaction: Zeeman Splitting (E_M).....	38
2.3.4 Combined Quadrupole and Magnetic interactions (ΔE_{QM}).....	40
2.4 MÖSSBAUER SPECTRUM.....	41
2.4.1 Mössbauer line intensities.....	42
CHAPTER 3.....	45
3.1 EXPERIMENTAL DETAILS.....	45
3.1.1 The ISOLDE Facility at CERN.....	45
3.2 GEOMETRICAL ARRANGEMENTS OF THE MÖSSBAUER SPECTROSCOPY EXPERIMENT.....	47
3.2.1 Transmission Mössbauer Spectroscopy (TMS).....	47
3.2.2 Conversion electron Mössbauer spectroscopy (CEMS).....	48
3.3 MÖSSBAUER SPECTROSCOPY INSTRUMENTATION.....	49
3.3.1 ^{57}Fe Mössbauer Spectroscopy.....	50
3.3.2 $^{57}\text{Mn}^*$ beam production at ISOLDE.....	51

3.3.3	Experimental details of the ISOLDE Mössbauer system	52
3.4	SAMPLES AND MEASUREMENTS	55
3.4.1	Calibration of Mössbauer spectrum	56
3.5	DATA AND ERROR ANALYSIS	58
CHAPTER 4	59
4.1	RESULTS AND ANALYSIS	59
4.2	DATA ANALYSIS OF INP	59
4.2.1	Assignment of components	61
4.2.2	Discussion of hyperfine parameters	62
4.2.3	Debye temperatures (θ_D) of Fe in different lattice sites	66
4.2.4	Annealing of radiation damage	67
4.2.5	Summary of $^{57}\text{Mn}/^{57}\text{Fe}$ implanted in InP results	69
4.3	DATA ANALYSIS OF THE N-TYPE INAS AND P-TYPE INAS	69
4.3.1	Discussion of hyperfine parameters	73
4.3.2	The annealing behavior of the damage in n-type InAs and p-type InAs	78
4.4	ELECTRONIC CHARGE STATES OF IRON IN DIFFERENT SITES	80
4.5	COMPARISON OF THE DAMAGE RECOVERY	81
CHAPTER 5	86
5.1	CONCLUSION AND OUTLOOK	86

List of Figures

Figure 1.1:	Energy bands for solids: (a) Metal, (b) Semiconductor and (c) Insulator. Note that metals may have a partially filled band or a filled band which overlaps an empty one.....	2
Figure 1.2:	Energy diagrams of (a) a n-type semiconductor and (b) a p-type semiconductor..	4
Figure 1.3:	Types of intrinsic and extrinsic defects in a crystal lattice.	6
Figure 1.5:	Layer arrangement in a GMR device.....	11
Figure 1.6:	Nuclear S_n and electronic S_e components of the ion stopping energy as a function of kinetic energy.	13
Figure 1.7:	Views of the ion range. (a) Total length R and R_p is the projected range. (b) The two dimensional Gaussian distribution for the implanted ion.	14
Figure 1.8:	Ion mass effect on semiconductors surface.	16
Figure 1.9:	Three basic mechanisms of diffusion: (a) Vacancy mechanisms, where atoms exchange position with vacant lattice sites. (b) Interstitial mechanism, where atoms diffuse by hopping from one interstitial site to an adjacent one. (c) Ring mechanism, where more than two atoms may rotate together.....	18
Figure 2.1:	The nuclear transition from the excited state E_e to the ground state E_g results in the emission of a gamma ray.	25
Figure 2.2:	The statistical energy distribution of the emitted or absorbed γ -ray with natural line-width.	26
Figure 2.3:	Recoil energy E_R received by an isolated nucleus on gamma ray emission or absorption.....	28

Figure 2.4: Resonance overlaps in free atoms. The overlap of emission and absorption spectra is shaded..... 29

Figure 2.5: (a) Energy level diagram in the absence of a magnetic field or an electric field gradient. (b) Corresponding absorption line illustrating the isomer shift in the transition spectrum..... 33

Figure 2.6: The effects on the nuclear energy levels of ^{57}Fe under a nuclear quadrupole interaction due to ∇E and eQ . The resulting Mössbauer spectrum, which gives the isomer shift δ and the quadrupole splitting ΔE_Q , is also shown..... 37

Figure 2.7: The magnetic splitting of $I = \frac{1}{2}$ and $I = \frac{3}{2}$ nuclear energy levels in ^{57}Fe 39

Figure 2.8: The effect of a first-order quadrupole perturbation on a magnetic hyperfine spectrum for $I = \frac{1}{2} \rightarrow I = \frac{3}{2}$ transition in ^{57}Fe 40

Figure 2.9: Schematic representation of a source on the velocity drive unit, absorber and detector in a transmission Mössbauer geometric arrangement. 41

Figure 3.1: The schematic layout of the ISOLDE facility at CERN..... 46

Figure 3.2: Geometrical arrangements on Mössbauer spectroscopy, adopted from. 47

Figure 3.3: Internal conversion process after Mössbauer effect of ^{57}Fe nucleus. 48

Figure 3.4: Decay scheme of ^{57}Fe and parent nuclei..... 50

Figure 3.5: Beam production at ISOLDE ^{57}Mn beam-line system. After ionization, the beams are mass-separated then accelerated directly to an implantation chamber where samples are held, then collected by the gas-filled PPAC detector mounted on a Mössbauer drive unit outside the implantation chamber. 52

Figure 3.6: Experimental arrangement of the Mössbauer system at ISOLDE/CERN. A $^{57}\text{M}^+$ beam is directed to an implantation chamber in which the sample is mounted, the gas-filled PPAC detector is mounted on a Mössbauer drive unit outside the implantation chamber. The PPAC is connected to a Voltage supply and a pre-amplifier.....53

Figure 3.7: Four position sample holder mounted with annealing system.....55

Figure 3.9: Unfolded Mössbauer spectrum of enriched $\alpha\text{-Fe}$57

Figure 3.10: Example of a Folded Mössbauer spectrum of an $\alpha\text{-Fe}$ absorber.....58

Figure 4.1: Mössbauer spectra of InP obtained at temperatures indicated after $^{57}\text{Mn}^*$ implantation.60

Figure 4.2: Temperature dependence of the isomer shift obtained in ^{57}Fe Mössbauer spectra of InP after $^{57}\text{Mn}^*$ implantation, where the dash lines represent the calculated values and symbols represent the results extracted from fits.....63

Figure 4.3: Temperature dependence of the quadrupole splitting obtained in ^{57}Fe Mössbauer spectra of InP after $^{57}\text{Mn}^*$ implantation, where the dash lines represent the calculated values and symbols represent the results extracted from fits.65

Figure 4.4: Area fractions of components as a function of annealing temperature, observed in the Mössbauer spectra for InP after $^{57}\text{Mn}^*$ implantation.68

Figure 4.5: Mössbauer spectra of n-type InAs at temperatures indicated after implantation of $^{57}\text{Mn}^*$ ions.70

Figure 4.6: Mössbauer spectra of p-type InAs obtained at temperatures indicated after implantation of $^{57}\text{Mn}^*$ ions.....71

Figure 4.7: Temperature dependence of the isomer shift obtained in ^{57}Fe Mössbauer spectra of n-type InAs after $^{57}\text{Mn}^*$ implantation, where the dashed lines represent the calculated values and symbols indicates the results extracted from fits. 74

Figure 4.8: Temperature dependence of the isomer shift obtained in ^{57}Fe Mössbauer spectra of p-type InAs after $^{57}\text{Mn}^*$ implantation, where the dashed lines represent the calculated values and symbols indicates the results extracted from fits. 75

Figure 4.9: Temperature dependence of the quadrupole splitting obtained in ^{57}Fe Mössbauer spectra of n-InAs after $^{57}\text{Mn}^*$ implantation, where lines represent the calculated values and symbols represent the results extracted from fits..... 76

Figure 4.10: Temperature dependence of the quadrupole splitting obtained in ^{57}Fe Mössbauer spectra of p-InAs after $^{57}\text{Mn}^*$ implantation, where the dashed lines represent the calculated values and symbols represent the results extracted from fits. 77

Figure 4.11: Area fractions of components as a function of annealing temperature, observed in the Mössbauer spectra for n-type InAs after $^{57}\text{Mn}^*$ implantation. 78

Figure 4.12: Area fractions of components as a function of annealing temperature, observed in the Mössbauer spectra for p-type InAs after $^{57}\text{Mn}^*$ implantation. 79

Figure 4.13: The isomer shifts against the quadrupole splitting values for each spectral component obtained from the Mössbauer spectra for InP, n-type InAs and p-type InAs, modified from the Mössbauer data. 80

Figure 4.14: Area fractions of Fe_D component as a function of annealing temperature, observed in the Mössbauer spectra for InP, n-type InAs and p-type InAs after $^{57}\text{Mn}^*$ implantation. 82

Figure 4.15: Area fractions of Fe_X components as a function of annealing temperature, observed in the Mössbauer spectra for InP, n-type InAs and p-type InAs after $^{57}Mn^*$ implantation..... 83

Figure 4.16: Area fractions of Fe_S components as a function of annealing temperature, observed in the Mössbauer spectra for InP, n-type InAs and p-type InAs after $^{57}Mn^*$ implantation. 84

List of Tables

Table 1.1: Physical properties of the III-V semiconductors at 300 K compared with some of the group IV elemental semiconductors. 8

Table 2.1: Relative probabilities for a dipole $\frac{3}{2}, \frac{1}{2}$ transition. C is calculated by $\left\langle \frac{1}{2} 1 - m_1 \left| \frac{3}{2} m_2 \right. \right\rangle$ converted by means of the relationship

$$\left\langle \frac{1}{2} 1 - m_1 \left| \frac{3}{2} m_2 \right. \right\rangle = (-)^{\frac{1}{2} m_1} \sqrt{\left\langle \frac{3}{2} \frac{1}{2} m_2 m_1 \left| 1 m \right. \right\rangle}; C^2 \text{ and } \Theta$$

are normalized angular independent and dependent terms, and 90^0 and 0^0 are relative intensity angles with respect to the principal axis 44

Table 4.1: Hyperfine parameters: isomer shift (δ) and quadrupole splitting (ΔE_Q), the Gaussian broadening (σ) obtained at room temperature from a simultaneous analysis of the spectra for InP, and the extracted Debye temperatures (θ_D) for the different lattice sites and errors in parentheses. 61

Table 4.2: Hyperfine parameters isomer shift (δ) and quadrupole splitting (ΔE_Q), the Gaussian broadening (σ) obtained at room temperature from a simultaneous analysis of the spectra for n- and p-type InAs, and the extracted Debye temperatures (θ_D) for the different lattice sites and errors in parentheses. 72

Abstract

III-V compound semiconductors such as Gallium Arsenide, Indium Phosphide as well as Indium Arsenide have recently demonstrated the capability of applications in high speed semiconductor devices compared to those made from Silicon. As a result, III-V compound semiconductors have drawn attention of material researchers, in particular in understanding the effects that may occur during manufacturing of these devices.

Optical and electrical properties of a device may alter when a foreign atom is introduced during the manufacturing of the device. However, the foreign atom may also lead to the formation of lattice disorder (defects). A convenient way of introducing impurity atoms into a substrate and tailoring their functionality for particular applications is by ion implantation. Mössbauer spectroscopy is a useful technique usually utilized for understanding site location of the impurity atoms in a lattice and the formation of defect complexes. The focus of this dissertation is the study of lattice location of ion implanted $^{57}\text{Mn}/^{57}\text{Fe}$ ions in the III-V semiconductors InP, n-type InAs and p type InAs, and the annealing of implantation induced lattice damage in these samples.

^{57}Fe Mössbauer spectroscopy studies have been conducted on III-V semiconductors InP, n-type InAs and p-type InAs with the ^{57}Fe Mössbauer state being populated following the implantation of radioactive $^{57}\text{Mn}^+$ ions which has the advantage that extremely low fluence implantations are sufficient to give data with good statistics. The $^{57}\text{Mn}^+$ ions were accelerated to 60 keV at the ISOLDE/CERN facility and implanted with fluences of up to 2×10^{12} ions/cm² into single crystal samples which were held at 300–700 K in an implantation chamber. β -decay of the Mn^+ imparts an average recoil energy of 40 keV to the daughter $^{57*}\text{Fe}$ which are then re-distributed onto interstitial and/or substitutional sites, or trapped in defect complexes and damage sites. The Mössbauer spectra were collected with a light-weight parallel plate avalanche counter, with ^{57}Fe enriched stainless steel electrodes, mounted on a conventional drive unit outside the implantation

chamber. The spectra were analyzed with the Mössbauer fitting code VINDA which allowed for simultaneous fits of the set of spectra for each sample collected at different temperatures.

Acceptable fits to the Mössbauer spectra of the InP, n-type InAs and p-type InAs samples required three components: an asymmetric doublet attributed to Fe atoms in implantation induced damaged environments, a single line assigned to Fe on substitutional In sites, and a weak symmetric doublet assigned to impurity-vacancy complexes. In InP there is already an appreciable substitutional Fe (Fe_S) fraction on implantation at room temperature; while in the InAs samples Fe_S only becomes significant above 400 K. In all samples, the asymmetric doublet dominates the spectra below 400 K. Implantation damage, however, anneals quite rapidly and at high temperatures (above 400 K), the single line due to Fe_S dominates the spectra while the Fe-defect complex dissociates at 500 K. The implantation induced damage is observed to anneal fast in the arsenide samples compared to the phosphide sample. The slow annealing of the damage in InP was supported by the higher Debye temperature (290 K) extracted from the temperature dependence of the site population for the damage site in InP compared with InAs (194 K and 200 K for n-type and p-type, respectively).

Variations in the isomer shift and quadrupole splitting for the damage site in InP at high temperatures (above 400 K) suggest structural changes in the neighborhood of the ^{57}Fe probe. Furthermore, the isomer shifts of the spectral components were consistent with near trivalent state and fully trivalent state i.e., Fe^{3+} with d^5 electron configuration for Fe ions in the damage site and at the substitutional (In) site, respectively. The impurity Fe atoms associated with vacancies are identified to be in the Fe^{2+} state with a d^6 electron configuration.

CHAPTER 1

1.1 Introduction

Applications of semiconductors in the electronic industry have grown rapidly over the past several decades. At present, the majority of applications of semiconductors are based on silicon. However, compound semiconductors such as Gallium Arsenide (GaAs), Indium Phosphide (InP) and Indium Antimonide (InSb) have been demonstrated to be suitable for producing semiconductor devices operating at high speed and high frequency [1-3]. As a result, they have drawn considerable research attention.

This dissertation presents the results of ^{57}Fe Mössbauer measurements on InP and n- and p-type InAs. The experiments were conducted at the on-line radioactive ion beam facility ISOLDE at CERN, Geneva, in the Mössbauer collaboration of which my two supervisors are active members.

In this chapter, a brief overview of semiconductors is presented, highlighting details of selected charge donor and acceptor states, of defects and impurities in solids, and of the growth techniques of semiconductors. Then a discussion on compound trivalent-pentavalent (III-V) semiconductors and their physical properties is given, together with a description of ions that can be implanted in semiconductors and their effects, and concludes with a brief motivation for the current study. This is followed, in Chapter 2, by a discussion of the principles of Mössbauer spectroscopy, focusing on the parameters that are extracted from the data and the information they reveal about the system under study. The details of the experimental set up at the ISOLDE/CERN facility are presented in Chapter 3 and some of their unique features are highlighted. The Mössbauer spectra, details of the data analysis procedures, and the results are presented in Chapter 4, and finally the conclusions are discussed in Chapter 5.

1.1.1 Semiconductors: A brief Overview

Valence electrons in metals are loosely bound to their atoms so that even a very small electric field is sufficient to accelerate them and enable conduction. As shown in Figure 1.1(a), in metals (good conductors), the valence band and conduction band overlap, while in semiconductors these are separated by a gap called the *energy gap* or *band gap*, E_g . Bonds between atoms in *semiconductors* are moderately strong. On the other hand, atomic bonds in *insulators* are strong, thus large amounts of energy is needed to free electrons, resulting in valence and conduction bands being separated by a large gap, see Figure 1.1 (c).

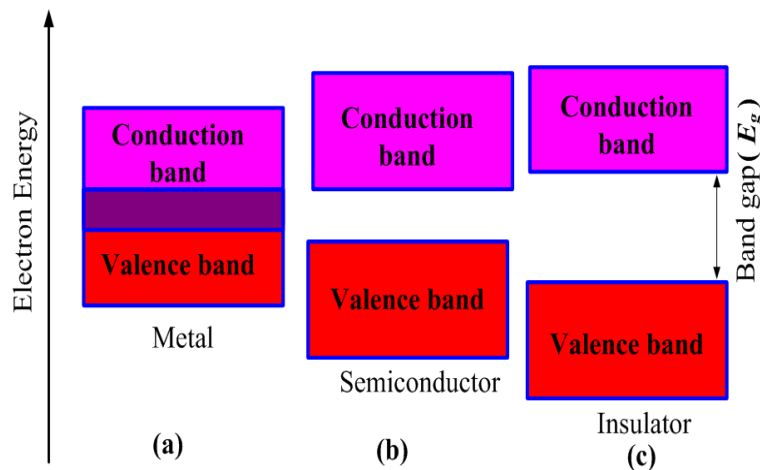


Figure 1.1: Energy bands for solids: (a) Metal, (b) Semiconductor and (c) Insulator. Note that metals may have a partially filled band or a filled band which overlaps an empty one.

In semiconductors, the energy gap between energy bands is relatively small as shown in Figure 1.1(b). At $T = 0$ K all electrons are bound to their atoms; hence there are no free electrons that would enable conduction. In terms of the energy band picture, the valence band is fully occupied and the conduction band is completely empty. A significant amount of energy (equal to E_g or higher) has to be transferred to electrons at the valence band in order for electrons to jump

from the valence band to the conduction band. When this is achieved, the valence band now contains *holes*, where some states in that band are empty, and the conduction band is no longer totally empty. Furthermore, both bands can contribute to the conduction of current, but the conductivity is low. This is because the number of unoccupied states in the valence band and the number of occupied states in the conduction band are few.

In group VI semiconductors each atom is bound to four neighbouring atoms and share valence electrons, forming covalent bonds. If $T > 0$ K, lattice vibrations can cause the covalent bonds to break.

In group III-V semiconductors, the bonding is also predominantly covalent. However, there exists a small but not insignificant ionic contribution due to a reduction in the electron density around the III⁺ ion (and a corresponding increase around the V ion) [4]. Broken bonds result in free electrons, hence enabling conduction. Valence electrons in neighboring bonds can jump into the position of a missing electron, thus the flow of electric current is produced. After some time the free electron will jump into another broken bond in the crystal. This process is called *electron-hole recombination*.

1.1.2 Creation of n-type and p-type Semiconductors

In pure semiconductors, free charge carriers are generated by the process of electron-hole generation. Therefore, the number of holes is the same as the number of free electrons. This kind of semiconductor is called an *intrinsic* semiconductor. The doped semiconductor in which a foreign atom (dopant) is introduced is referred to as an *extrinsic* semiconductor because now the optical and electrical properties depend strongly upon the impurity content.

The impurity atoms that cause the increase of electron concentration in an intrinsic semiconductor are called *donors* and a semiconductor in which the concentration of electrons is higher than the concentration of holes is said to be an *n-type* semiconductor. The extra electron is constrained to remain in the neighbourhood of the impurity atom as it is attracted by the extra positive charge on the nucleus. A very small energy will be sufficient to accelerate this electron,

and when it leaves, the donor atom becomes positively charged. In the energy band diagram, the presence of a donor atom can be represented by discrete states within the energy gap as shown in Figure 1.2(a). The donor states are very close to the conduction band.

When the impurity atom does not have enough electrons to complete covalent bonds with host semiconductor atoms, such impurity is referred to as an *acceptor*. An impurity atom will bind with an electron that may jump from the valence band into the conduction band. Hence, it captures an electron and becomes negatively charged. Therefore, an acceptor impurity produces ionized states within the energy gap very close to the valence band as shown in Figure 1.2 (b). The number of holes is higher than the number of electrons and the semiconductor is said to be a *p-type* semiconductor.

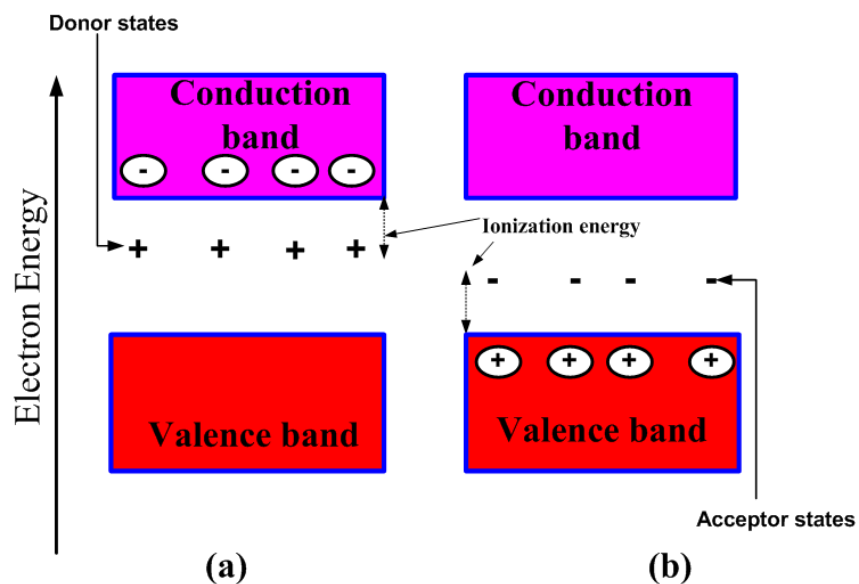


Figure 1.2: Energy diagrams of (a) a n-type semiconductor and (b) a p-type semiconductor.

In compound semiconductors, donor impurities are elements with valence electrons lower than that of the element they substitute. Acceptor impurities are elements with valence lower than that they substitute. However, in trivalent and pentavalent elements (III-

V compound semiconductors), a tetravalent dopant (for example silicon in gallium arsenide) can be both a donor (if it substitutes a trivalent element) and acceptor (if substitutes a pentavalent element).

1.1.3 Defects and impurities in solids

The crystal structure of all real crystals is imperfect. The imperfection in the regular periodic arrangement of atoms in a crystal is called a *defect*. Defects even in very small concentrations have dramatic impacts on the properties of materials. The most common imperfections in crystals are point defects. Point defects may occur in pure materials (intrinsic defects) or due to impurity atoms (extrinsic defects). Intrinsic defects do not change the overall composition of a material while the extrinsic defects introduce impurity atoms into the system.

The two well known types of intrinsic defects are the vacancy *defect*, due to a missing atom in a crystal lattice site and the *interstitial defect* where an atom of the host material or an impurity atom is squeezed into the space between the atoms of the host material (known as interstitial site).

In the case of an impurity atom present in a crystal lattice, it may be located at normal lattice sites when it forms a *substitutional impurity*. It may also be located at an interstitial site, forming an *interstitial impurity*. However, impurity atoms may also be embedded in defect complexes in the lattice resulting in, for example, *interstitial-vacancy* or *substitutional-vacancy* complexes [5]. The different lattice defects are illustrated in Figure 1.3.

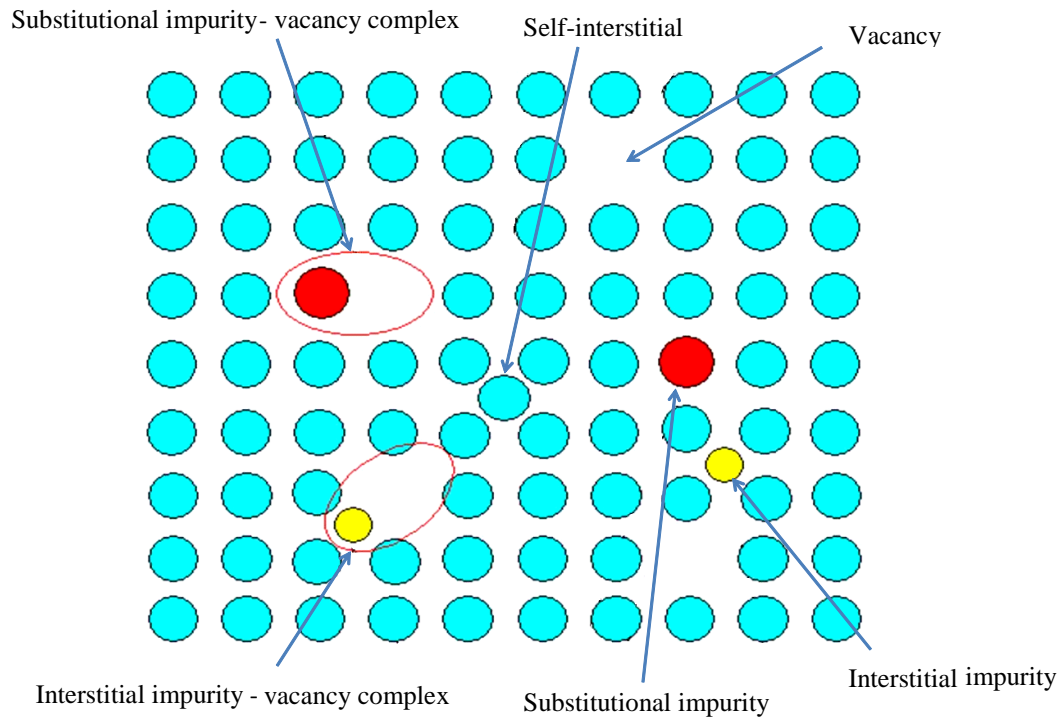


Figure 1.3: Types of intrinsic and extrinsic defects in a crystal lattice.

The introduction of controlled amounts of impurity atoms can alter the electrical and optical properties of semiconductors. The technique of adding impurity atoms to a semiconductor is known as *doping*. Doping can be achieved either during the growth of a single crystalline semiconductor, or by impurity diffusion or by ion implantation.

1.1.4 Growth of semiconductor materials

Semiconductors can be grown by two methods known as *melt* and *epitaxial* growth [5]. A well-known technique for growth of a single crystal is a Czochralski (a melt method) process [5]. This process was discovered by a Polish scientist Jan Czochralski in 1916. In the Czochralski's method, a single crystal material (known as seed) is brought into contact with the surface of the

same material in the liquid phase [6]. The seed is then slowly withdrawn from the melt while it is rotated about the growth axis. The rotation of the seed provides a slight stirring action to the melt, resulting in a more uniform temperature. The single crystal (called boules) is then produced along the plane between the solid and liquid interface. Controlled amounts of impurities may be added to the melt so that the grown semiconductor is intentionally doped with specific concentration of impurity atoms. Both n-type and p-type semiconductors may be grown by such methods.

The Czochralski method is not applicable in the case of compound semiconductors where the melting point of one of the elements is lower than that of the desired semiconductor. Furthermore, the temperature of the melt is kept below the melting temperature of the substrate to ensure that the substrate does not disintegrate. In such a case an epitaxial growth process may be used, in which a thin single crystal layer of a material is grown on the surface of a single crystal substrate. Epitaxial growth takes place far from the melting temperature of the substrate. The epitaxial layer may be grown on a substrate of the same material (InP layer on InP substrate); this technique is referred to as the homoepitaxy process. When the grown layer and substrate are not the same but their crystal structures are very similar (InGaAs layer on InP substrate) the process is referred to as heteroepitaxy.

The similarities in crystal structures promote the growth of single crystals and avoid large numbers of defects that may result at the epitaxial layer-substrate interface. The process of epitaxial growth uses *chemical vapour-phase deposition (CVD)*, *liquid-phase epitaxy (LPE)* or *molecular beam epitaxy (MBE)* techniques. The controlled deposition of atoms onto the surface of a substrate from a chemical vapour containing the desired material is used in the CVD method. This technique allows great flexibility in the fabrication of semiconductors. The LPE technique uses a liquid solution for growing a crystalline epitaxial semiconducting layer on a substrate [7, 8].

A third method of growing a semiconductor is molecular beam epitaxy (MBE). In the MBE technique, a beam of atoms or molecules is directed on the growth surface without any prior interference or interaction (in a vacuum). Semiconductor or dopant atoms are evaporated onto

the surface of the substrate. This technique is utilized in growth of complex ternary compounds such as GaInAs [8].

1.2 III-V Semiconductors

The III-V semiconductor is a compound which comprises of one element from group III and the other from group V of the periodic table. Examples of elementary and III-V compound semiconductors are listed in Table 1.1, where their properties are compared with *Silicon* (Si) and *Germanium* (Ge).

Table 1.1: Physical properties of the III-V semiconductors at 300 K compared with some of the group IV elemental semiconductors [6, 9].

Semiconductor	Gap's type	Energy gap (eV) at 300 K	Effective mass m_e/m_0	Lattice constant (\AA)
C	Indirect	5.50	0.99	3.56683
Si	Indirect	1.12	0.43	5.42
Ge	Indirect	0.74	0.60	5.62
GaP	Indirect	2.25	0.35	5.45
GaAs	Direct	1.34	0.066	5.63
GaSb	Direct	0.70	0.047	6.09593
InP	Direct	1.27	0.073	5.86875
InAs	Direct	0.33	0.026	6.05838
InSb	Direct	0.18	0.015	6.48

III-V semiconductor materials have narrow direct energy gaps, which allow more efficient electronic transitions than indirect energy gap materials. They also have higher recombination

efficiency, which make them suitable for optoelectronic applications [10, 11]. Moreover, III-V semiconductors have higher electron mobilities than group V semiconductors, which result from their low effective mass. As a result, III-V semiconductors are utilized in the manufacturing of semiconductor devices that emit light efficiently and operate at exceptionally high frequencies.

1.2.1 Physical properties of III-V semiconductors

III-V semiconductors are classified as Arsenides, Phosphides, Antimonides and Nitrides. Most of the III-V semiconductors have a zinc-blende lattice structure, which is similar to the diamond lattice, except that one sublattice consists of group III atoms and the other group V atoms. In the case of III-V semiconductors, two face centered sublattices are translated by $\frac{3}{4}$ of the distance along the diagonal direction. The cell of the zinc-blend lattice structure is formed by two atoms, one group III element and the other group V element, as shown in Figure 1.3 below.

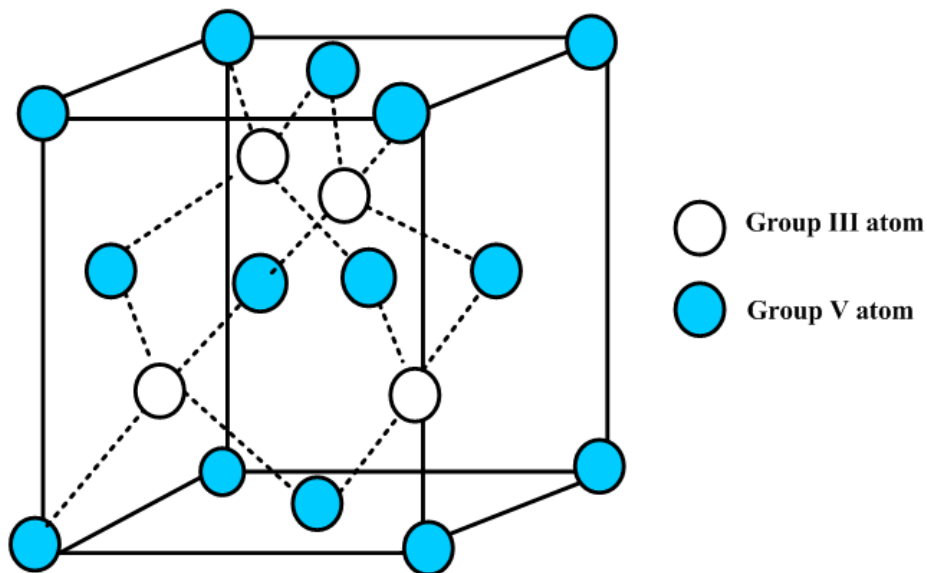


Figure 1.4: Face Centred Cubic (FCC) lattice structure where the unit cell is formed by two atoms in $(0, 0, 0)$ and in $(\frac{1}{4}, \frac{1}{4}, \frac{1}{4})$ positions.

Most of the III-V semiconductors have very high electron mobilities, which arise from their direct energy gap, as shown in Table 1.1. As a result, they are used in the production of high frequency devices. InAs and InSb are very suitable semiconductors for producing High Electron Mobility Transistors (HEMT). This is due to their higher electron mobility compared with other compounds. These materials also offer the promise of being able to access the mid- and far-infrared wavelength regions and should provide the generation of LEDs, laser and photo detectors for applications such as gas sensors, in molecular spectroscopy, and in thermal imaging and thermo-photovoltaic cells [12]. The narrow energy gaps in InAs and InSb also make them excellent materials for the formation of low resistance contacts. The low resistance ohmic contact reduces thermal dissipation, which is needed for the fabrication of very small devices.

The III-V semiconductors, InAs and InP, investigated in the present study, are utilized in producing optoelectronic devices due to their direct energy gap type, and have also demonstrated applications in fast transistors and in spintronics [13, 14]. InAs is also used for producing photovoltaic photodiodes and infrared detectors (for wavelength ranging from 1 μm to 3.8 μm) [15].

1.3 Spintronics in Semiconductors

Conventional electronic devices ignore the spin property of the electron and depend strictly on the transport characteristics of their electric charge. However, the ability to utilize the spin degree of freedom of the electron provides new effects, new capabilities and new functionalities, leading to the development of a technology called *spintronics*. Spintronics is a new branch of electronics, which is based on the study of the role played by electron spin in solid-state materials. Spin is a quantum property, which is closely related to magnetism, thus spintronics is regarded as exploiting the quantum effect. As a result spintronics is sometimes called *magneto-electronics*. All spintronic devices operate in a similar way, where information is stored in the particular spin orientation (up or down) of the charge carrier. The spins being attached to mobile electrons carry the information along a conducting path and the information is read at the terminal.

There are several advantages of spintronic devices such as; long lifetime of spin orientation (nanosecond), greater data processing speed, and lower power consumption, smaller sized chip. In addition data remain encoded even when the power is switched off (no-volatility), and binary spin polarization offers the possibility of applications in quantum computers.

The first spintronic effect was discovered in 1988, in a phenomenon called *Giant Magnetoresistance* (GMR) [16]. A GMR device is made out of at least two magnetic layers separated by a non-magnetic layer, as illustrated in Figure 1.5.

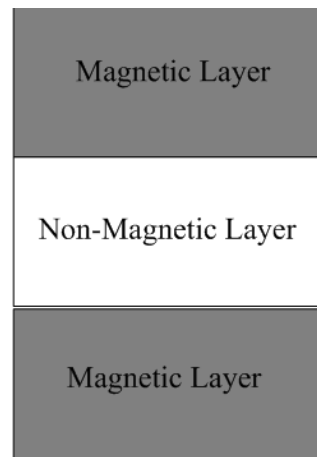


Figure 1.5: Layer arrangement in a GMR device.

A measurement of resistance of the device is used in the detection of a magnetic field. The non-magnetic material is sandwiched between two magnetic plates. GMR is a result of spin-up and spin-down electrons experiencing different resistances when passing through a magnetic layer. It is a useful tool for the detection of extremely small magnetic fields. GMR device is a very powerful spintronic device, which operates in the terahertz range. It is most commonly employed in recording devices such as computer hard disc drives (where the magnetic information on the disc is read) and in field sensors and *Magnetic Random Access Memories* (MRAM) [17].

Dilute ferromagnetic semiconductors including Mn doped III-V semiconductors [18] and materials with spin, are mostly used in the construction of spintronic devices. The combination of both semiconducting and magnetic properties offers multiple functionalities.

1.4 Ion Implantation

A versatile procedure for incorporating dopant atoms in semiconductors is *ion implantation*. The ion implantation process has several advantages: the concentration of dopant and their lateral and depth distributions can be precisely controlled. Furthermore, the implantation process is not limited by thermal equilibrium. Another advantage of ion implantation is that the temperature of the substrate can be accurately controlled which limits the diffusion of the implanted species. However, lattice damage is created during implantation; hence post implantation thermal treatment is required for annealing implantation damage.

During the implantation, impurity atoms are accelerated to energies from a few keV to several hundred keV and implanted into a crystal [19]. These high energy atoms enter the crystal lattice and lose their energy by collision with the lattice atoms before they come to rest at some distance below the surface of the substrate. Thus, high concentrations of defects (*vacancies*, *interstitials* even *amorphous* layers) are created. The adjustment of the acceleration energy controls the average depth of the implanted atoms, while their lateral profile may be defined by the use of appropriate masks. If the incident energy exceeds the displacement energy of the lattice atoms, a number of displaced atoms are created resulting in the production of vacancies and interstitial atoms. If the lattice atom receives energy, which is less than the displacement energy the host atom will not displace any additional atoms.

1.4.1 Ion stopping

As the ions being implanted impinge onto the substrate target, they undergo several collisions with the host atoms until they finally come to rest at some depth [20]. This energy lost per unit path length is called the *stopping power*. The overall stopping power of a target to stop an ion is given by

$$-\frac{dE}{dx} = N [S_n(E) + S_e(E)], \quad (1.1)$$

where N is the number of implanted ions, $S_n(E)$ is the nuclear stopping power which results from the collisions with the target atoms, and $S_e(E)$ is the electronic stopping power resulting from the interaction of the implanted ions with bound and free electrons of the target atoms. For heavy ions and at lower energies, nuclear stopping is the more important process [21]. However, the electronic stopping is important for lighter ions and at higher energies. Figure 1.6 shows the relative distribution of stopping powers over a wide ion energy range. More host atoms are displaced in the energy range where nuclear stopping dominates.

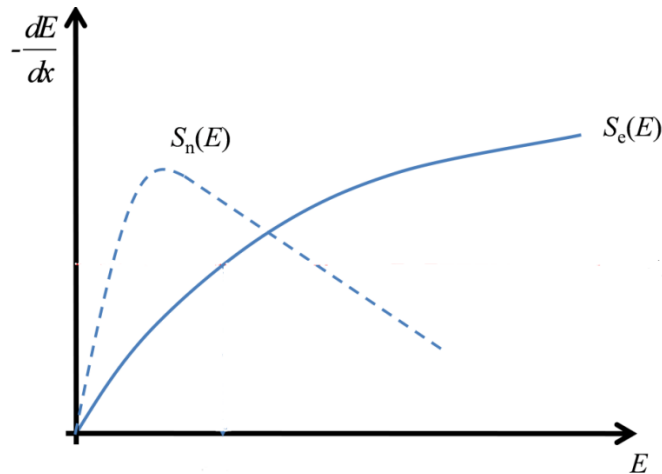


Figure 1.6: Nuclear S_n and electronic S_e components of the ion stopping energy as a function of kinetic energy [22].

1.4.2 Range and Dose Distributions

An energetic ion implanted in a substrate travels in a random path as it penetrates the target before it comes to rest; see Figure 1.7 (a). The depth length travelled by implanted ions is defined by its average range (R_p) which is sometimes referred to as the *projected range*. A good estimate of the range and distribution of implanted ions is given by the Lindhard, Scharf and Schiott (LSS) [21, 23] formulation, which gives the projected range.

$$R_p = \frac{1}{E_0} \int_{E_i}^0 \frac{dE}{(S_n(E) + S_e(E))}, \quad (1.2)$$

where E_i is the implantation energy.

The projected range R_p depends on the implantation energy, the implantation angle, and the stopping power of the substrate. R_p is composed of both lateral and vertical motions. As a result, heavier ions that have low velocity come to rest closer to the surface, while lighter ions penetrate deeper.

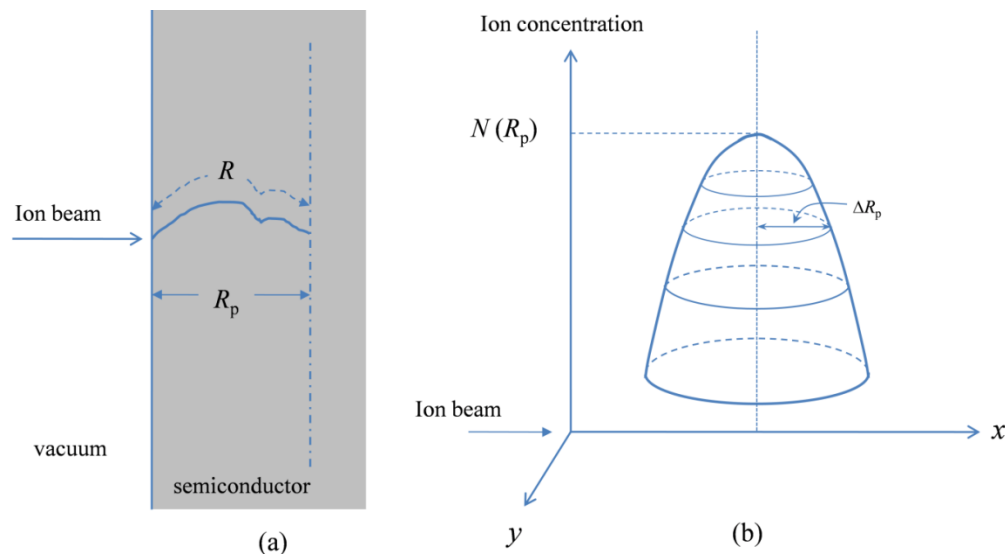


Figure 1.7: Views of the ion range. (a) Total length R and R_p is the projected range. (b) The two dimensional Gaussian distribution for the implanted ion [22].

Figure 1.7 (b) shows the distribution of the implanted ions $N(x)$ that is approximated as a Gaussian distribution, centered at the projected range R_p with a standard deviation (ΔR_p) and symmetrical on either side of R_p . The implanted ion distribution gives information about the concentration of ions at varying depth from the surface of the substrate. On this approximation the distribution of the implanted ions is determined by

$$N(x) = N_p \exp\left[-\frac{(x - R_p)^2}{2(\Delta R_p)^2}\right], \quad (1.3)$$

where N_p is the peak concentration at $x = R_p$ and can be related to the total number of ions implanted and the standard deviation by

$$N_p = \frac{Q}{\sqrt{2\pi}\Delta R_p}, \quad (1.4)$$

where

$$Q = \frac{1}{q} \int_0^t J dt = \frac{Jt}{q} = \frac{It}{qA}. \quad (1.5)$$

Here J is the ion current density, q is the charge of the implanted ions, A is the impact area and t the implantation time.

1.4.3 Radiation Damage

As the implanted ions undergo a series of collisions with the host atoms, the target atoms are disturbed from their lattice sites. The disturbance of host atoms is regarded as the lattice damage. The lattice damage depends on the mass and atomic number of the implanted ion, the fluence of ions implanted, and the energy transferred to the target atoms. The heavier implanted ions and higher ion fluencies produce more defects. If the implantation fluence is high, the crystal

structure becomes highly disordered and small amorphized pockets may be formed in the lattice. At very high fluences, complete amorphization of the crystalline material may result.

Figure 1.8 illustrates the effect of the mass of the implanted ion on a semiconductor [23]. This figure shows a light ion that moves deeper into the substrate, and the damage caused spreads over a larger volume and range R_p . Hence, the implantation damage is low. A heavy ion loses more energy per collision, moves shorter distance and displaces the host atoms more. As a result, the implantation damage is large for a heavy ion implantation. If the implantation damage is very high an amorphous layer is found near R_p .

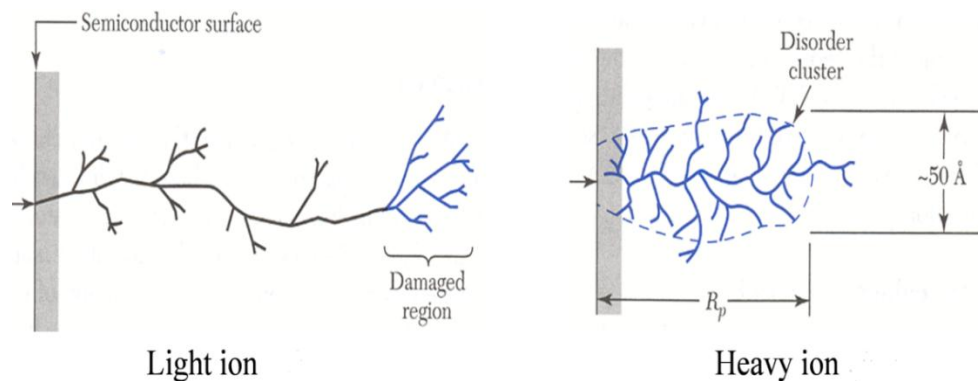


Figure 1.8: Ion mass effect on semiconductors surface [23].

1.4.4 Annealing of the Radiation Damage

The lattice damage is usually undesired because it changes the electrical characteristics of the target material. The change in electrical characteristics involves an increase in the resistivity of a target material. Therefore, ion implantation is usually followed by laser or thermal annealing processes to anneal or repair the lattice damage.

Annealing is a process to restore the ion implanted substrate to its pre-implanted condition. During the annealing process vacancies and self-interstitial recombine as the annealing temperature increases. The thermal treatment also serves to locate the implanted ions on good

lattice sites where they are electrically active. In some cases, the higher temperatures drive the implanted ions into complexes with vacancies where they show magnetic behavior [24].

In some cases, an amorphous layer is created at lower temperatures below 72°C [25], and restored to a crystalline state at latter stages. The re-crystallization of the amorphous layers increases with an increase in annealing temperature. However, the rate of re-crystallization depends on the Debye temperature of the host material, crystal orientation and the implanted impurities. If implanted impurity atoms form strong bonds with the target atoms, then the re-crystallization takes place at a slow rate. The healing of the implantation damage takes place even when the implantation is ongoing, because the annealing temperature applied during the implantation causes point defects to be more mobile.

1.4.5 Diffusion of an impurity atom in a solid

An atom in a substrate may diffuse via three processes: vacancy mechanism, interstitial mechanism, and a ‘ring’ mechanism. The three basic mechanisms of diffusion are illustrated in Figure 1.9. The vacancy mechanism involves the movement of a lattice atom to the adjacent vacant site. The atom moves in the opposite direction to the movement of the vacancy and the diffusion dominates for large vacancy concentrations. Both self and impurity diffusion may occur by this mechanism.

In interstitial diffusion the atoms move through the lattice by hopping from one interstitial site to the next. Interstitial atoms are usually smaller and thus are more mobile. Interstitial diffusion occurs much more rapidly than vacancy diffusion, as there are more interstitial sites than vacancies in a real lattice. The impurity atom can move rapidly from interstitial site to interstitial site until it reaches a vacancy and thus becomes a substitutional atom.

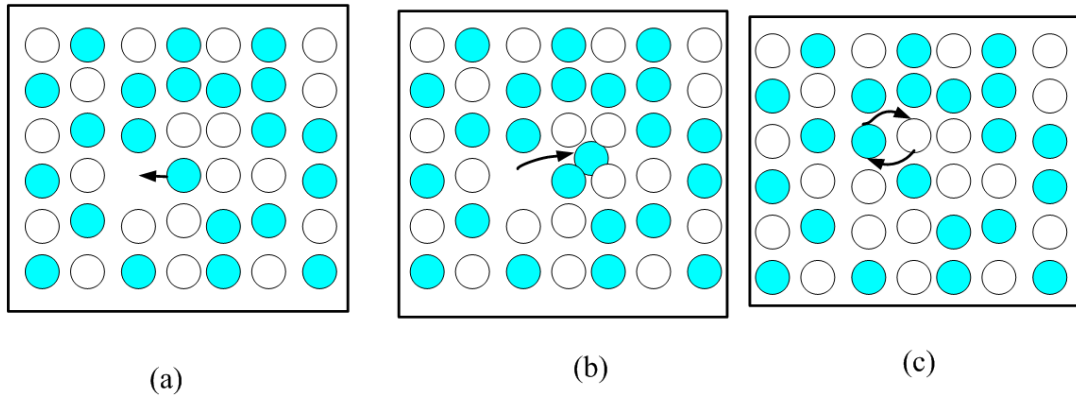


Figure 1.9: Three basic mechanisms of diffusion: (a) Vacancy mechanisms, where atoms exchange position with vacant lattice sites. (b) Interstitial mechanism, where atoms diffuse by hopping from one interstitial site to an adjacent one. (c) Ring mechanism, where more than two atoms may rotate together.

The ring mechanism involves the rotation of two adjacent atoms, which is most unlikely in ionic bounded crystals where cations and anions are adjacent to each other.

The temperature dependence of the diffusion of an atom through a crystal is assumed to follow an Arrhenius behavior [9, 26], and is described by

$$D = D_0 \exp\left[-\frac{E_0}{k_B T}\right], \quad (1.6)$$

where D is the diffusion coefficient, D_0 is the diffusion constant, E_0 is the activation energy, k_B is Boltzmann constant and T is the absolute temperature.

1.5 Literature review of Mössbauer studies on III-V semiconductors

An early investigation of the lattice site location of heavy ions implanted in InP was conducted by Damgaard *et al.* [27]. Two different radioactive isotopes ^{119}In and ^{119}Sb which populate the 24 keV Mössbauer level of ^{119}Sn were implanted into InP. After the implantation of the ^{119}Sb isotope, a single line component with an isomer shift of $1.84(3) \text{ mm}\cdot\text{s}^{-1}$ was observed and assigned to Sn atoms found on substitutional P site. This component dominated the spectrum upon annealing at 350°C . A second single line component with an isomer shift of $2.56(5) \text{ mm}\cdot\text{s}^{-1}$ was observed which nearly vanished completely upon annealing at 350°C . This component was assigned to Sn on P site, but in Sn-vacancy complexes.

Similar spectral components were also observed after the implantation of radioactive ^{119}In isotope. However, the single line with an isomer shift of $1.66(1) \text{ mm}\cdot\text{s}^{-1}$ was assigned to Sn on In site. It dominated the spectrum after annealing at 250°C . Another line with an isomer shift of $2.66 \text{ mm}\cdot\text{s}^{-1}$ was observed to anneal at 250°C and assigned to Sn atoms on In site associated with vacancies. The annealing of Sn-vacancy complexes resulted in an increase of the respective substitutional fractions. This annealing behavior suggested the annealing was due to the dissociation of the impurity-vacancy complexes. Similar results were reported for Sn implanted on InP [28-30].

From the temperature dependence of the intensity of the spectral components, the Debye temperatures of the Sn atoms on the two different substitutional sites were deduced as $184(5) \text{ K}$ and $203(8) \text{ K}$ for the P and In sites, respectively [27]. These Debye temperatures are in agreement with values of $186(10) \text{ K}$ and $202(6) \text{ K}$ for Sn on P and In sites, respectively deduced earlier by Nielsen *et al.* [31]. The Debye temperatures of $156(15) \text{ K}$ and $168(14) \text{ K}$ for Sn-vacancy complexes formed after ^{119}Sb and ^{119}In implantations, respectively were close to each other. The large values of isomer shifts and lower Debye temperatures for the Sn-vacancy complexes were attributed to impurity-multivacancy complexes in comparison with impurity-monovacancy pairs.

The annealing of the implantation damage after ion implantation of ^{111}Cd and ^{111}In in GaAs and InP, respectively, was investigated by Pfeiffer *et al.* [32] using the *Perturbed Angular Correlation* (PAC) technique. Their results revealed two different annealing stages, the first around 280 K assigned to the annealing of the associated defects. The second annealing stage was found at temperatures above 500 K in GaAs and was associated with the diffusion of impurity atoms. The first annealing stage occurred at a slightly higher temperature (above 300 K) in InP than in GaAs.

A limited amount of research on implantation of ^{57}Mn in III-V semiconductors has been reported thus far. However, Gunnlaugsson *et al.* [33] reported on the behavior of radiation damage created in Silicon based materials by ion implantation of radioactive $^{57}\text{Mn}^*$ ions between 77 K and 500 K. Three spectral components assigned to damage, interstitial and substitutional sites were observed in the temperatures range 77 - 300 K. However, the interstitial component was not observed above room temperature where the substitutional and damage components were dominant. The large quadrupole splitting for the damage site suggested location of the probe ions in a highly distorted (or amorphous) regions. The annealing of the radiation damage was observed in two stages (100 - 200 K and 300 - 450 K). The first stage led to an increase of the interstitial fraction, while the second stage showed an increase in the substitutional fraction. In 2009, Bharuth-Ram *et al.* reported on Mössbauer studies on GaAs after ^{57}Mn implantation [34]. Similar sites to those observed in silicon based semiconductors were observed.

1.6 Motivation for current work

The ionized dopants, either donor or acceptor impurities, provide the major source of current carriers, i.e. electrons or holes in semiconductor devices. They are also the greatest source of electron impurity scattering in semiconductor devices, which determines the transport and optical properties of the semiconductor devices at low temperatures. The transport properties such as electron mobility and electron saturation velocity are useful parameters in design and

manufacture of high speed semiconductor devices such as transistors, optoelectronics devices, photovoltaic cells, and quantum dot structures [35- 37].

At present Silicon (Si) is the most commonly used semiconductor in fast semiconductor devices. However, III-V compound semiconductors such as Gallium Arsenide (GaAs), Indium Phosphide (InP) and Indium Arsenide (InAs) have also demonstrated capabilities of applications in high speed semiconductor devices. These compound semiconductors are also utilized for the creation of semi-insulating substrates. As a result, III-V compound semiconductors have drawn the attention of material science researchers in order to understand effects that may occur during the manufacturing of such semiconductor devices. When a foreign atom is introduced in the semiconductor device it may alter the device's electrical and optical properties. This may affect the functioning of a device by increasing or reducing the mobility of charge carriers. However, the foreign atom may also cause lattice disorder (defects), where it substitutes lattice atom from its original position (substitutional site) or locates in an interstitial site, and or forms defect complexes.

Studies on doping III-V semiconductor materials with transition metals helps to understand site locations and defects caused by impurities on compound devices. The convenient way of introducing impurity atoms in a substrate and tailoring their functionality for particular applications is by the ion implantation process. This process is advantageous since any suitable ion may be implanted into the single crystal, and the concentration and depth profile of the implanted ions may be precisely controlled. However, during ion implantation the collision of foreign atoms with lattice atoms results in radiation damage on the lattice, which may change the electrical characteristic of a semiconductor. In order to repair this radiation damage and place the impurity atoms into substitutional sites so that they can be electrically active, thermal annealing treatment of the implanted semiconductor is required.

The 3d transition metal atoms form deep impurity states in the energy gap region of semiconductors, and play an important role in the electronic and optical properties of semiconductors. In particular, the outer shells of the iron (^{57}Fe) ion can be $3d^6 4s^1$ or $3d^5 s^2$ with charge states Fe^{2+} or Fe^{3+} , respectively. In InP, the Fe^{3+} impurity ion acts as a deep acceptor and substitutional Fe atoms in the In sites produce semi-insulating substrate for current blocking

layers [36]. With ^{57}Fe as a probe nucleus, Mössbauer spectroscopy is a very useful technique which allows one to study the site location of the impurity atoms in the crystal lattice, their charges state and the complexes they form, as well as the annealing of implantation induced damage.

This work is hence concerned with the study of lattice sites and complexes formed in III-V compound semiconductors InAs and InP, using ^{57}Fe Mössbauer spectroscopy following the implantation of radioactive ^{57}Mn ions. The Debye temperatures and electronic charge states of the impurity ions in different lattice sites, and the annealing behavior of radiation damage, in particular, are investigated.

Objectives:

The objectives of the study are:

- to determine the lattice location and chemical nature of Fe impurity atoms in different lattice sites of n- and p-type InAs and InP compound semiconductors,
- to determine the isomer shifts and quadrupole splitting values and area fractions of Fe impurities at the different lattice sites and in impurity- complexes,
- to extract Debye temperatures of Fe impurities at different lattice sites and compare with those determined in earlier Mössbauer studies on III-V semiconductors [31],
- to determine charge states of Fe impurities in different sites (based on values of isomer shifts and quadrupole splitting), and
- to investigate the annealing behavior of the radiation damage as a function of annealing temperature.

CHAPTER 2

2.1 Principles of Mössbauer Spectroscopy

The physical phenomenon of emission or absorption of gamma ray photons by a nucleus without the loss of energy due to recoil of the nucleus is known as the Mössbauer effect. It was discovered by Rudolph Mössbauer in 1957 [38] who demonstrated the effect in Iridium. Later Stanley Hanna showed the effect in ^{57}Fe [39]. Since then, this effect has been established to as a very useful tool to study materials; the technique is known as Mössbauer spectroscopy. This effect has found many applications in various fields of science. The direct application of Mössbauer effect in chemistry and physics arises from its ability to detect weak interactions between the nucleus and its surroundings.

Mössbauer spectroscopy allows for the study of both bulk and surface properties of materials. One of the advantages of this technique is that there is no restriction concerning domain size as found in X-ray diffraction. Mössbauer spectroscopy can also be used to study nanostructure materials. It provides information on static properties such as magnetic properties, valence state, bonding and crystal structure as well as information on dynamic properties such as superparamagnetic relaxation, diffusion and mechanical vibrations of atoms. As a result, Mössbauer spectroscopy has been widely used in research and industry, which has given rise to at least two international conferences dedicated to applications of the Mössbauer Effect – the International Conference on Applications of the Mössbauer Effect (ICAME) and the International Symposium on Industrial Applications of the Mössbauer Effect (ISIAME).

More details elaborating the fundamentals of the techniques and applications of Mössbauer effect are found in [40-44]. The discussions in the following sections are based on these texts.

2.2 The Mössbauer effect

The Mössbauer effect involves the emission of photons (γ -rays) from nuclei in the excited state in a source and the resonant absorption of the γ -rays in identical nuclei in an absorber material. There are several factors which must be considered in order to understand the physical basis of the Mössbauer effect and the importance of recoilless emission of gamma rays, namely:

- Resonant emission and absorption of gamma photons
- Natural line width of gamma ray emitted by a nucleus
- Recoil energy, and
- Recoil-free fraction.

2.2.1 Resonant emission and absorption of gamma photons

The Mössbauer effect involves the emission of a gamma ray by a nucleus, as mentioned above. The properties of the nuclear transition and of the gamma ray are coupled through the conservation of energy and momentum involved during the resonance emission of gamma rays. Therefore, let us consider a nucleus in its excited state with energy E_e and mass number A (proton number Z and neutron number N) as shown in Figure 2.1 (a). If the nucleus decays from an excited state to its ground state E_g , a γ -ray is emitted from the nucleus. The emitted γ -ray can be absorbed by another nucleus in its ground state, as shown in Figure 2.1 (b). If this nucleus is of the same atomic number as the emitting nucleus, then the process is called *resonant absorption* of the gamma ray.

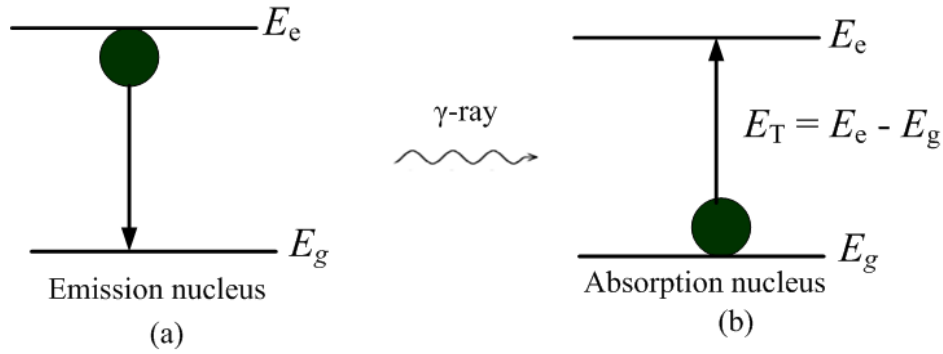


Figure 2.1: The nuclear transition from the excited state E_e to the ground state E_g results in the emission of a gamma ray.

The difference in energy between the excited state (E_e) and the ground state (E_g) of the atomic nucleus is the nuclear transition energy (E_T), i.e.

$$E_T = E_e - E_g. \quad (2.1)$$

Resonant absorption occurs when

$$E_\gamma = E_T, \quad (2.2)$$

where E_γ is the gamma ray energy.

2.2.2 Spectral line shapes

The gamma emission probabilities as a function of the transition energy $W(E)$, yield spectral lines centered around the nuclear transition energy E_T , and have *Lorentzian shape* as shown in Figure 2.2. This line shape is described by the Breit-Wigner relation: [42]

$$W(E) = \frac{\Gamma_N^2/4}{(E - E_T)^2 + \Gamma_N^2/4}, \quad (2.3)$$

Principles of Mössbauer Spectroscopy

where $W(E)$ is the relative probability, Γ_N is the natural line-width of the emission line and is equal to the line width at half-maximum height.

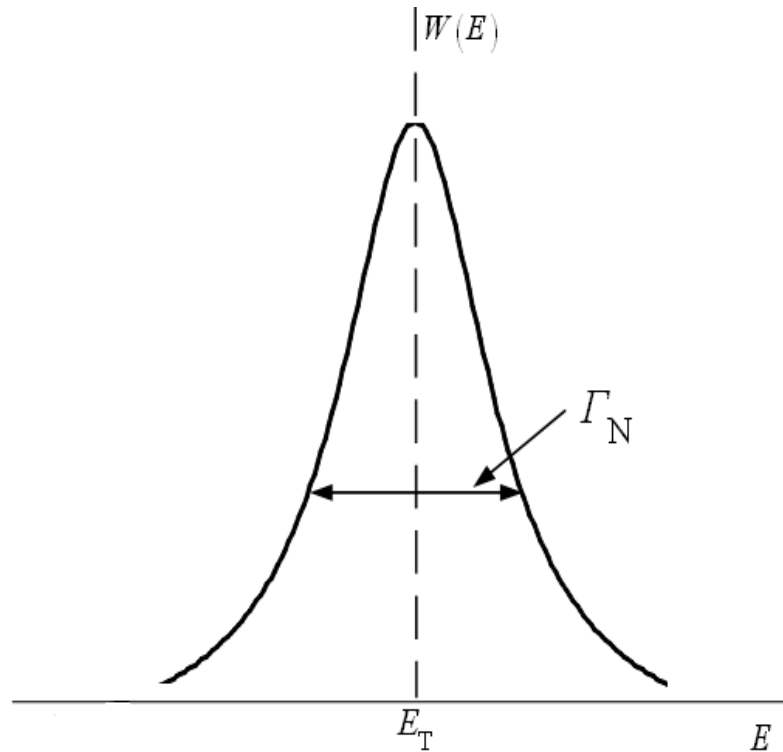


Figure 2.2: The statistical energy distribution of the emitted or absorbed γ -ray with natural line-width [42].

2.2.3 Natural line-width of the gamma ray emitted by a nucleus

From the Heisenberg uncertainty principle,

$$\Delta E \Delta t \geq \hbar, \quad (2.4)$$

we get the result that the line width of the energy distribution of gamma rays Γ_N at half maximum is related to the mean lifetime τ of the excited state by,

$$\Gamma_N = \frac{\hbar}{\tau} \quad (2.5)$$

where $\hbar = \frac{h}{2\pi}$, with h being Planck's constant.

2.2.4 Recoil energy

When a photon is emitted from an emitting nucleus, not only does it carry away energy E_γ , but it also carries away momentum p_γ . The conservation of momentum requires that the nucleus then recoils with an equal and opposite momentum (p_R),

$$p_R = -p_\gamma = -\frac{E_\gamma}{c}. \quad (2.6)$$

Thus,

$$p_R = Mv_R = -\frac{E_\gamma}{c}, \quad (2.7)$$

where M is the nuclear mass, v_R is the recoil velocity of the nucleus and c is the speed of light.

The recoil energy is given by,

Principles of Mössbauer Spectroscopy

$$E_R = \frac{1}{2} M v_R^2. \quad (2.8)$$

From the above equations, the recoil energy becomes

$$E_R = \frac{E_\gamma^2}{2Mc^2}. \quad (2.9)$$

When the γ -ray is absorbed by another nucleus, it will receive the same amount of recoil energy as the emitting nucleus and hence will move with the same velocity v_R in an opposite direction of the emitting nucleus, see Figure 2.3.

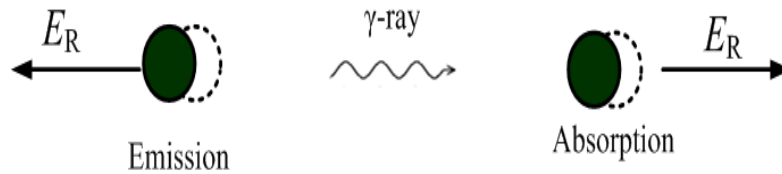


Figure 2.3: Recoil energy E_R received by an isolated nucleus on gamma ray emission or absorption.

As a result, the energy distribution lines for the emission and absorption will be separated by $2E_R$ and the γ -ray energy E_γ is not exactly the same as the nuclear transition energy E_T . For the emission process the energy of the γ -ray is given by $E_\gamma = E_T - E_R$. For the absorption process to occur the γ -ray must have energy $E'_\gamma = E_T + E_R$. The resonant absorption only occurs when emission and absorption spectral lines overlap, as discussed earlier. The spectral lines may overlap if the natural line-width $\Gamma_N > E_R$. This is satisfied in the case of an atomic transition, as shown in Figure 2.4 below. However, in nuclear transitions Γ_N is always very much less than the recoil energy. (e.g. for ^{57}Fe nuclei $\Gamma_N = 4.6 \times 10^{-9} \text{ eV}$, which is much smaller than $E_R = 40 \text{ eV}$).

Principles of Mössbauer Spectroscopy

As a result, the emission and absorption spectral lines do not overlap, hence the resonant absorption is not observed.

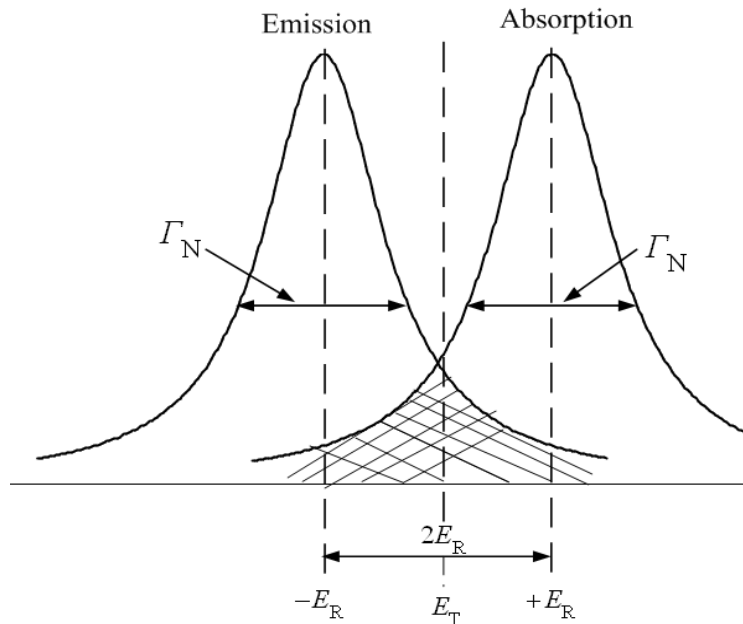


Figure 2.4: Resonance overlaps in free atoms. The overlap of emission and absorption spectra is shaded [40].

If the emitting nucleus is held by strong bonding forces in the lattice of a solid, the following two situations may arise: the nucleus may also dissipate its recoil energy by phonon creation, or the whole crystal may receive the recoil energy without phonon creation. If the whole crystal takes up the recoil energy, then the mass M in equation (2.8) becomes the mass of the crystal. Since the mass of the crystal is typically large, the energy lost due to recoil will be very small ($E_R \approx 0$). Hence, the emitted gamma-ray is emitted essentially without any loss of energy due to recoil and $E_\gamma = E_T$. Consequently, the Mössbauer Effect occurs.

2.2.5 Recoil-free fraction

There is a significant probability that the emission and absorption events are recoilless, meaning no phonon creation. This probability gives the Mössbauer recoil free fraction f and is related to the vibrational properties of the crystal lattice. The fraction f varies from solid to solid and is given by [41]

$$f = e^{-k^2 \langle x^2 \rangle}, \quad (2.10)$$

where $\langle x^2 \rangle$ is the component of the mean square vibrational displacement of the emitting (or absorbing) nucleus in the solid along the wave vector \mathbf{k} . For any real crystal the recoilless fraction f is always smaller than unity. To increase the relative strength of the recoilless resonance process, f must be as large as possible. The recoilless fraction f will be large for a tightly bound atom with a small mean square displacement.

The wave vector \mathbf{k} depends on the wavelength λ of the γ -ray and is given by

$$\mathbf{k} = \frac{2\pi}{\lambda} = \frac{E_\gamma}{\hbar c} \quad (2.11)$$

Substituting equation (2.11) into (2.10) gives

$$f = \exp \left[-\frac{E_\gamma^2 \langle x^2 \rangle}{\hbar^2 c^2} \right]. \quad (2.12)$$

According to the above expression, large values of f can be obtained if E_γ and $\langle x^2 \rangle$ are small.

The mean square vibrational displacement of the emitting nucleus can be determined from the vibrational properties of the crystal.

Using the Debye model the following expression for f can be deduced:

$$f = \exp \left[\frac{-6E_R}{k_B \theta_D} \left\{ \frac{1}{4} + \left(\frac{T}{\theta_D} \right)^2 \int_0^{\theta_D/T} \frac{x}{e^x - 1} dx \right\} \right], \quad (2.13)$$

Principles of Mössbauer Spectroscopy

where θ_D is a characteristic temperature of the lattice, called the Debye temperature, and T is the absolute temperature. Once θ_D is known, the recoil-free fraction f at any temperature can be evaluated from the above expression.

For low temperatures $T \ll \theta_D$, the integral in equation 2.13 becomes $\pi^2/6$, hence

$$f = \exp \left[\frac{-E_R}{k_B \theta_D} \left\{ \frac{3}{2} + \left(\frac{T\pi}{\theta_D} \right)^2 \right\} \right]. \quad (2.14)$$

Therefore, it is clear from equation (2.12) and (2.14) that $\ln f$ or $\langle x^2 \rangle$ is proportional to T^2 .

When $T > \theta_D$, the integral in equation 2.13 becomes θ_D/T so $\ln f$ or $\langle x^2 \rangle$ is linear in T , hence

$$\ln f = \frac{6E_R}{k_B \theta_D} \quad (2.15)$$

Maximum Mössbauer fraction is obtained when $T = 0$ which results in equation (2.14) simplifying to

$$f = \exp \frac{-3E_R}{2k_B \theta_D}. \quad (2.16)$$

Therefore, larger values of θ_D result in larger values of f from equation (2.16). The Debye temperature θ_D varies with chemical compounds and depends on the maximum vibrational frequency (ω_D) of the lattice. The Debye temperature is given by

$$\theta_D = \frac{\hbar \omega_D}{k_B}. \quad (2.17)$$

2.3 Hyperfine Interactions

The number, shape, position and relative intensity of the various absorption lines characterize a Mössbauer spectrum. These features result from the nature of the hyperfine interactions and their time dependence, as well as on any motion of the Mössbauer nuclei.

Hyperfine interactions occur between a nucleus and its surrounding environment that arise from the interactions between the static magnetic and electric moments of the nucleus with the electron charge distribution in its immediate vicinity. These interactions influence the nuclear levels and the transition energies, in a characteristic way from which valuable information about the absorbing atom and its surrounding can be obtained. The three main hyperfine interactions are:

- i) the electric monopole interaction, detectable as a line shift called isomer-shift (δ),
- ii) the electric quadrupole interaction, detectable as a line splitting called quadrupole splitting (ΔE_Q) and
- ii) the magnetic dipole interaction detectable as a line splitting-magnetic Zeeman effect (E_M).

In the following sections, we consider these hyperfine interactions and briefly discuss what information Mössbauer Spectroscopy can obtain.

2.3.1 Electric Monopole Interaction: Isomer Shift (δ)

Resonance absorption occurs at zero velocity between the source and absorber if both the source and absorber are in the same environment. If the source and absorber are not in the same environment then the resonance absorption occurs at a non-zero velocity. This shift in resonance from zero relative velocity is known as the *isomer shift*. The isomer shift results from the

Principles of Mössbauer Spectroscopy

electronic monopole interaction between the nuclear charge distribution over the finite nuclear volume and the electronic charge density over this volume. It arises because of the difference in the nuclear volume of the ground and excited states in the source and the absorber.

In the case where the electric monopole interaction is the only hyperfine interaction affecting the nuclear energy levels, then both ground and excited states remain unsplit. The separation between the nuclear states as shown in Figure 2.5 (a), differs by the isomer shift (δ) given by,

$$\delta = E_A - E_S \quad (2.18)$$

The energy change is obtained by comparing values obtained from a suitable reference spectrum, e.g. ^{57}Fe source natural iron absorber spectrum.

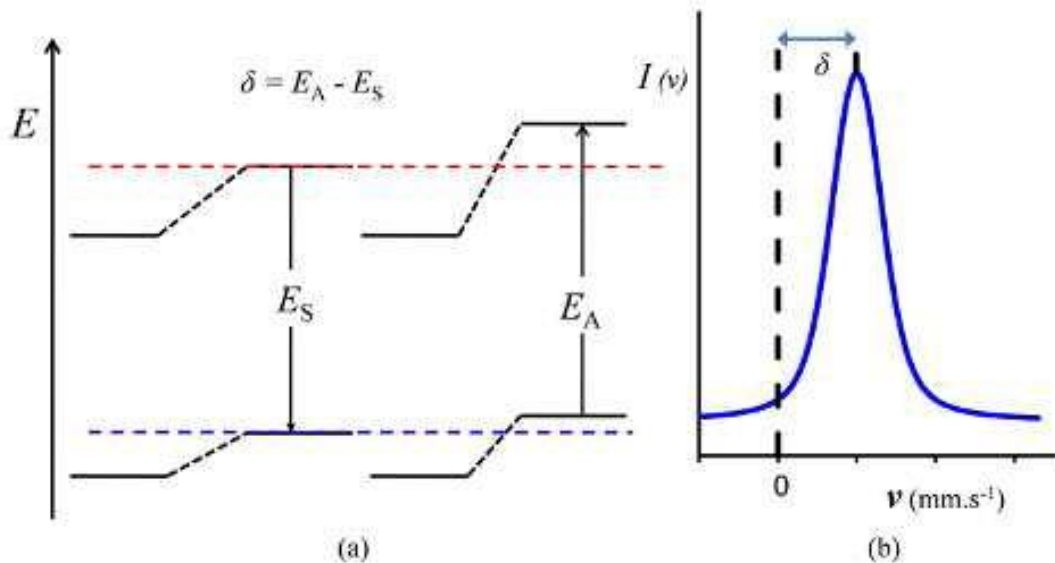


Figure 2.5: (a) Energy level diagram in the absence of a magnetic field or an electric field gradient. (b) Corresponding absorption line illustrating the isomer shift in the transition spectrum [22].

Principles of Mössbauer Spectroscopy

The isomer shift arises from the difference in the s-electron density at the nuclei of radioactive source and absorbing iron nuclei in the sample, which can be expressed by the following equation:

$$\delta = \frac{2\pi}{5} Ze^2 \left[|\psi_A(0)|^2 - |\psi_S(0)|^2 \right] \langle R_e^2 - R_g^2 \rangle, \quad (2.19)$$

where Ze^2 is the nuclear charge, $\langle R_e^2 \rangle$ and $\langle R_g^2 \rangle$ are the mean square radii of the excited and ground states, respectively. $|\psi_S(0)|^2$ and $|\psi_A(0)|^2$ are the total electron densities in the source and absorber, respectively [41]. The isomer shift is observed in the transition spectrum as a minimum shift of the absorption line away from the zero velocity, as illustrated in Figure 2.5 (b). The isomer shift allows us to determine the nuclear radius and the total charge density at the absorbing nucleus relative to the charge density around the Mössbauer nucleus in the source.

The nucleus interacts with s-electrons, thus s-electron charge density affects the nucleus prominently. However, the shielding effect from p, d and f orbitals as well as binding interactions of these orbitals also contributes to the electronic environment. The isomer shift yields useful information on the oxidation state of the nucleus in the absorber. Larger values of isomer shift suggest larger s-electron density, for example, for the ^{57}Fe atom 3s electrons are shielded by 4d electron density and cause the decrease in the electron density at the nucleus.

The isomer shift of energy levels can also arise from the thermal motion of the Mössbauer atoms. This phenomenon is known as the Second Order Doppler shift (δ_{SOD}) and is related to the isomer shift as follows

$$\delta(T) = \delta_c - \delta_{\text{SOD}}, \quad (2.20)$$

where δ_c is the total observed energy shift of the entire Mössbauer spectrum which is defined as a centre shift. The Second Order Doppler shift is related to the atomic mean square displacement in the lattice, thus it strongly depends on the temperature. The Second Order Doppler shift can be approximated by the Debye model as:

$$\delta_{\text{SOD}}(T) = -\frac{3k_{\text{B}}\theta_{\text{D}}}{Mc} \left[\frac{3}{8} + 3 \left(\frac{T}{\theta_{\text{D}}} \right)^4 \int_0^{\theta_{\text{D}}/T} \frac{x^3}{e^x - 1} dx \right]. \quad (2.21)$$

If $T = 0$ K, the above expression yields:

$$\delta_{\text{SOD}}(T = 0 \text{ K}) = -\frac{9k_{\text{B}}\theta_{\text{D}}}{8Mc}, \quad (2.22)$$

The Second Order Doppler shift depends on the material and hence can vary from material to material, for example substitutional to interstitial sites in the same substrate.

2.3.2 Electric Quadrupole Interaction: Quadrupole Splitting (ΔE_{Q})

In the previous section 2.3.1, we assumed that the nuclear charge distribution is spherical. However, nuclei with spin $I > \frac{1}{2}$ have non-spherical charge distribution and are characterized by a nuclear quadrupole moment Q which interacts with a non-uniform charge distribution, i.e. an electric field gradient (EFG), at the nucleus. The magnitude of the charge deformation is expressed as [40]

$$eQ = \int (3\cos^2\theta - 1)\rho r^2 d\tau, \quad (2.23)$$

where e is the charge on an electron, ρ is the charge density in the volume element $d\tau$ at a distance r from the centre of the nucleus at an angle θ to the axis of the nuclear spin. The sign of Q depends on the shape of the deformation ($-$ for oblate and $+$ for prolate shape).

The interaction between the quadrupole moment of the probe nucleus and the electric field gradient at the nucleus gives rise to a splitting of the nuclear energy levels, and is expressed by the Hamiltonian as

$$H = -\frac{1}{6}eQ\nabla E \quad (2.24)$$

The EFG is defined as the tensor

$$\nabla E = -V_{ij} \frac{\partial V}{\partial x_i \partial x_j}, \quad (2.25)$$

where V is the electric potential and $x_i, x_j = (x, y, z)$ refers to the principal axes of the EFG. Usually the axis system of the resonant atom is defined such that $V_{zz} = eq$ is the maximum value of the EFG [40]. Therefore, equation (2.24) becomes

$$H = \frac{e^2}{4I(2I-1)} \left[3\hat{I}_z^2 - I(I+1) + \frac{\eta}{2} (\hat{I}_+^2 + \hat{I}_-^2) \right], \quad (2.26)$$

where \hat{I}_+ and \hat{I}_- are shift operators and \hat{I}_z is a spin operator and η is the asymmetry parameter defined as

$$\eta = \frac{V_{xx} - V_{yy}}{V_{zz}}. \quad (2.27)$$

By convention, (x, y, z) are chosen so that $|V_{zz}| \geq |V_{yy}| \geq |V_{xx}|$ such that $0 \leq \eta \leq 1$. In case of a nucleus with $I = \frac{3}{2}$ excited state, for an example, the excited state splits into a pair of sublevels (doublet) $m_I = \pm \frac{1}{2}$ and $m_I = \pm \frac{3}{2}$ (see Figure 2.6). The quadrupole splitting (ΔE_Q) is measured as the separation of the two sublevels and is given by

$$\Delta E_Q = \frac{1}{2} e^2 q Q \left(1 + \frac{\eta^2}{3} \right)^{\frac{1}{2}} \quad (2.28)$$

which is a peak separation observed in a quadrupole split spectrum of ^{57}Fe , as shown in Figure 2.6, below. In equation (2.28), eQ is the nuclear constant for the resonant isotope, while eq is a function of the chemical environment of the probe nucleus. The equation above can give

information about the magnitude of q and η as well as the sign of the quadrupole splitting. The sign of e^2qQ may be an important factor in deciding the origin of the EFG [40].

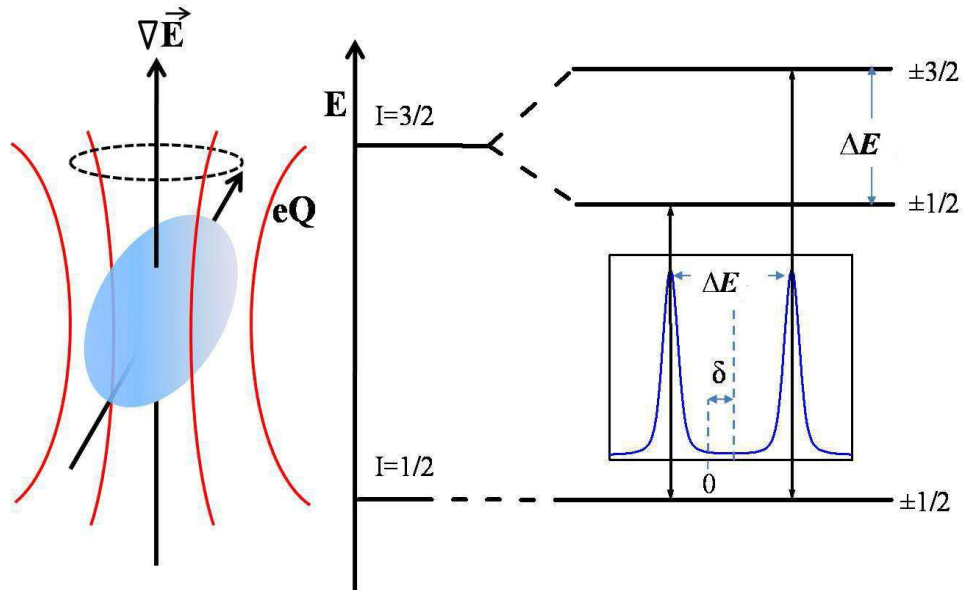


Figure 2.6: The effects on the nuclear energy levels of ^{57}Fe under a nuclear quadrupole interaction due to ∇E and eQ . The resulting Mössbauer spectrum, which gives the isomer shift δ and the quadrupole splitting ΔE_Q , is also shown [22].

The electric field gradient at the nucleus may result from different contributions, such as the asymmetry in the lattice contribution, from charges on distant ions, and the valence contribution due to incompletely filled electron shells and molecular orbitals. In general, the valence contribution is the major factor unless the ion has intrinsic symmetry of an s state ion such as high-spin Fe^{3+} (d^5). In the latter case the lattice contribution dominates. However, the effects of these contributions at the nucleus are modified by the polarization of the core electron of the Mössbauer atom which may enhance the EFG. Thus, the quadrupole splitting reflects the symmetry of the bonding environment and the nature of the local structure in the vicinity of the

Mössbauer atom. As a result, the quadrupole splitting gives information on the immediate environment of the nucleus. In semiconductors, the extracted quadrupole splitting provides a means to obtain information on the defect complexes that may be formed and details on the symmetry of the lattice site occupied by the probe nuclei.

2.3.3 Magnetic Hyperfine Interaction: Zeeman Splitting (E_M)

If a nucleus has a magnetic dipole moment (μ), then there will be an interaction between magnetic dipole moment and the magnetic field \mathbf{B} at the nucleus, which results in a splitting of the nuclear energy levels. The magnetic field at the nucleus may be due to an internal field or due to an externally applied field. This interaction is known as the magnetic dipole hyperfine interaction, also referred to as the Zeeman splitting. The Hamiltonian describing the magnetic dipole hyperfine interaction is given by:

$$H = g \mu_N I \cdot \mathbf{B}, \quad (2.29)$$

where g is the nuclear g factor, $\mu_N (= \frac{e\hbar}{2m_p c})$ is the nuclear magneton and \mathbf{B} is the sum of the applied field with the internal field of an unpaired electron.

The presence of a magnetic field causes both the ground and excited states to split according to the equation:

$$E_M = -g \mu_N B m_I, \quad (2.30)$$

where m_I is the magnetic quantum number which has values $I, I-1, \dots, -I$. The internal magnetic field splits the nuclear energy levels of spin I into $2I+1$ equidistantly spaced non-

Principles of Mössbauer Spectroscopy

degenerate sublevels [40]. Figure 2.7 shows the magnetic splitting of ^{57}Fe . The state of $I = \frac{1}{2}$

splits into $m_I = -\frac{1}{2}$ and $+\frac{1}{2}$; and $I = \frac{3}{2}$ splits into $m_I = +\frac{3}{2}, +\frac{1}{2}, -\frac{3}{2}$ and $-\frac{1}{2}$.

Hence, the presence of a magnetic field leads to the splitting of single line in a Mössbauer spectrum into a six-line resonance pattern (a magnetic sextet). The distance between the outermost lines is a measure of the hyperfine magnetic field. These lines are of similar line-widths but different intensities result from the nuclear selection rules $\Delta m_I = 0$, or ± 1 . The two transitions ($m_I = +\frac{1}{2}$ to $m_I = -\frac{3}{2}$ and $m_I = -\frac{1}{2}$ to $m_I = +\frac{3}{2}$) do not occur because they are forbidden by the selection rules. The Mössbauer spectrum in the presence of a magnetic hyperfine field is illustrated in Figure 2.7. For a thin absorber in which the nuclear spins are randomly orientated, the ratio of the sextet lines is 3:2:1:1:2:3 and their widths are assumed to be the same.

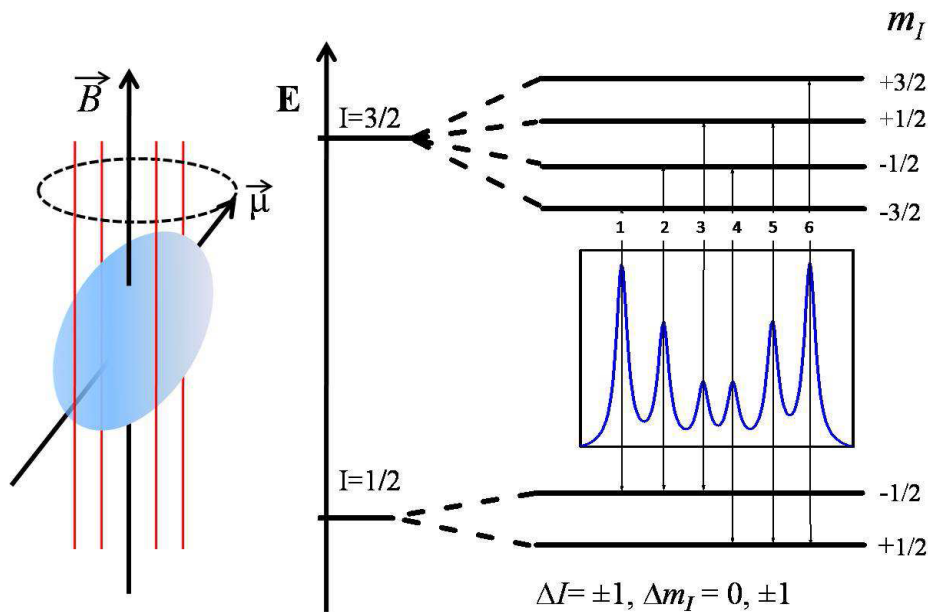


Figure 2.7: The magnetic splitting of $I = \frac{1}{2}$ and $I = \frac{3}{2}$ nuclear energy levels in ^{57}Fe [22].

2.3.4 Combined Quadrupole and Magnetic interactions (ΔE_{QM})

In the presence of both the electric field gradient and a hyperfine magnetic field at the nucleus, both quadrupole and magnetic splittings occur. The Hamiltonian describing this effect is given by the sum of the right hand side of equations (2.24) and (2.29). Both the quadrupole and magnetic splittings are directional dependants, but the interpretation of the Mössbauer spectrum is quite complex. The quadrupole splitting can be treated as first order perturbations to the magnetic interaction for $\frac{1}{2} \rightarrow \frac{3}{2}$ decay (see Figure 2.8) provided that $e^2qQ \ll \mu_B$. The energy levels are given by [40]:

$$\Delta E_{QM} = \frac{e^2 q Q}{4} (-1)^{\left(m_i + \frac{1}{2}\right)} \left(\frac{3 \cos^2 \theta - 1}{2} \right) - g \mu_N m_i \cdot \mathbf{B} . \quad (2.31)$$

Here θ is the angle between the magnetic axis and EFG tensor axis.

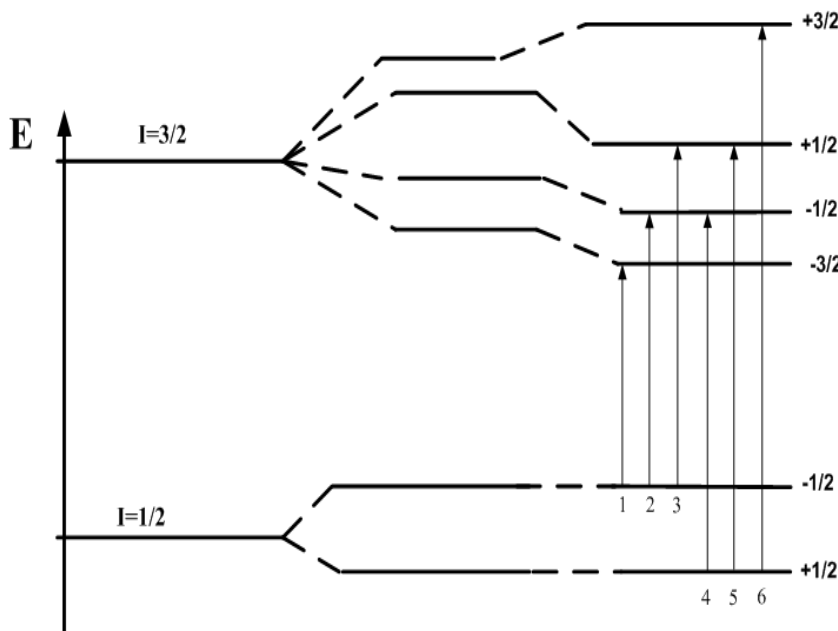


Figure 2.8: The effect of a first-order quadrupole perturbation on a magnetic hyperfine spectrum for $I = \frac{1}{2} \rightarrow I = \frac{3}{2}$ transition in ^{57}Fe .

In this case, the magnetic hyperfine interaction lines are dominated by the quantity:

$$\frac{e^2qQ}{4} \left(\frac{3\cos^2\theta - 1}{2} \right). \quad (2.32)$$

The angle θ and the value of e^2qQ cannot be determined separately from the line position. The presence of a small quadrupole perturbation is easily observed because the spectrum is non-symmetrical about the centroid [40].

2.4 Mössbauer spectrum

A Mössbauer source consisting of radioactive nuclei embedded in a suitable matrix is mounted on a velocity drive unit in order to generate a Mössbauer absorption spectrum. The γ -rays emitted from the source which has a significant recoilless fraction are passed through an absorber containing atoms of the same nucleus. The intensity of the γ -radiation transmitted is measured as a function of velocity in mms^{-1} (i.e. effective γ -ray energy). The decrease in transmission is affected by the difference in relative values of E_γ for the source and the absorber (see Figure 2.9). The effective E_γ value can be altered by moving the source and absorber relative to each other with a relative velocity v , so that the γ -ray energy is Doppler shifted by an amount $E = \frac{v}{c} E_\gamma$, where c is the speed of light.

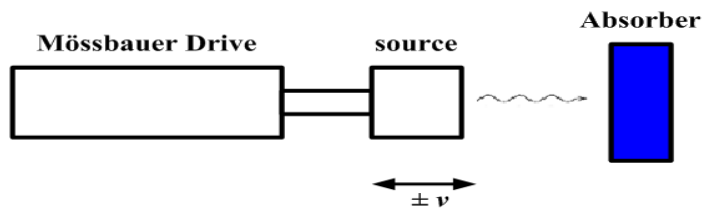


Figure 2.9: Schematic representation of a source on the velocity drive unit, absorber and detector in a transmission Mössbauer geometric arrangement.

Resonance absorption occurs when the effective E_γ values are exactly matched to the difference between the ground state and excited state of the probe nucleus in the absorber. R.L. Mössbauer discovered that by placing emitting and absorbing nuclei in a crystal then it could be used for recoil. However, if the internal conversion coefficient (α) is high, few γ -rays will be emitted.

2.4.1 Mössbauer line intensities

The Mössbauer spectrum is easily interpreted if the line intensities of components are known. Line intensities are determined from the theory of the coupling of angular momenta, provided that the quadrupole splitting, magnetic splitting and the spin quantum numbers for each state are determined. The final results contain the angular-independent and angular- dependent terms. The angular independent term corresponds to a case where there is no preferred orientation. Thus, examining the angular independent term, the probabilities of the intensity are given by the square of the appropriate Clebsch-Gordan coefficients (C) [40]

$$Intensity \propto \langle I_1 J - m_1 m | I_2 m_2 \rangle^2, \quad (2.33)$$

where I_2 and I_1 are nuclear spins of the excited and ground states, respectively, J is the vector sum $I_1 + I_2$, m_1 and m_2 are quantum numbers, m is the vector sum $m_1 - m_2$. The quantity J is also referred to as the multi-polarity of the transition. Smaller values of J give large intensities. If there is no change in polarity during the decay the transition is classified as the magnetic dipole (M1) or electric quadrupole (E2).

For ^{57}Fe , the energy absorption in the $\frac{1}{2} \rightarrow \frac{3}{2}$ transition gives eight possible transitions between the levels. The corresponding Clebsch-Gordan coefficients are listed in Table 2.1. These coefficients are obtained for the magnetic spectra (M1) when $J=1$. The transitions $+\frac{3}{2} \rightarrow -\frac{1}{2}$ and $-\frac{3}{2} \rightarrow +\frac{1}{2}$ have zero probability as $\Delta m = \pm 2$ for these transitions. The ratio of line

Principles of Mössbauer Spectroscopy

intensities for the six possible transitions extracted from the values of the normalized C^2 is 3 : 2 : 1 : 1 : 2 : 3. The corresponding terms for a quadrupole spectrum are obtained by simulation which gives the ratio of 1:1 when the electric field gradient has axial symmetry.

The angular dependent terms $\theta(J, m)$ in Table 2.1 are expressed as the radiation probability in the direction at an angle θ to the quantization axis. In this case, the probabilities of intensity will

be in the ratios 3: x : 1: 1: x : 3, where $x = 4 \left(\frac{\sin^2 \theta}{1 + \cos^2 \theta} \right)$ [38].

For the quadrupole spectra (E2), where there are two transitions $\pm \frac{1}{2} \rightarrow \pm \frac{1}{2}$ and $\pm \frac{3}{2} \rightarrow \pm \frac{1}{2}$, the corresponding values of C^2 give a 1:1 ratio (see Table 2.1). The angular dependent coefficients give 1: 3 ratios if the γ -ray axis is parallel to the direction of V_{zz} and a 5:3 ratio if perpendicular to V_{zz} . If the magnetic and quadrupole interactions are present or the asymmetry parameter is non-zero, the energy states are represented as a linear combination of terms.

Table 2.1: Relative probabilities for a dipole $\frac{3}{2}, \frac{1}{2}$ transition. C is calculated

by $\left\langle \frac{1}{2} 1 - m_1 m \left| \frac{3}{2} m_2 \right\rangle\right.$ converted by means of the relationship

$$\left\langle \frac{1}{2} 1 - m_1 \left| \frac{3}{2} m_2 \right\rangle = (-)^{\frac{1}{2} m_1} \sqrt{\left\langle \frac{3}{2} \frac{1}{2} m_2 m_1 \left| 1 m \right\rangle\right.}; C^2 \text{ and } \Theta \text{ are normalized angular}$$

independent and dependent terms, and 90° and 0° are relative intensity angles with respect to the principal axis [40].

m_2	$-m_1$	m	C	C^2	Θ	Relative intensities at	
						$\theta = 90^\circ$	$\theta = 0^\circ$
$+\frac{1}{3}$	$+\frac{1}{2}$	+1	1	3	$1 + \cos^2 \theta$	3	6
$+\frac{1}{2}$	$+\frac{1}{2}$	0	$\sqrt{\frac{2}{3}}$	2	$2 \sin^2 \theta$	4	0
$-\frac{1}{2}$	$+\frac{1}{2}$	-1	$\sqrt{\frac{1}{3}}$	1	$1 + \cos^2 \theta$	1	2
$-\frac{3}{2}$	$+\frac{1}{2}$	-2	0	0	0	0	0
$+\frac{3}{2}$	$-\frac{1}{2}$	+2	0	0	0	0	0
$+\frac{1}{2}$	$-\frac{1}{2}$	+1	$\sqrt{\frac{1}{3}}$	1	$1 + \cos^2 \theta$	1	2
$-\frac{1}{2}$	$-\frac{1}{2}$	0	$\sqrt{\frac{2}{3}}$	2	$2 \sin^2 \theta$	4	0
$-\frac{3}{2}$	$-\frac{1}{2}$	-1	1	3	$1 + \cos^2 \theta$	3	6

Quadrupole splitting (E2)		Relative intensities at		
Transition	C^2	Θ	$\theta = 90^\circ$	$\theta = 0^\circ$
$\pm \frac{1}{2}, \pm \frac{1}{2}$	1	$2 + 3 \cos^2 \theta$	5	2
$\pm \frac{3}{2}, \pm \frac{1}{2}$	1	$3(1 + \cos^2 \theta)$	3	6

CHAPTER 3

3.1 Experimental Details

The measurements presented in this work were conducted at the ISOLDE facility at CERN (European Centre for Nuclear Research in Geneva, Switzerland). This Chapter briefly describes the ISOLDE facility and the techniques applied for data acquisition. This is followed by a description of the Mössbauer experimental set-up at CERN and how the measurements were undertaken.

3.1.1 The ISOLDE Facility at CERN

The ISOLDE facility is an on-line isotope separator facility dedicated to the production of a variety of radioactive ion beams for a great number of different experiments [45, 46]. The radioactive ion beams enable research in the fields of nuclear and atomic physics, solid-state physics, life sciences and material science. This facility is located at the *Proton-Synchrotron Booster* (PSB) accelerator complex at CERN and is operated by the ISOLDE Collaboration.

The radioactive nuclides are produced in reactions of high-energy protons from PSB accelerator in thick targets via fission or fragmentation reactions. Targets are placed in the external proton beam of the PSB, which has energy of 1.0 GeV or 1.4 GeV. Figure 3.1 shows the layout of the ISOLDE facility at CERN. A target material is kept at an elevated temperature up to 800 K, so that the produced radioactive atoms diffuse out of the target into different dedicated ion sources. Ionization can take place in hot plasma, on a hot surface or by laser excitation. An electric field accelerates ions which are then mass separated and steered to the experiments. The radioactive ions are employed for many nuclear solid techniques such as Perturbed Angular Correlations (PAC), Mössbauer Spectroscopy (MS) and Emission Channeling (EC).

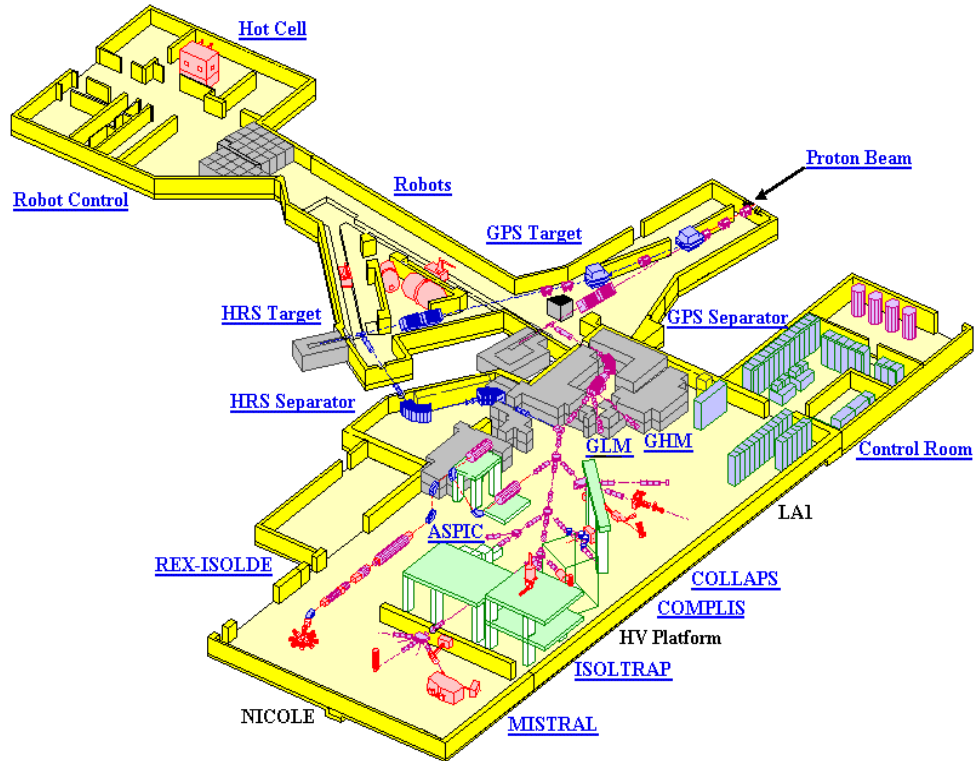


Figure 3.1: The schematic layout of the ISOLDE facility at CERN [47].

Applications of these techniques involve the investigation of radiation damage, lattice sites of dopants, site selective doping of semiconductors, donor-acceptor interactions in semiconductors, diffusion studies, and the investigation of surfaces and interfaces.

The Mössbauer experimental setup at CERN is directly connected to the on-line mass separator (*on-line Mössbauer spectroscopy*). The usage of radioactive isotope beams for on-line Mössbauer spectroscopy has proved to be a powerful method to obtain atomic information concerning the final lattice position and dynamic behavior of Fe atoms in semiconductors [48-52]. The on-line Mössbauer arrangement using a radioactive pre-cursor has the advantage that both ion implantation and probing of the lattice can be performed at the same time.

3.2 Geometrical arrangements of the Mössbauer spectroscopy experiment

There are two geometrical arrangements of measuring the recoilless resonant absorption of γ -rays, namely transmission and backscatter geometry, as shown in Figure 3.2. In the transmission geometry the detector is aligned with the source where it detects γ -rays transmitted through an absorber. However, in the backscattering geometry a detector is placed at an angle relative to a source on the same side of the incident gamma rays.

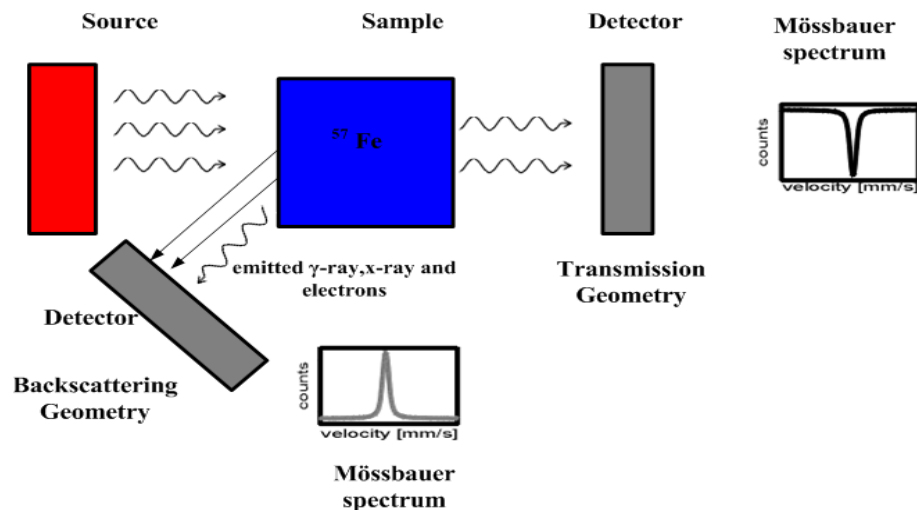


Figure 3.2: Geometrical arrangements on Mössbauer spectroscopy, adopted from [53].

3.2.1 Transmission Mössbauer Spectroscopy (TMS)

Transmission Mössbauer Spectroscopy (TMS) is the common experimental geometry arrangement for measurements of the Mössbauer effect and its experimental set-up is simple. This Mössbauer arrangement is limited to measurements on powders or thin foils, where the γ -ray transmitted through an absorber is measured. The whole sample contributes to the spectrum

and a multilayer sample with many interfaces is always required in order to prevent lattice structure distortion.

3.2.2 Conversion electron Mössbauer spectroscopy (CEMS)

Conversion Electron Mössbauer Spectroscopy (CEMS) is the method by which one can investigate Mössbauer effect in backscattering geometry, and instead of detecting gamma rays one detects the conversion electrons emitted in the decay of the Mössbauer probe nucleus. The internal conversion process in the decay of the excited state of iron nucleus is shown in Figure 3.3. During the process, the decay gamma photon transfers its energy to electrons from the K, L or M electronic shells, which are then emitted. The subsequent transition of electrons from higher levels to fill the holes in the L shell to K shell is followed by emission of X-rays and Auger electrons.

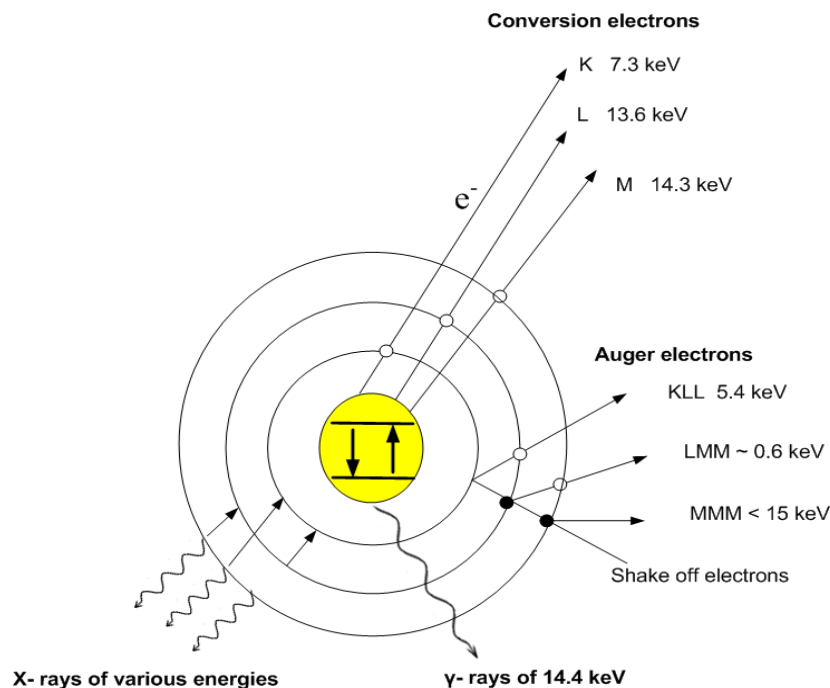


Figure 3.3: Internal conversion process after Mössbauer effect of ^{57}Fe nucleus, modified from [54].

The CEMS detector is most sensitive to low energy electrons. The emitted K-electrons are preferably detected in the case of internal conversion electrons detection, because these electrons are closer to the nucleus. An iron K-conversion electron is ejected with a kinetic energy equivalent to the difference between the gamma-ray energy and binding energy [55].

The CEMS investigations are usually restricted to the near-surface of a sample rather than the bulk, because of relatively low kinetic energy of the K-electrons. It is also useful for samples with thick substrates or high Z where transmission of γ -rays through a sample is blocked. Thus, it is useful in studying implanted samples [56]. The advantage of this method compared with TMS method is that samples any shape and thickness can be used, for which there is the limit on the sample for TMS method.

3.3 Mössbauer spectroscopy instrumentation

The experimental set up for Mössbauer spectroscopy consists of a source, a detector for detecting emitted γ -rays and a drive mechanism for imparting a Doppler velocity to the source. A Doppler shift is the energy of the emitted gamma rays which is achieved by either moving the source or the detector. Therefore a drive mechanism is necessary for moving a source or the detector in a very accurate, measurable way. In most cases the source is mounted on a vibrator, which moves the source at constant acceleration. The source is moved through range of linear velocities (measured in mm. s^{-1}) relative to the absorber. The energy of gamma rays increases, when the γ -ray source is moving with velocity v_x towards (positive Doppler velocity) the absorber. The energy E_γ of the emitted γ -ray is modulated by the Doppler shift and is given by:

$$E_\gamma = E_T + \frac{v_x}{c} E_T , \quad (3.1)$$

where c is the velocity of light, E_T is the nuclear transition energy and v_x is a velocity along x -axis.

3.3.1 ^{57}Fe Mössbauer Spectroscopy

The most frequently used isotope for Mössbauer spectroscopy is ^{57}Fe . The study of Mössbauer effect in ^{57}Fe is useful because the lifetime for the 14.4 keV excited states is 98 ns, giving narrow natural line-width ($\sim 0.097 \text{ mm. s}^{-1}$) of the 14.4 keV transition. In addition, the f value is large, ranging from 0.65 to 1. In conventional emission Mössbauer studies, the ^{57}Fe Mössbauer state is produced by the K-electron capture decay of ^{57}Co which has a lifetime $t_{1/2} = 270$ days.

The energy level schemes for ^{57}Co and ^{57}Mn is shown in Figure 3.4. ^{57}Co decays to $^{57}\text{Fe}^*$ at 137 keV level, by internal conversion, i.e. process in which a proton in the nucleus captures an electron from the K-atomic shell. $^{57}\text{Fe}^*$ either decays directly to the ground state and emits a 137 keV γ -ray or decays to the 14.4 keV level and emits a 122 keV γ -ray. The 14.4 keV level decays to the ground state by gamma-ray emission or internal conversion.

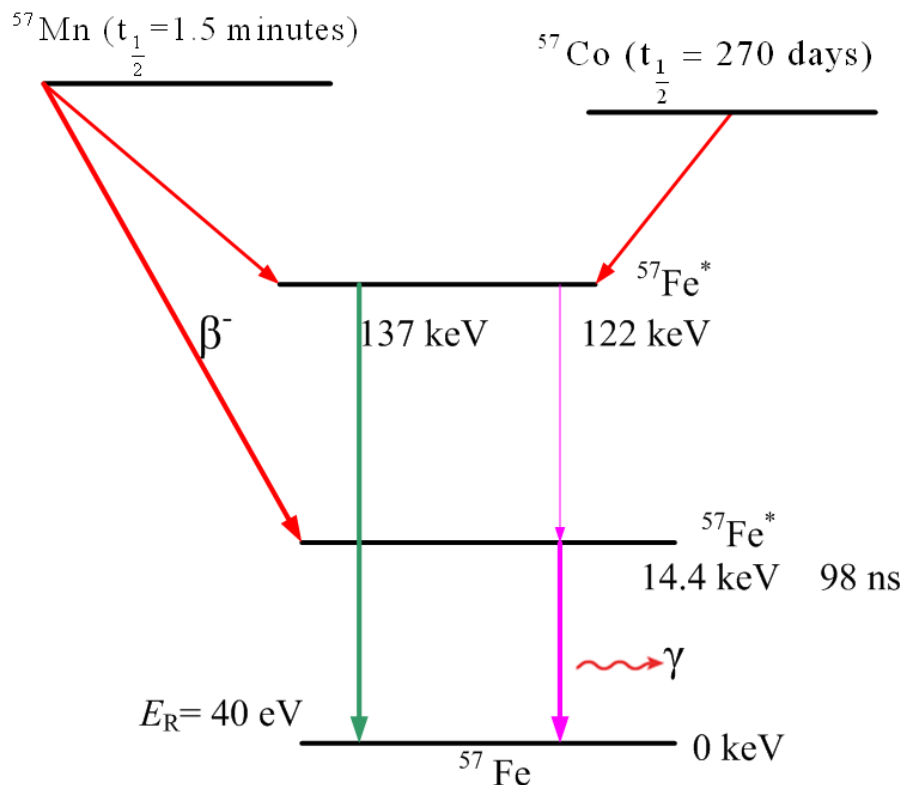


Figure 3.4: Decay scheme of ^{57}Fe and parent nuclei.

Another method of population the ^{57}Fe , 14.4 keV level is through the β -decay of $^{57}\text{Mn}^*$. The nuclide ^{57}Mn with a short half-life ($t_{\frac{1}{2}} = 1.5$ minutes) undergoes β^- - decay to $^{57}\text{Fe}^*$. About 80% of ^{57}Mn nuclei decay directly to the 14.4 keV Mössbauer level of ^{57}Fe . The short half-life of ^{57}Mn nuclide gives it an advantage over ^{57}Co ($t_{\frac{1}{2}} = 270$ days) nuclide since a spectrum with good statistics is obtained in less than 10 minutes,

- an extremely low ion implantation fluence ($\leq 10^{12}/\text{cm}^2$) is used, which ensures single ion implantation and no damage cascade, and
- during β^- - decay of $^{57}\text{Mn} \rightarrow ^{57}\text{Fe}^*$ an average recoil energy of $E_R = 40$ eV is imparted to the ^{57}Fe ions so that a sizeable fraction of ^{57}Fe ions is expelled onto interstitial or substitutional sites.

3.3.2 $^{57}\text{Mn}^*$ beam production at ISOLDE

At ISOLDE radioactive ion beams of $^{57}\text{Mn}^*$ ($t_{\frac{1}{2}} = 1.5$ min) are produced by means of 1.4 GeV protons induced nuclear fission in a Uranium Carbide (UC_2) target. Following multistage laser ionization, mass separated clean beams of $^{57}\text{Mn}^+$ ions are produced and accelerated to 60 keV [49, 57, 58]. A schematic arrangement of the beam production and acceleration into the Mössbauer set up at ISOLDE is shown in Figure 3.5.

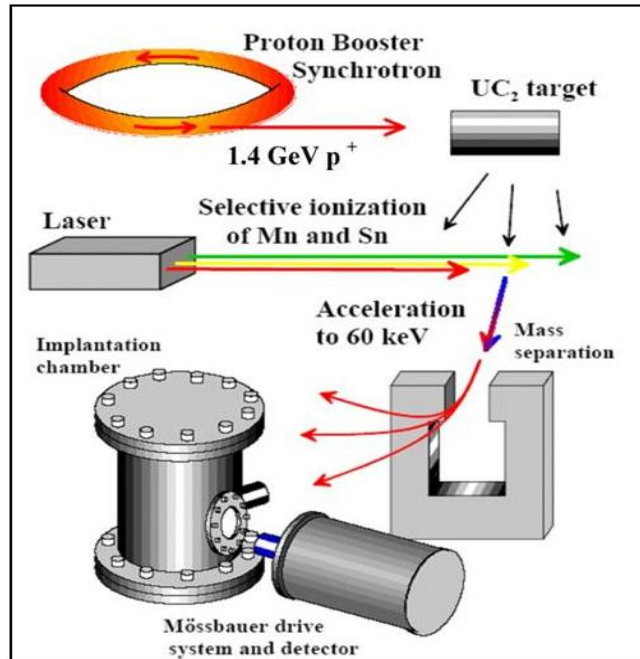


Figure 3.5: Beam production at ISOLDE ⁵⁷Mn beam-line system. After ionization, the beams are mass-separated then accelerated directly to an implantation chamber where samples are held, then collected by the gas-filled PPAC detector mounted on a Mössbauer drive unit outside the implantation chamber [59].

3.3.3 Experimental details of the ISOLDE Mössbauer system

The Mössbauer system used at ISOLDE/CERN is shown in Figure 3.6. The accelerated ion beams having intensities $\geq 10^8 \text{ s}^{-1}$ are directed to the vacuum implantation chamber where samples are held. The implantation chamber is connected to the ⁵⁷Mn* beam-line system. The sample under study is mounted in the implantation chamber, and can be held at temperatures in the range 300–800 K. The ⁵⁷Mn* sample thus acts as a source and a specially designed light weight detector, a *Parallel Plate Avalanche Counter* (PPAC), is required which is mounted on a velocity drive system outside the implantation chamber.

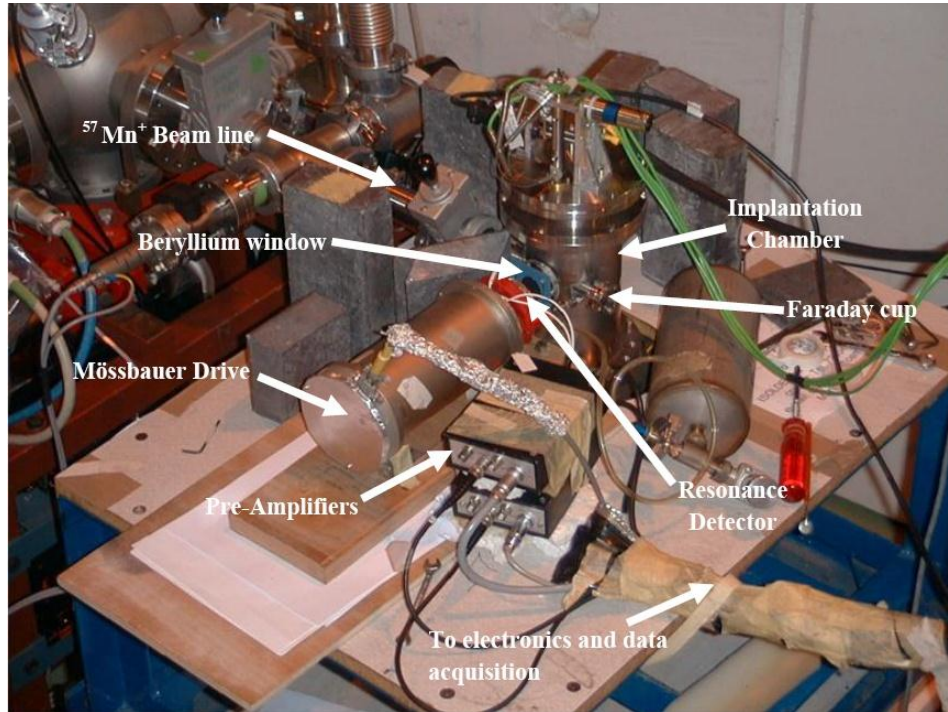


Figure 3.6: Experimental arrangement of the Mössbauer system at ISOLDE/CERN. A $^{57}\text{Mn}^+$ beam is directed to an implantation chamber in which the sample is mounted, the gas-filled PPAC detector is mounted on a Mössbauer drive unit outside the implantation chamber. The PPAC is connected to a Voltage supply and a pre-amplifier.

A PPAC detector consists of two conducting plates (cathode and anode) with Acetone gas between them. The conducting plates are mounted in parallel to each other with a small separation of 3 mm and used in transmission mode. A cathode is made a stainless steel foil enriched in ^{57}Fe while the anode is made of graphite. An electric field is created between the plates by applying high voltage between the anode and the cathode. Electrons are accelerated by the field towards the anode. A counter gas is used to amplify the low conversion-electron current emitted by the sample, with an avalanche effect taking place between the plates. Thus, the PPAC detector is used to detect internal conversion electrons emitted after resonant absorption of 14.4 keV ^{57}Fe Mössbauer γ -rays. The PPAC is efficient for Mössbauer γ -radiation, having a

high signal-to-background ratio due to its insensitivity to x - and γ -radiation and relatively high time resolution [60, 61].

The detector is mounted on a commercial electromagnetic drive system providing the Doppler velocity to record a spectrum of the emitted radiation. The detector is placed outside the implantation chamber. The detector is moved using triangular drive signal (linear velocity scale) as a function of time.

The PPAC is connected in series to a high voltage supply and pre-amplifier. The pre-amplified pulses are amplified and then the main amplifier directs DC voltage pulses to a central Multi-Channel Analyzer (MCA) operating in multichannel scaling mode (MCS) in which the start/time zero of the sweep and the dwell time in each channel is synchronized with the Mössbauer Drive Unit. The MCA card is installed in a Personal Computer used for the accumulation of the data and visualization of the spectra in which the counts are accumulated in channels (512 or 1024).

A sample holder with four samples positions is utilized, allowing for a series of measurements without having to break the vacuum condition, as show in Figure 3.7. One of the sample position is used for calibration with an α -Fe foil. An Osram halogen photo-optic lamp operating at 15 V and 150 W is incorporated in the implantation chamber. This provides rapid heating of the sample to a temperature up to 800 K.



Figure 3.7: Four position sample holder mounted with annealing system.

3.4 Samples and Measurements

The samples used for this study were commercially available grown by Molecular Beam Epitaxy (MBE). Mass separated $^{57}\text{Mn}^*$ ions were implanted to a fluence of $\leq 10^{12}$ ions/cm² (to assure single ion implantation) with 60 keV energy, at 60° to the surface normal (as shown Figure 3.8) into intrinsic InP p-type InAs and n-type InAs single crystals held at 300-650 K in the implantation chamber.

The dimensions of each sample were $0.3 \times 10 \times 10$ mm³. The crystals were heated by irradiation from the halogen photo-optic lamp from the rear of the four-position sample holder. The implantation times ranged from 8-15 minutes. Mössbauer spectra were recorded using the resonance detector (PPAC) described above. The drive velocity was calibrated using an α -Fe absorber which also provided the reference point for the isomer shifts of the spectral components. Six spectra for each arsenide sample and seven for the phosphide sample were collected at a range of temperatures.

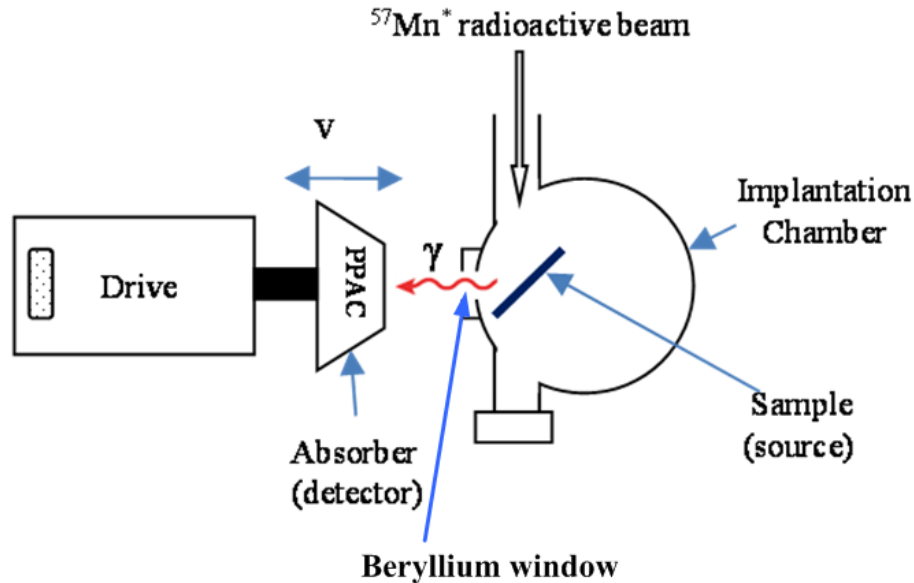


Figure 3.8: Implantation and detection system at the Mössbauer set up at ISOLDE [22].

3.4.1 Calibration of Mössbauer spectrum

In order to determine accurately the energy (velocity) scale, the spectra need to be calibrated. This is done with the use of a metallic α -Fe absorber because of its well defined magnetic sextet of absorption lines. Furthermore, the hyperfine field will not change significantly with small temperature variations, because α -Fe has high Curie temperature (about $T_c = 1043$ K) [62]. The first step of the calibration is to fold the spectrum, shown in Figure 3.9, which results in the velocity spectrum shown in Figure 3.10. This is a simple example of an absorber spectrum with pure nuclear magnetic splitting.

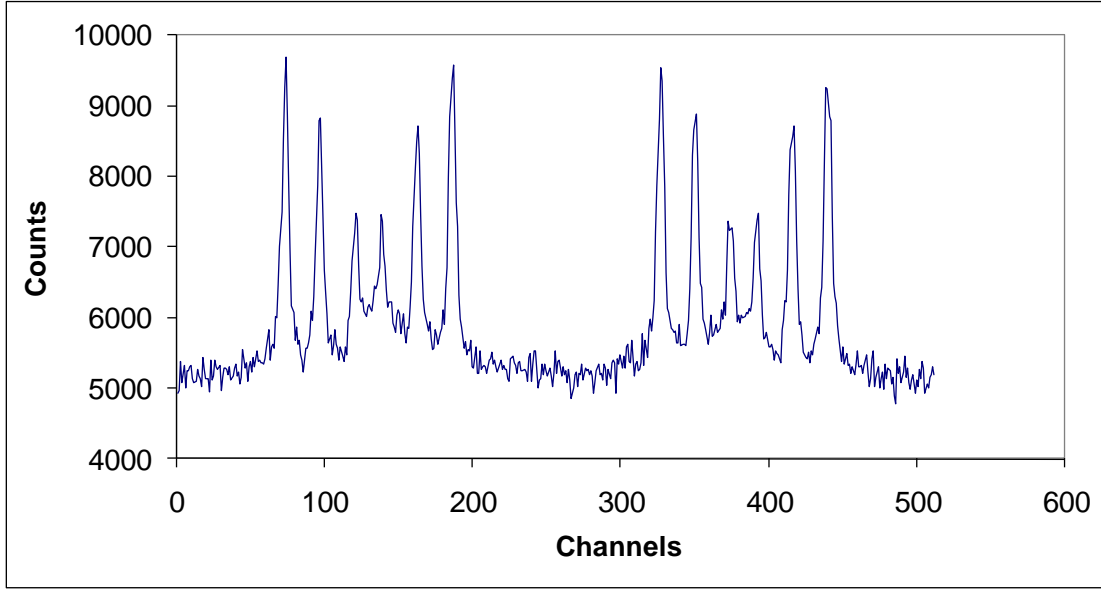


Figure 3.9: Unfolded Mössbauer spectrum of enriched α -Fe.

Thereafter, spectrum calibration occurs by fitting the six absorption line positions with the ratio 3 : 2 : 1 : 1 : 2 : 3 to the calibrated values by means of a least-square fitting program. This yields the velocity (v_0) of the zeroth channel and the velocity increment (Δv) per channel. The velocity of each channel i in the spectrum is determined by:

$$v_i = v_0 + i\Delta v \quad (3.2)$$

Accepted hyperfine parameters for α -Fe at room temperature are: magnetic field $\mathbf{B} = 33.04$ T, quadrupole splitting $\Delta E_Q = 0$ mm. s⁻¹ and isomer shift $\delta = 0$ mm. s⁻¹ [63].

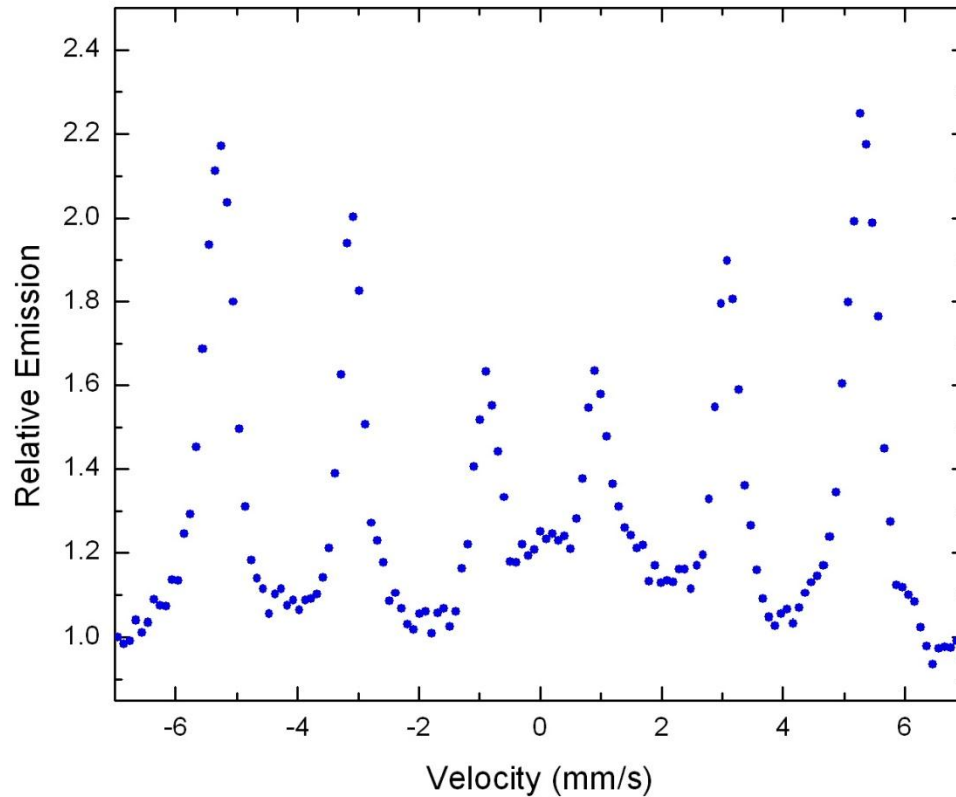


Figure 3.10: Example of a Folded Mössbauer spectrum of an α -Fe absorber.

3.5 Data and error analysis

The fitting of the spectra was undertaken with the aid of the fitting programme called Vinda, developed by Dr H.P. Gunnlaugsson [64]. The Vinda programme operates within Microsoft Excel, where all commands are contained in a toolbar that runs Visual Basic for Applications macros. This program enables simultaneous analysis of the spectra for an entire temperature range and also does an error analysis.

CHAPTER 4

4.1 Results and Analysis

This chapter presents results of the Mössbauer measurements on InP, n-type InAs and p-type InAs samples following the implantation of radioactive $^{57}\text{Mn}^+$ ions. The first section of the chapter focuses on the analysis of the Mössbauer spectra. The second section presents a comparison of extracted Mössbauer hyperfine interaction parameters for the materials under study with previous work. The third section discusses the recovery of the lattice damage formed during the implantation process, and the last section compares results obtained from various probe implantations in materials under study.

4.2 Data analysis of InP

The Mössbauer measurements were conducted on a single crystal InP sample held at temperatures ranging from 300 to 650 K in an implantation chamber. The spectra are shown in Figure 4.1. A broad doublet component, reflecting the damaged environments of the probe nuclei, dominates the spectra at low temperatures (303–426 K). The lattice damage starts to anneal at 426 K and a singlet is the dominant spectral component.

All spectra were analyzed by means of least-square fitting procedure using Voigt lineshapes, i.e. Lorentzian lines with Gaussian broadening. Several models were applied in seeking consistent fits to the data. In the final analysis, the following components were found to give acceptable fits in a simultaneous analysis of the spectra in the entire temperature range for all three samples:

- An asymmetric doublet (Fe_D)
- A single line (Fe_S) and
- A symmetric doublet (Fe_X)

The deduced hyperfine parameters are given in Table 4.1.

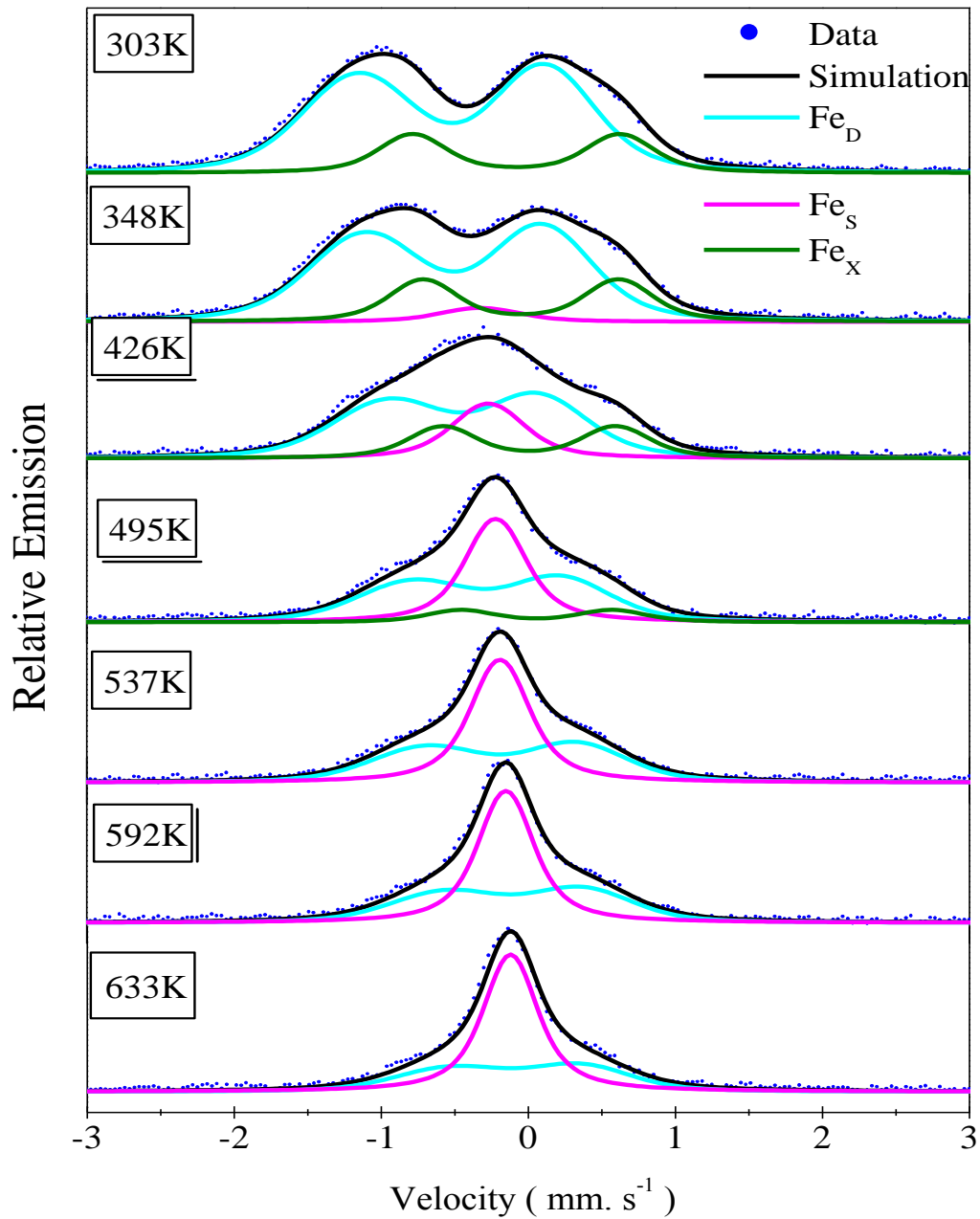


Figure 4.1: Mössbauer spectra of InP obtained at temperatures indicated after $^{57}\text{Mn}^*$ implantation.

Table 4.1: Hyperfine parameters: isomer shift (δ) and quadrupole splitting (ΔE_Q), the Gaussian broadening (σ) obtained at room temperature from a simultaneous analysis of the spectra for InP, and the extracted Debye temperatures (θ_D) for the different lattice sites and errors in parentheses.

Component	δ (mm.s ⁻¹)	ΔE_Q (mm.s ⁻¹)	σ (mm.s ⁻¹)	σ_L (mm.s ⁻¹)	σ_R (mm.s ⁻¹)	θ_D (K)
Fe _D	0.57(2)	1.27(4)	-	0.31(3)	0.27(3)	LT:362(8) HT: 36(2)
Fe _S	0.33(2) ^a	-	0.21(1) ^a - 0.10(3) ^b	-	-	206(2)
Fe _X	0.09(4)	1.42(8)	0.16(5)	-	-	212(7)

Notes:

- i) a) determined from spectra obtained at 348 K, and b) at 633 K.
- ii) LT and HT represent low temperature (300 K - 426 K) and high temperature (450 K - 633 K) ranges, respectively.

4.2.1 Assignment of components

An asymmetric doublet Fe_D with isomer shift 0.57(2) mm.s⁻¹ and quadrupole splitting 1.27(4) mm s⁻¹ dominates the spectra at low temperatures (303–426 K). The large values of the isomer shift and quadrupole splitting obtained for this component indicate that the Fe impurity atoms are located in a highly distorted lattice structure, thus the Fe_D component is assigned to a damage site. The damage site results from radiation damage induced by the ion implantation process.

The single line, Fe_S , is absent at room temperature (RT), however it is observed at 348 K and above, with an isomer shifts of $0.33(2) \text{ mm. s}^{-1}$. There is an increase in the intensity of this component with increasing sample temperature and a corresponding decrease in the Fe fraction in damage sites is observed. The absence of a quadrupole splitting and a positive isomer shift indicate Fe atoms in sites of cubic or tetrahedral symmetry. There are two sites of tetrahedral symmetry in the cubic lattice, substitutional or interstitial site. The Fe_S component is attributed to Fe atoms substituting host In atoms. A similar component was observed by Cesca *et al.* [65] from their implantation studies of Fe in InP. Their results from channelling measurements on the conversion electrons emitted by the radioactive ^{59}Fe probe nuclei, showed that within the temperature range of our measurements the majority of Fe ions were located in substitutional In sites. The increase in fraction of this component with temperature was associated with impurity atoms diffusing from the damage site and other (Fe_X component) site finally residing on In lattice sites.

A low intensity symmetric doublet, Fe_X , with an isomer shift of $0.09(4)$ and large quadruple splitting of $1.42(8) \text{ mm.s}^{-1}$ is observed at 303 K. This component disappears at above 500 K. The presence of a quadrupole splitting shows that this spectral line is not due to Fe ions at sites of tetrahedral symmetry. A similar component has been observed in the $^{57}\text{Mn}^*$ implantation investigations of Si, SiGe, Ge and GaAs materials [33, 34, 66, 67, 68]. In these studies this component was assigned to impurity pairing with element III vacancies (impurity-vacancy complex).

4.2.2 Discussion of hyperfine parameters

The line-width Γ of the components did not vary with temperature in any systematic way. Therefore, it was set to a temperature independent constant value of $0.30(5) \text{ mm.s}^{-1}$ for the temperature range used. The Gaussian broadening σ for the substitutional component showed a systematic trend, decreasing with increasing temperature. The Gaussian broadening for Fe_X was kept constant at $0.16(5) \text{ mm. s}^{-1}$. The broadening for the left and right (σ_L and σ_R) legs of the Fe_D component was kept constant for the entire temperature range (as shown in Table 4.1).

Figure 4.2 shows the temperature dependence of the isomer shift obtained for InP. The figure shows that the isomer shift values for all components follow the second order Doppler shift, except for the damage component Fe_D . The values of the isomer shift for Fe_D followed the second order Doppler shift with different Debye temperatures of 362 (8) K and 236 (2) K in the low and high temperature ranges, respectively. This behavior may be attributed to a change in the neighboring environment of the Fe nuclei located in the damage sites.

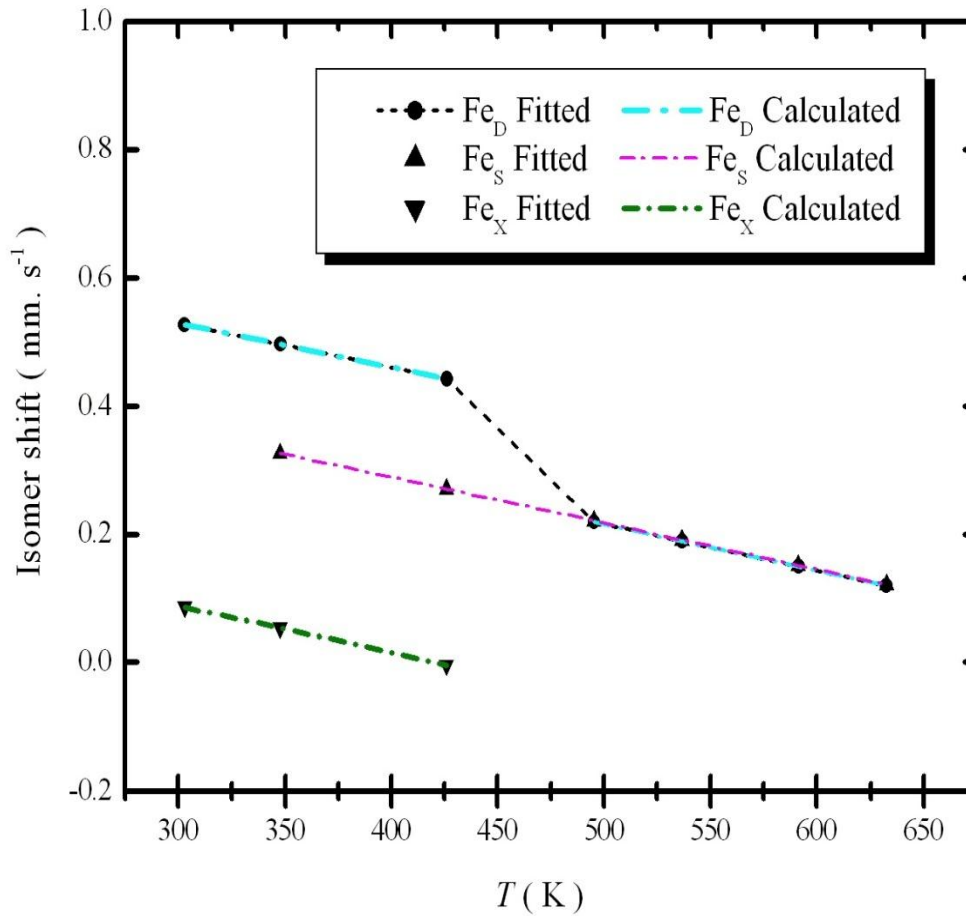


Figure 4.2: Temperature dependence of the isomer shift obtained in ^{57}Fe Mössbauer spectra of InP after $^{57}\text{Mn}^*$ implantation, where the dash lines represent the calculated values and symbols represent the results extracted from fits.

The large positive isomer shift $0.57(2) \text{ mm}\cdot\text{s}^{-1}$ of the damage component indicates an effective low s-electron density around the probe Fe atoms. It should be noted that the isomer shift values for the damage site for the InP spectra are approximately the same as for the substitutional site at temperature $>500 \text{ K}$. This suggests the diffusion of Fe impurity atoms to damaged substitutional sites. The isomer shift of $0.09(4) \text{ mm}\cdot\text{s}^{-1}$ for the Fe_X component in InP at low temperatures ranging from 303 to 326 K are also small but positive, suggesting a small reduction in the s-electron density at the nuclear probe.

Figure 4.3 shows the temperature dependence of the electric quadrupole splitting (ΔE_D) for the Fe_D and Fe_X components in InP, where the quadrupole splitting are plotted against $T^{3/2}$. The quadrupole splitting values for the Fe_D component show weak temperature dependence at higher temperatures (above 400 K). This variation can be attributed to a highly distorted structure near the substitutional site, as many Fe atoms move to In vacancies in the lattice.

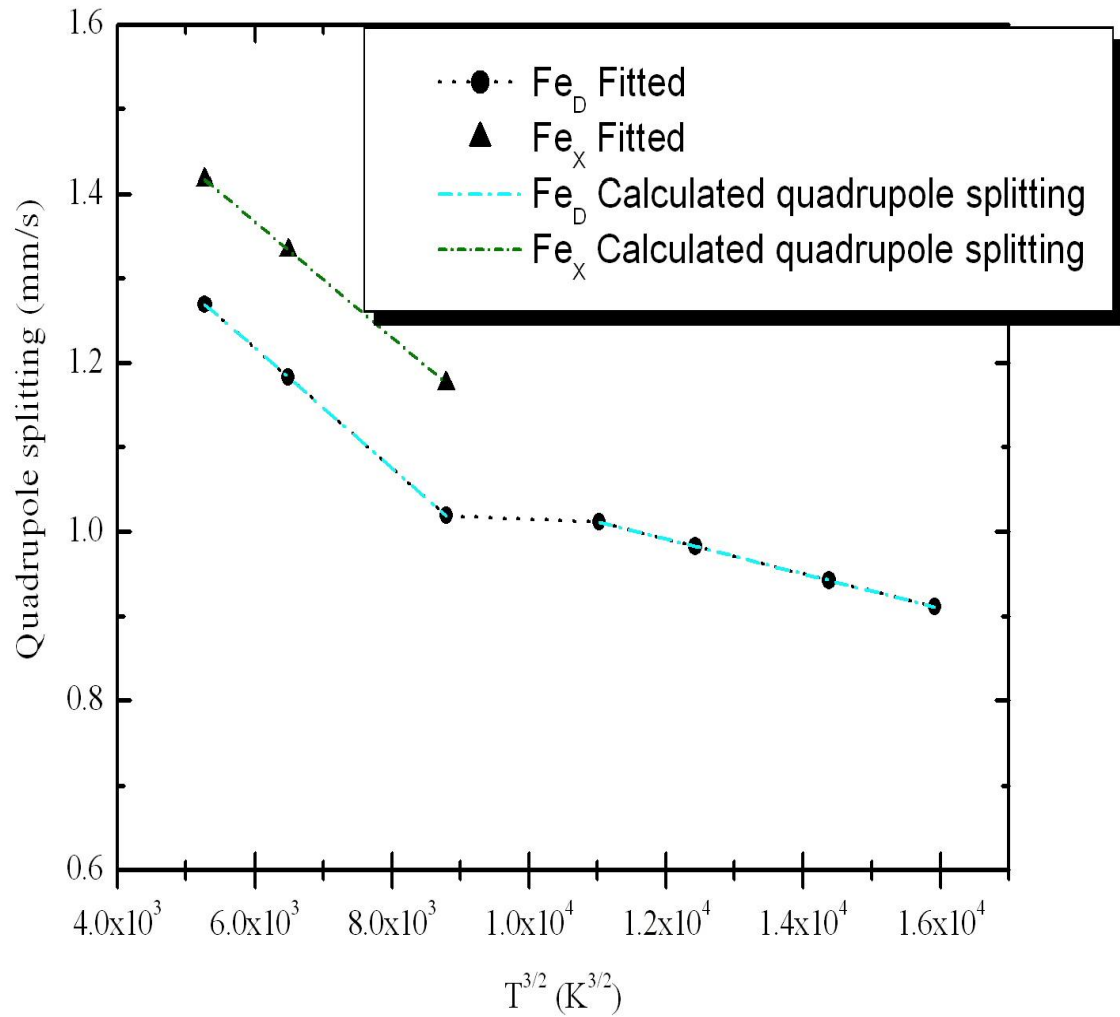


Figure 4.3: Temperature dependence of the quadrupole splitting obtained in ^{57}Fe Mössbauer spectra of InP after $^{57}\text{Mn}^*$ implantation, where the dash lines represent the calculated values and symbols represent the results extracted from fits.

4.2.3 Debye temperatures θ_D of Fe in different lattice sites

The area fractions for all sites were assumed to follow the Debye model [69, 70], which then allows one to determine the Debye temperatures. The extracted Debye temperature value of 206(2) K for the Fe_S component is relatively close to that of the Fe_X component which was determined to be 212(7) K, indicating that these components may be due to Fe in related sites, the first due to substitutional Fe, and the second to Fe in impurity-vacancy complexes.

The theoretical Debye temperature (θ_{eff}) value for Fe_S can be calculated using the mass-defect approximation given by

$$\theta_{\text{eff}} = \left(\frac{M_{\text{h}}}{M_{\text{Fe}}} \right)^{1/2} \left(\frac{\gamma_{\text{Fe-h}}}{\gamma_{\text{h-h}}} \right)^{1/2} \theta_D, \quad (4.1)$$

where M_{h} and M_{Fe} are the masses of the host and the impurity atom, respectively, $\gamma_{\text{Fe-h}}$ and $\gamma_{\text{h-h}}$ are the force constants of the impurity-host and host-host bindings, respectively and θ_D is the Debye temperature of the host material. Nielsen *et al* reported a calculated Debye temperature value of 178 (5) K using the mass-defect model and a Mössbauer experimental Debye temperature value for Sn impurity in In site of InP as 202(6) K [31]. Therefore the average Debye temperature value of 206 (2) K for Fe located in the substitutional site extracted in this work is in agreement with the value obtained by Nielsen *et al* [31].

The Debye temperature values extracted in the low (300 - 426 K) and high temperature ranges (450 - 633 K) for the Fe_D component are 362 (20) K and 236(20) K, respectively. The variation in Debye temperature values of Fe in this site can be explained by the different Fe-P bonds at the elevated temperatures >450 K. Furthermore, the large Debye temperature in the low temperature range suggests stronger Fe-P bonds than at high temperatures.

4.2.4 Annealing of radiation damage

Figure 4.4 shows the site populations of spectral components obtained in the InP sample as a function of implantation temperature. At room temperature, approximately 79% and 21% of impurity atoms are located in the damage sites and impurity-vacancy sites, respectively. The large fraction of impurity atoms in the damage site suggests that there are many P atoms disturbed in their lattice sites. The annealing of the damage is observed above room temperature, where the fraction of the Fe_D component decreases by 5%, and about 4% of Fe atoms substitute the lattice atoms. The fraction of atoms in the substitutional site increases as the sample temperature is increased, rising to 60% at 630 K. The fraction of the Fe_X component remains approximately constant (20%) up to 426 K, but then decreases at temperatures above 426 K until it completely disappears at 537 K. The decrease in this component is associated with the breakdown of the impurity-vacancy complexes, and Fe atoms jump into the substitutional site. Between 537 K and 633 K, the Fe_D component shows a decrease from about 49% to 34%, corresponding to an increase of the Fe_S component by about 12%. Thus, the increase in fraction of impurities in the substitutional site results from a decrease in fractions of the Fe_D , and Fe_X fractions.

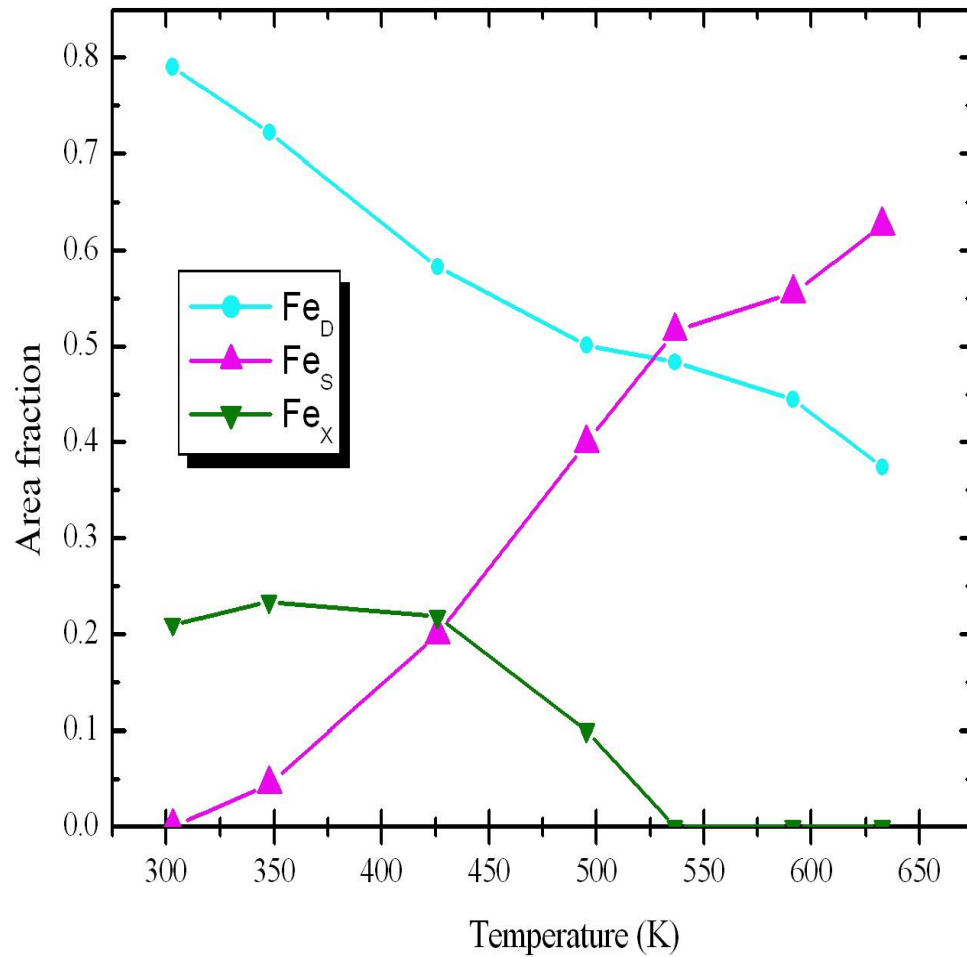


Figure 4.4: Area fractions of components as a function of annealing temperature, observed in the Mössbauer spectra for InP after $^{57}\text{Mn}^*$ implantation.

4.2.5 Summary of $^{57}\text{Mn}/^{57}\text{Fe}$ implanted in InP results

- Three lattice sites are observed, namely; Fe in a damage site (Fe_D) resulting from the radiation induced damage, Fe at a substitutional site (Fe_S) where Fe atoms substitute In lattice atoms and Fe in impurity-vacancy complexes (Fe_X), where Fe atoms pair with In vacancies.
- The large positive isomer shift of 0.57 (2) mm. s^{-1} for the damage site indicates a lower electron density around the Fe nucleus in this site than for other sites.
- The Fe impurities in the damage site form stronger bonds with P atoms compared with Fe impurities in other sites. This is supported by the large Debye temperature values extracted for the damage sites.
- An increase in the fraction of Fe atoms at substitutional sites with temperature is associated with an annealing of lattice damage which resulted from the ion implantation process.

4.3 Data analysis of the n-type InAs and p-type InAs

Figures 4.5 and 4.6 show Mössbauer spectra measured for single crystal samples of n-type InAs and p-type InAs, respectively. The same model and components used to fit the of InP data were applied for this analysis, namely an asymmetric doublet (Fe_D) which dominates the spectra at low temperatures (303 – 448 K); (ii) a single line (Fe_S) which dominates the spectra at high temperatures > 448 K and (iii) a low intensity symmetric doublet.

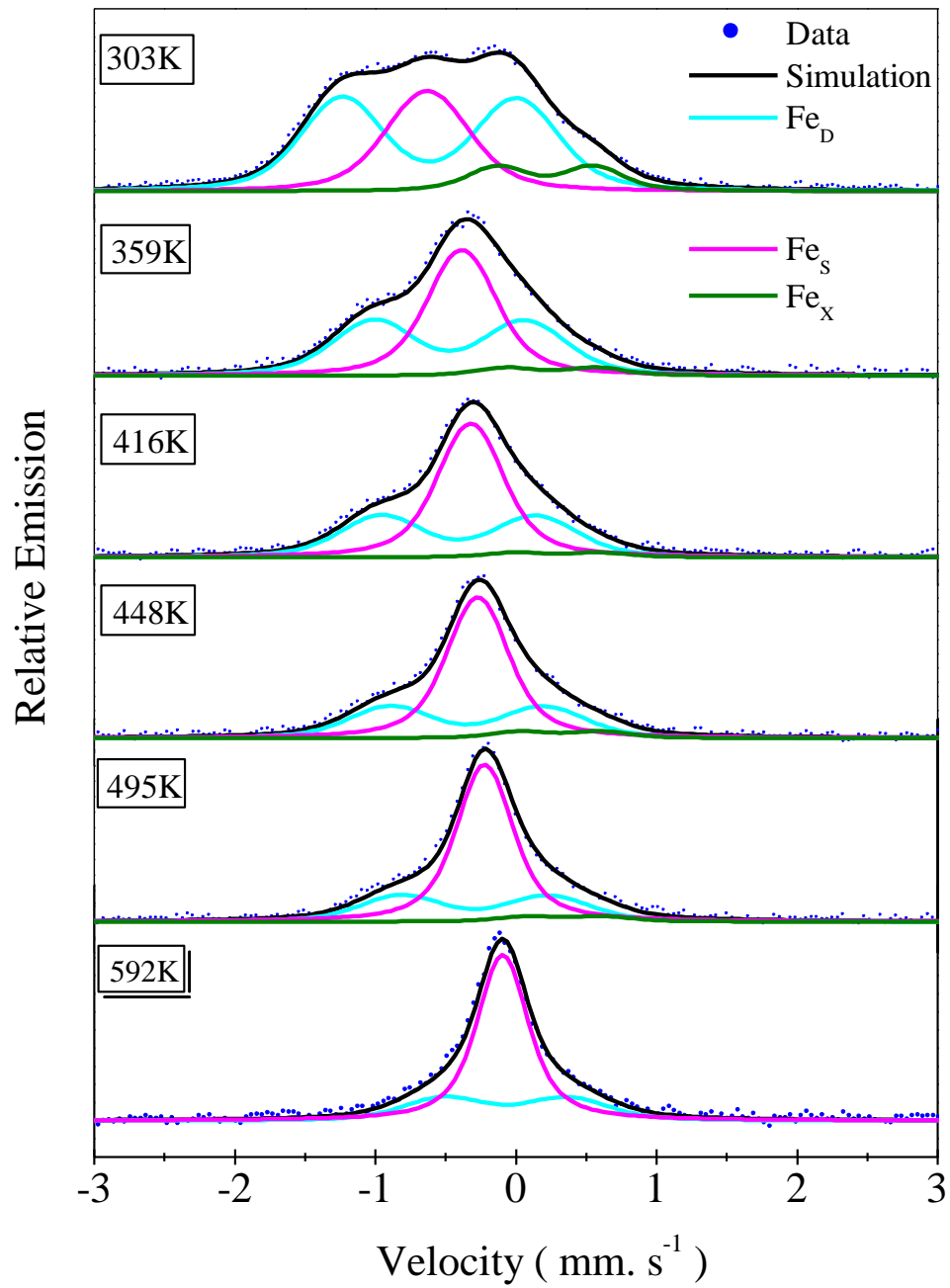


Figure 4.5: Mössbauer spectra of n-type InAs at temperatures indicated after implantation of $^{57}\text{Mn}^+$ ions.

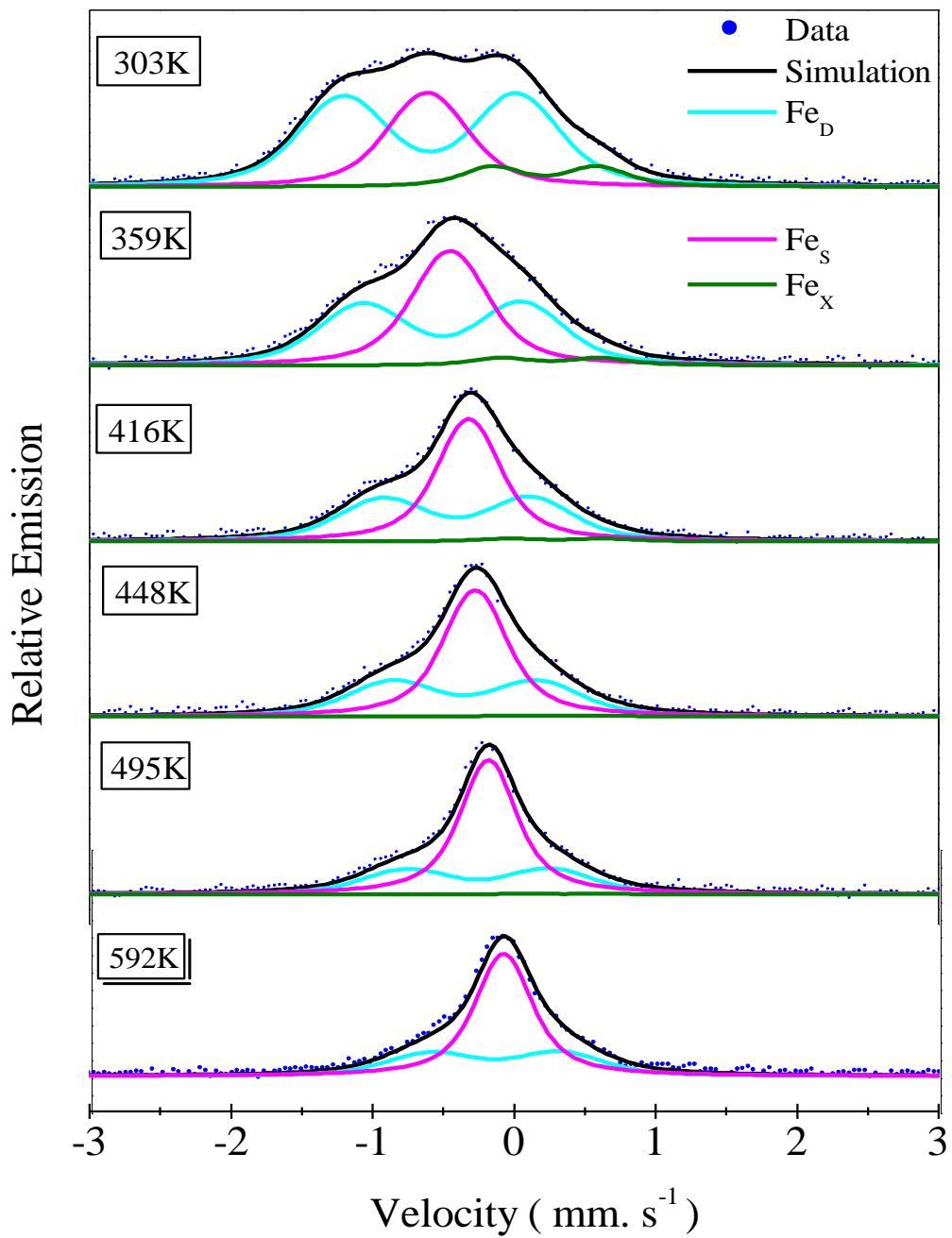


Figure 4.6: Mössbauer spectra of p-type InAs obtained at temperatures indicated after implantation of $^{57}\text{Mn}^*$ ions.

The obtained Mössbauer parameters and extracted Debye temperatures are presented in Table 4.2, below. The behavior of the hyperfine parameters of the three components was similar to those determined for the InP data. Therefore, the same lattice assignments were made for n-type InAs and p-type InAs as in InP.

An asymmetric doublet is assigned to Fe impurity atom in the damage resulting from the radiation induced damage. This component dominates the spectra in the temperature range 303 to 416 K. A single line dominates the spectra at temperatures above 416 K. This site is assigned to Fe impurity atoms located in the In substitutional site. A weak symmetric doublet component is assigned to Fe impurity atoms forming impurity-vacancy complexes. This component disappears at temperatures above 495 K.

Table 4.2: Hyperfine parameters isomer shift (δ) and quadrupole splitting (ΔE_Q), the Gaussian broadening (σ) obtained at room temperature from a simultaneous analysis of the spectra for n- and p-type InAs, and the extracted Debye temperatures (θ_D) for the different lattice sites and errors in parentheses.

	Component	δ (mm. s ⁻¹)	ΔE_Q (mm. s ⁻¹)	σ (mm. s ⁻¹)	σ_L (mm. s ⁻¹)	σ_R (mm. s ⁻¹)	θ_D (K)
n- InAs	Fe _D	0.62(3)	1.22(6)	-	0.24(4)	0.25(5)	177(3)
	Fe _S	0.61(4)	-	0.25(4)- 0.11(4) ^c	-	-	187(3)
	Fe _X	-0.29(4)	0.65(2)	0.15(2)	-	-	175(2)
p-InAs	Fe _D	0.62(3)	1.17(7)	-	0.22(6)	0.23(6)	184(3)
	Fe _S	0.61(4)	-	0.22(5)-0.14(5) ^c	-	-	188(3)
	Fe _X	-0.30(2)	0.49(2)	0.15(1)	-	-	177(2)

Note:

iii) ^c determined from spectra obtained at 592 K.

4.3.1 Discussion of hyperfine parameters

For the entire temperature range the line width Γ of the components was kept constant at $0.27(7) \text{ mm. s}^{-1}$ and $0.32(8) \text{ mm. s}^{-1}$, in both n- and p-type InAs, respectively. The Gaussian broadening (σ) of the Fe_S component decreases dramatically with increasing temperature, see Table 4.2. Figures 4.7 and 4.8 represent the temperature dependence of the isomer shift obtained for n- and p-type InAs, respectively. The values of the isomer shift for the Fe_X component follows the second-order Doppler shift; but for both Fe_D and Fe_S vary in the low temperature (303 – 359 K) and high temperature (495 – 592 K) intervals.

At low (303 K) and high (592 K) temperatures, the isomer shift values for Fe_D and Fe_S components are the same. This suggests that both components are associated with Fe probe nuclei at or near substitutional sites, Fe_S in essentially defect free sites and Fe_D in sites with extended lattice damage, with a larger fraction in damage sites in the earlier stages of the implantation.

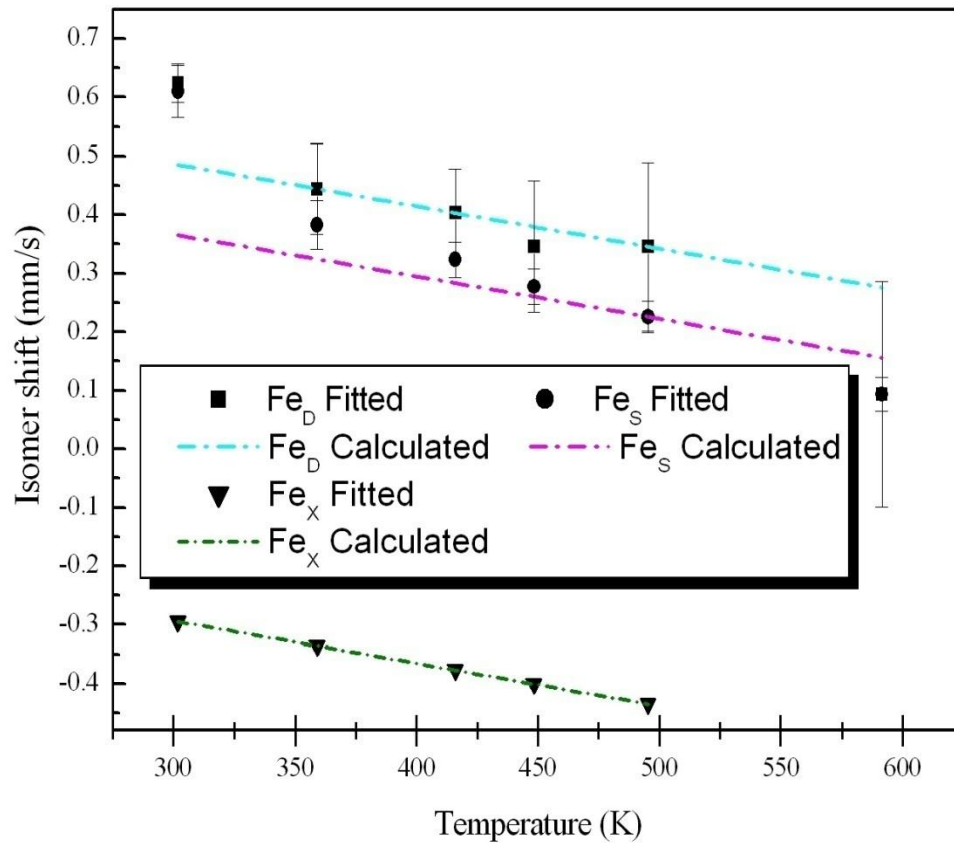


Figure 4.7: Temperature dependence of the isomer shift obtained in ^{57}Fe Mössbauer spectra of n-type InAs after $^{57}\text{Mn}^*$ implantation, where the dashed lines represent the calculated values and symbols indicates the results extracted from fits.

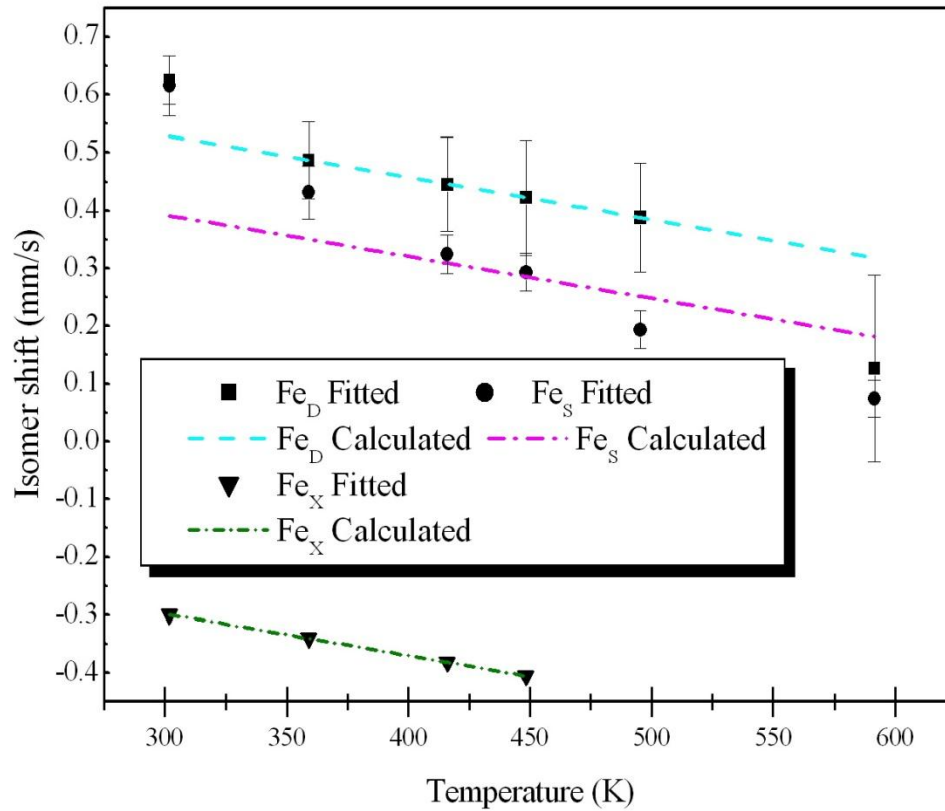


Figure 4.8: Temperature dependence of the isomer shift obtained in ^{57}Fe Mössbauer spectra of p-type InAs after $^{57}\text{Mn}^*$ implantation, where the dashed lines represent the calculated values and symbols indicates the results extracted from fits.

The variations of the quadrupole splitting with temperature for the damage site and impurity-vacancy complex site for n-type InAs and p-type InAs are illustrated in Figures 4.9 and 4.10, respectively, where ΔE_Q is plotted against $T^{3/2}$. The large values of the quadrupole splitting for the damage site could be attributed to a highly distorted environment.

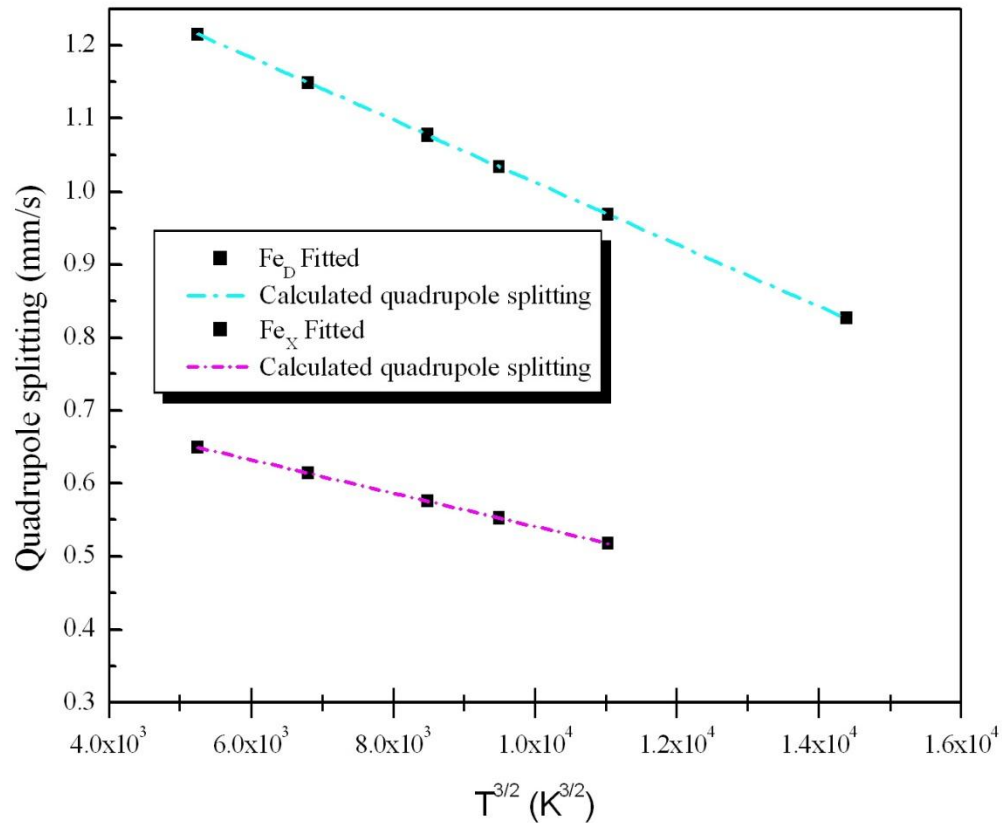


Figure 4.9: Temperature dependence of the quadrupole splitting obtained in ^{57}Fe Mössbauer spectra of n-InAs after $^{57}\text{Mn}^*$ implantation, where lines represent the calculated values and symbols represent the results extracted from fits.

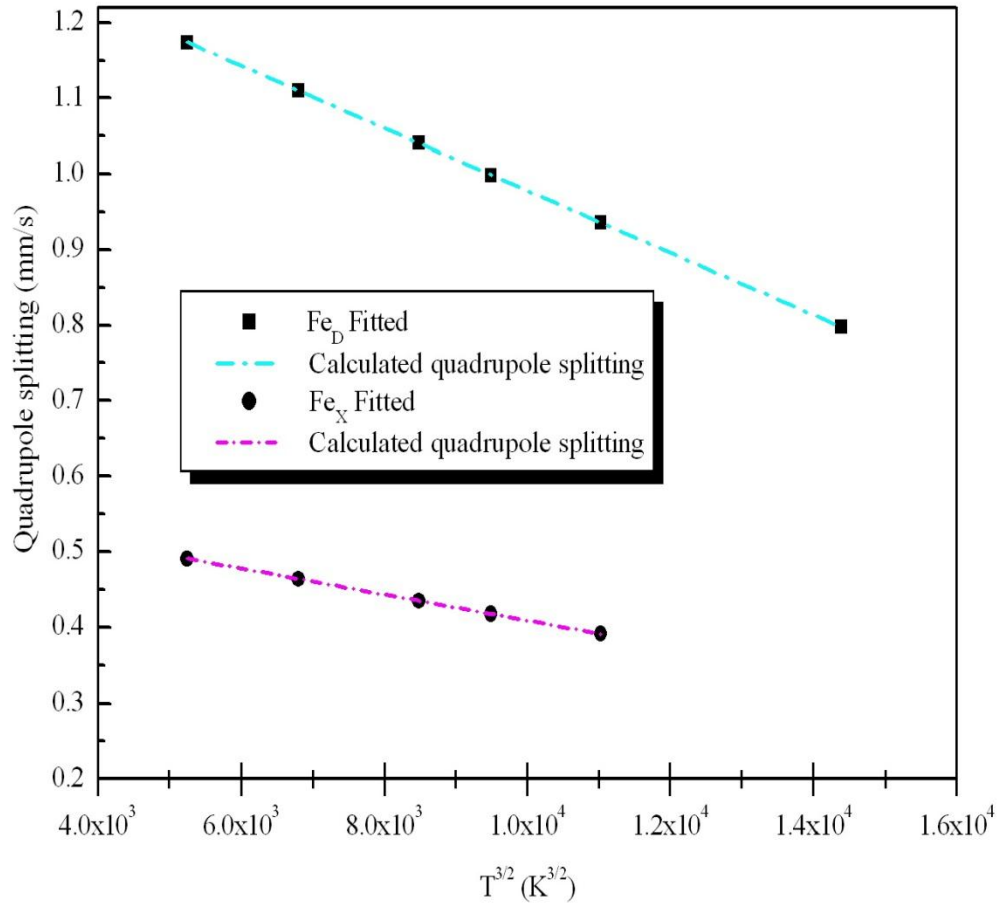


Figure 4.10: Temperature dependence of the quadrupole splitting obtained in ^{57}Fe Mössbauer spectra of p-InAs after $^{57}\text{Mn}^*$ implantation, where the dashed lines represent the calculated values and symbols represent the results extracted from fits.

4.3.1.1 The annealing behavior of the damage in n-type InAs and p-type InAs

Figure 4.11 shows the site populations of the spectral components obtained in n-type InAs sample as a function of implantation temperature. The annealing of the damage site is observed between 300 K and 425 K. In this temperature range the fraction of the Fe_D component decreases by 10% while Fe_X decreases by 8%. The decrease of these components leads to an increase in the Fe_S component from 31% to 49%. The damage anneals again within the temperature range 495 K to 592 K, where the fraction of Fe_D is approximately constant (30%), while Fe_S increases by approximately 5%. The Fe_X component disappears at 592 K.

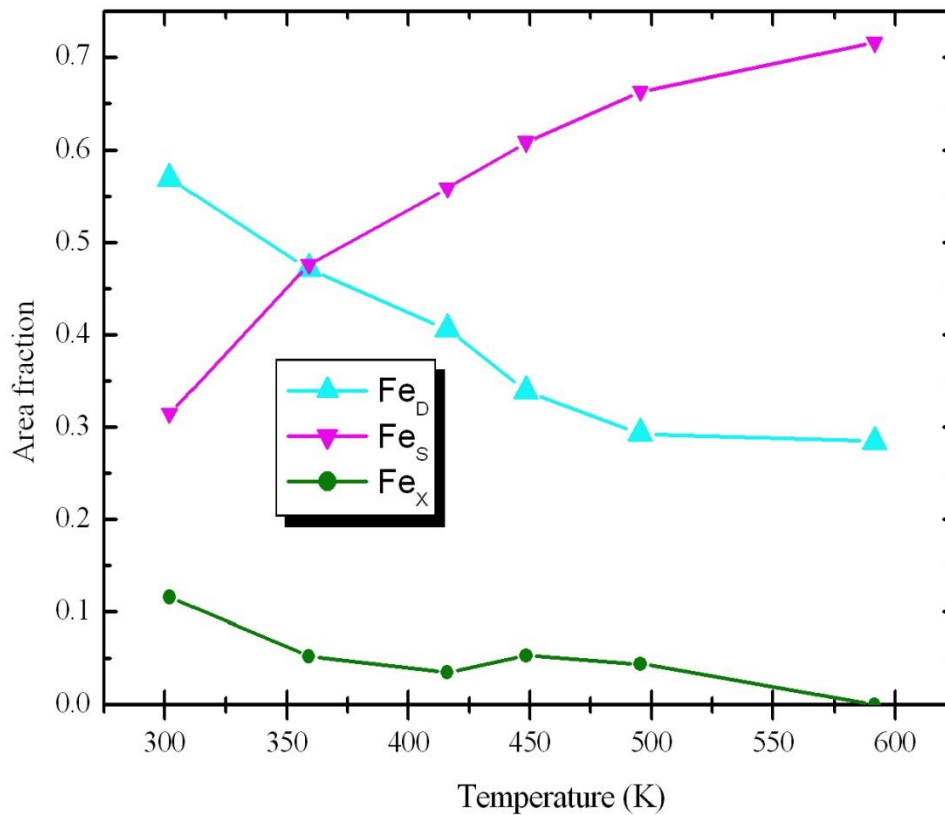


Figure 4.11: Area fractions of components as a function of annealing temperature, observed in the Mössbauer spectra for n-type InAs after $^{57}\text{Mn}^*$ implantation.

In the p-type InAs material, the annealing of damage is observed between 302 K and 495 K, as illustrated in Figure 4.12: the Fe_D component decreases from 60% to 30% and the fraction of the Fe_X component decreases from 11% to 7%. The decrease in Fe_X and Fe_D fractions leads to an increase in the Fe_S fraction by approximately 34%. Above 495 K, the fraction of Fe_D is approximately constant at 30%, while the fraction of Fe_X completely disappears. The fraction of Fe_S increases to approximately 73% at 592 K.

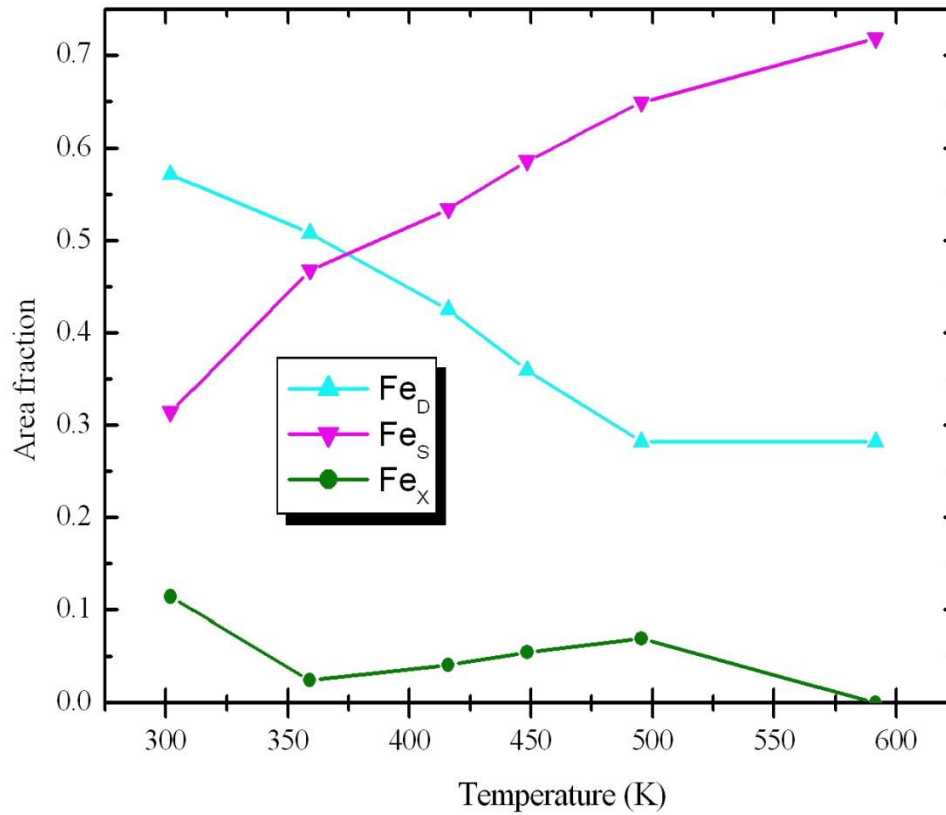


Figure 4.12: Area fractions of components as a function of annealing temperature, observed in the Mössbauer spectra for p-type InAs after $^{57}\text{Mn}^*$ implantation.

4.4 Electronic charge states of iron in different sites

The values of the isomer shift can be used to determine electronic charge states of Fe in different lattice sites. Figure 4.13 shows values of isomer shift plotted against values of quadrupole splitting. The electronic charge states of Fe within different ranges of the isomer shift and quadrupole splitting are indicated. The relationship between isomer shift and quadrupole splitting values was extracted from the Mossbauer Spectroscopy data base [71].

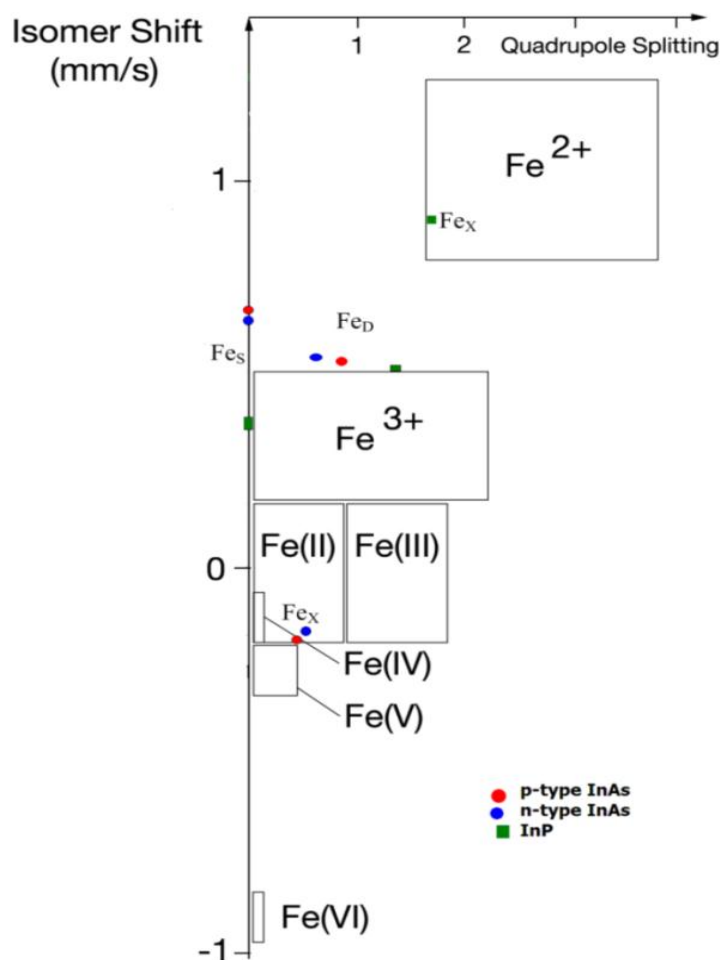


Figure 4.13: The isomer shifts against the quadrupole splitting values for each spectral component obtained from the Mössbauer spectra for InP, n-type InAs and p-type InAs, modified from the Mössbauer data [71].

The isomer shift for Fe ions in the damage site are consistent with near trivalent state (Fe^{3+} with d^5 electron configuration). This may have resulted due to the location of the damage site not being at an original cubic lattice site. The isomer shift value for Fe at substitutional sites is positive but relatively small in the InP sample suggesting a larger s-electron density at the probe nuclei, and that the Fe ions in this site have Fe^{3+} electronic charge state. However, the isomer shift values for n- and p-type InAs are larger than that for InP, indicating a $\text{Fe}^{2+}/\text{Fe}^{3+}$ mix, but nearer the Fe^{3+} charge state. The component Fe_X is assigned high spin Fe^{+2} ($3d^6$) species from the values of the isomer shift and quadrupole splitting for all materials.

4.5 Comparison of the damage recovery

Figure 4.14 shows the annealing behavior of the implantation induced damage in n- and p-type InAs and InP samples. The InP lattice is highly damaged after Fe ion implantation at room temperature compared to both n- and p-type InAs lattices. Furthermore, the recovery of the radiation damage is faster in n-type InAs and p-type InAs than in InP.

These results confirm the formation of stronger Fe-P bonds in InP than Fe-As bonds in both n-type InAs and p-type InAs. This is also supported by the larger Debye temperatures of all components in InP compared to arsenide samples. Above 500 K, the radiation damage in the arsenide samples shows stability, as the fraction of Fe in the damage site shows small variation. The complete annealing of the damage is not achieved at the highest measured temperature, thus temperatures above 600 K are required for further lattice recovery.

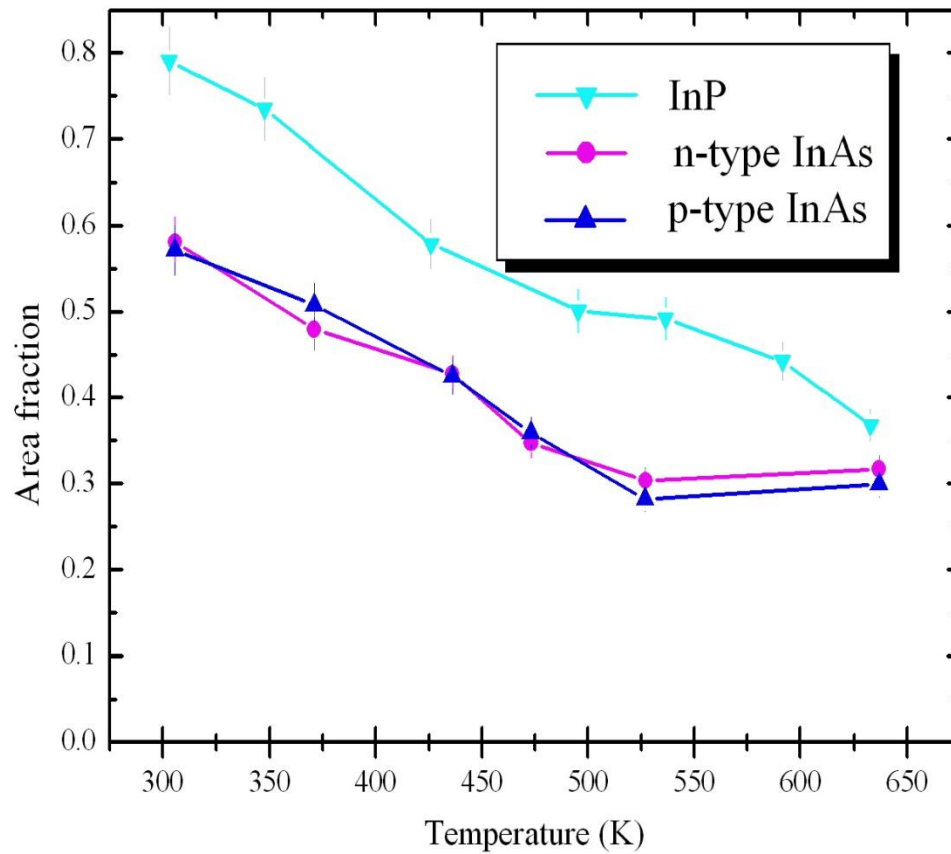


Figure 4.14: Area fractions of Fe_D components as a function of annealing temperature, observed in the Mössbauer spectra for InP, n-type InAs and p-type InAs after $^{57}\text{Mn}^*$ implantation.

The annealing behavior of impurity-vacancy complexes in InP and n- and p-type InAs is presented in Figure 4.15. The results show a larger fraction of the Fe_X component in the phosphide sample than in arsenide samples. W. Wesch *et al.* [72] reported a slow annealing of Frankel-defects at 300 K in InP compared to other III-V compounds, and the differences were assumed to be connected with strong variations of the mobility and annealing of Frankel-defects.

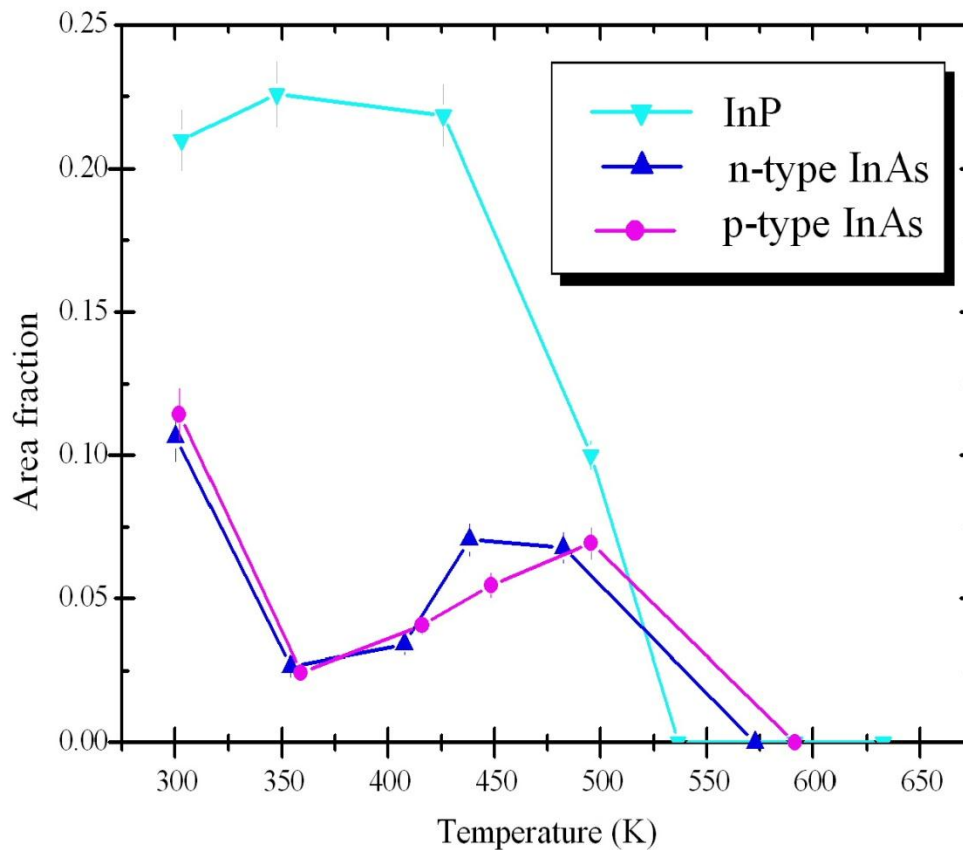


Figure 4.15: Area fractions of Fe_X components as a function of annealing temperature, observed in the Mössbauer spectra for InP, n-type InAs and p-type InAs after $^{57}\text{Mn}^*$ implantation.

The large fraction (~20%) and minor variation of the Fe_x component at low temperatures in InP observed in the present work may be associated with slow mobility of vacancies. This fraction in InP decreases rapidly above 450 K and disappears above 500 K. Therefore, it may be concluded that the breakdown of the impurity-vacancy complexes is achieved more rapidly (i.e. at a lower temperature) in InP than in n-type InAs and p-type InAs.

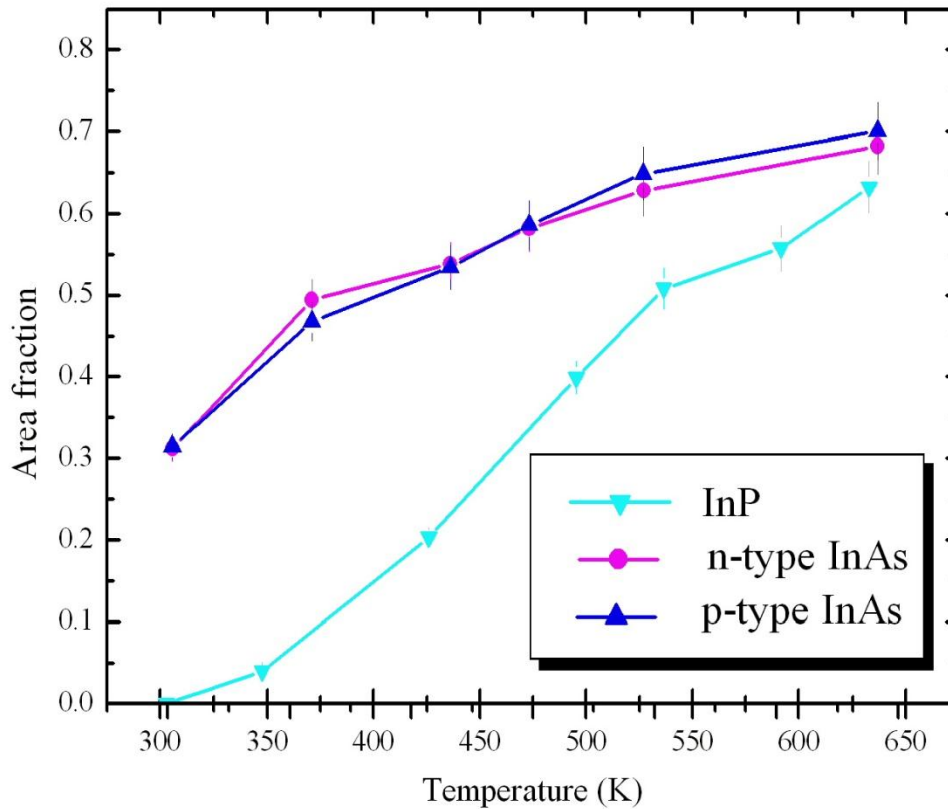


Figure 4.16: Area fractions of Fe_S components as a function of annealing temperature, observed in the Mössbauer spectra for InP, n-type InAs and p-type InAs after $^{57}Mn^*$ implantation.

In InP, the substitutional component is absent at room temperature and is first evident at 338 K, as shown in Figure 4.16. This indicates that the lattice is badly damaged at room temperature (303 K) implantation. The lattice starts to heal with increasing temperature and this additional diffusion from damage sites as well as breakup of the impurity vacancy complex leads to an increase of Fe ions located in Fe_S site at the higher temperatures. In addition, the breakdown of impurity-vacancy complexes also favors the increase in impurity atoms substituting In atoms. The Fe_S fraction increases with temperature for all materials. The Fe_S fraction for n-type InAs is larger (~72%) compared to other samples at the highest measured temperature. This is supported by the quick recovery (at lower temperature) of the damage in n-type InAs.

CHAPTER 5

5.1 Conclusion and Outlook

The main purpose of this work was concerned with the study of lattice sites and complexes formed in III-V compound semiconductors n-type InAs and p-type InAs and InP after implantation with ^{57}Mn ions, using Mössbauer spectroscopy. The radioactive ^{57}Mn nucleus decays to the 14.4 keV Mössbauer state in ^{57}Fe nuclei. Therefore, ^{57}Fe Mössbauer spectroscopy has been employed to yield information on the lattice sites of the probe ions and annealing of implantation induced lattice damage. The Mössbauer hyperfine parameters, particularly isomer shifts and quadrupole splitting are useful tools to assign lattice locations of Fe impurities, study lattice damage and complex formation, and the charge states of Fe impurities in different sites.

The Mössbauer measurements have been conducted on single crystal III-V semiconductors InP, n-type InAs and p-type InAs implanted with low fluencies (up to 2×10^{12} ions/cm²) $^{57}\text{Mn}^*$ ions, over a temperature range 300 – 630 K. The spectra have been analyzed in terms of three components, a single line assigned to Fe at substitutional III sites, a doublet to Fe in regions of extensive defect in the lattice, and a weaker doublet to contributions from Fe-In vacancy complexes. The isomer shift and the quadrupole splitting values suggest different charge states of Fe impurities in different sites, near Fe^{3+} for Fe atoms in distorted environments, Fe^{3+} in In substitutional lattice site and Fe^{2+} in Fe-In vacancy complexes.

The Debye temperatures extracted for Fe ions in In substitutional sites are 206(2) K, 187 (3) K and 188 (3) K, for InP, n- and p-type InAs, respectively. These values are closely related to the Debye temperature of 202 (6) K extracted by Nielsen *et al.* [31] from Mössbauer measurements after Sn ion implantation into InP. Two different Debye temperature values of 362 (8) K and 236(2) K were extracted at low (300 – 426 K) and high (450 – 633 K) temperature intervals, respectively for Fe ions located in damage sites for the InP material. This variation in Debye temperature values of Fe in this site suggests different Fe-P bonds at elevated temperature. The large Debye temperature in the low temperature range suggests stronger Fe-P bonds than in the

high temperature range. However, the Debye temperatures for Fe in the distorted structure in n-type InAs and p-type InAs are 177(3) K and 184(3) K, respectively, for all temperature ranges. The Debye temperatures for Fe impurity atoms forming impurity-vacancy complexes are 212(7) K, 175(2) K and 177(2) K for InP, n-type InAs and p-type InAs samples, respectively. The larger Debye temperature values of Fe-vacancy complexes in InP compared with n-type InAs and p-type InAs suggests stronger Fe-vacancy bonds form in InP. The higher Debye temperature values for the different sites in InP compared to n-type InAs and p-type InAs suggests stronger Fe-P bonds than Fe-As. These results are consistent with those of Masenda *et al.* [22, 68] after ^{57}Mn ion implantation into GaP and GaAs.

These studies together with those undertaken by Masenda [22] show that

- i) the implantation process produces more damage in the phosphide samples (80% at RT) compared to the arsenide samples (60% at RT),
- ii) the damage anneals more rapidly in the phosphide samples and that fractions of up to 70% in essentially defect free substitutional sites can be achieved after annealing at 600 K,
- iii) the damage in the arsenide samples anneal up to 500 K; but remain unchanged at higher temperatures,
- iv) the Fe-P bonds appear to be stronger than the Fe-As bonds as reflected by the higher Debye temperatures determined for the Fe-P defect component in both InP and GaP.

It would be interesting to study the same materials with a complimentary technique such as emission channeling (EC) which allows the direct determination of lattice sites of radioactive impurity ions, incorporated into single crystalline solids. The channeling effects on conversion electrons or α -particles emitted from radioactive impurities are measured along different crystal axes and planes. The lattice sites of the emitting atoms can be determined from the measured anisotropic emission distributions. This method also provides information on the diffusion

behavior and the defect interaction of impurities. This technique has been employed to study Fe impurity atoms implanted into Si, Ge, SiC and diamond [73].

References

- [1] S.S. Li, in *Semiconductor Physical Electronics 2nd Edition* (Springer Science & Business Media, New York, 2006) pg 458-460, 1613-1617.
- [2] H. Andreasen, S. Damgaard, J. W. Petersen and G. Weyer, *Journal Physics F: Metal Physics* **13** (1983) 2077-2088.
- [3] C. Liu, Y. Li, Y. Zeng, *Engineering* **2** (2010) 617-624.
- [4] N.W. Ashcroft and N.D. Mermin, in *Solid State Physics* (Saunders, Harcourt, 1976) pg 387-389.
- [5] D.A. Neamen, in *Semiconductor Physics and Devices-Basic Principles*, IRWIN, (United State of America 1992), pg 15-21.
- [6] R. Turton, in *The Physics of Solids*, (Oxford University Press, New York, 2000), pg 129.
- [7] W.C. Dautremont-Smith, R.J. McCoy, R.H. Burton, *AT & T Technical Journal* **68** (1989) 53-63.
- [8] A. Kumar, P.S. Dutta, *Journal of Crystal Growth* **310** (2008)1647–1651.
- [9] C. Kittel, in *Introduction to Solid State Physics 7th edition* (John Wiley & Sons, New York, 1996), pg 221.
- [10] M. Bosi and C. Pelosi, *Progress in photovoltaics: Research and Applications*, **15** (2007) 51-68.
- [11] J. Singh, in *Electronic and Optoelectronic Properties of Semiconductor Structures*, (Cambridge University Press, 2003), pg 2-5.
- [12] Q.A.H. Naser, H.W. Hilou, A.F. Abdulkader, *SECS International Colloquium on Computing, Communication, Control, and Management* (2009) **373-378**.

-
- [13] O. Sadahura, Yokagawa, *Technical Report English Edition* no.34 (2002).
- [14] H. Ohno, *Science* **281** (1998) 951-56.
- [15] S.A. Wolf, D.D. Awschalom, R.A. Buhrman, J.M. Daughton, S. von Molnar, M.L. Roukes, A.Y. Chtchelkanova, D. M. Treger, *Magnetism and Materials* **294** (2001) 1488-1494.
- [16] M.N. Baibich, J.M. Broto, A. Fert, F. Nguyen Van Dau and F. Petroff, *Physical Review Letters*, **61** (1988) 2472-2475.
- [17] J. De Boeck, W. Van Roy, J. Das, V. Motsnyi, Z. Liu, L. Lagae, H. Dessen and G. Borghs, *Semiconductor Science Technology* **17** (2002) 342-354.
- [18] A.H. MacDonald, P. Schiffer and N. Samarth, *Natural Materials* **4** (2005) 195-202.
- [19] L. Rubin and J. Poate, *American Institute of Physics* **9** (2003) 12-15.
- [20] G. Dearnaley, *Reports on Progress in Physics* **32** (1969) 405-491.
- [21] J.W. Mayer and L. Eriksson, in *Ion Implantation in Semiconductors* (Academic Press, New York, 1970), pg 10-11, 36.
- [22] H. Masenda, MSc. Dissertation, ^{57}Fe Mössbauer investigations in GaAs and GaP following implantation of $^{57}\text{Mn}^*$, University of Witwatersrand (2010).
- [23] A.N. Bagaria, in *Doping by Diffusion & Implantation*, IIT Kharagpur, Indo-German Winter Academy (2006).
- [24] H.P. Gunnlaugsson, T.E. MØlholt, R. Mantovan, H. Masenda, D. Naidoo, W.B. Dlamini, R. Sieleman, K. Bharuth-Ram, G. Weyer, K. Johnston, G. Langouche, S. Ólafsson, H.P. Gislason, Y. Kobayashi, Y. Yoshida and M. Fanciulli, *Applied Physics Letters* **97** (2010), 142-501.
- [25] J.S. Williams, *Material Science and Engineering* **A253** (1998) 8-15.

-
- [26] H.P. Myers, in *Introductory Solid State Physics* (Taylor & Francis, new York, 1990) pg101.
- [27] S. Damgaard, J.W. Petersen and G. Weyer, *Journal of Physics C: Solid State Physics* **14** (1981) 993-1000.
- [28] P. Kringhøj and G. Weyer, *Hyperfine Interactions* **79** (1993) 639-644.
- [29] P. Kringhøj and G. Weyer, *Applied Physics Letters* **62** (1993) 1973-1975.
- [30] N.E. Holm and G. Weyer, *Journal of Physics C: Solid State. Physics* **13** (1980) 1109-1120.
- [31] O.H. Nielsen, F.K. Larsen, S. Damgaard, J.W. Petersen and G. Weyer, *Zeitschrift für Physik B Condensed Matter* **52** (1983) 99-109.
- [32] W. Pfeiffer, M. Deicher, R. Keller, R. Magerle, P. Pross, H. Skudlik, Th. Wichert, H. Wolf, D. Forkel, N. Moriya and R. Kalish, *Applied Surface Science* **50** (1991) 154-158.
- [33] H.P. Gunnlaugsson, M. Fanciulli, M. Dietrich, K. Bharuth-Ram, R. Sielemann, G. Weyer, ISOLDE Collaboration, *Nuclear Instruments and Methods in Physics Research B* **186** (2002) 55-60.
- [34] K. Bharuth-Ram, H.P. Gunnlaugsson, G. Weyer, R. Mantovan, D. Naidoo, R. Sielemann, M. Fanciulli, G. Langouche, S. Olafsson, Th. Aigne, ISOLDE Collaboration, *Hyperfine Interactions* **191** (2009) 115-120.
- [35] M.W. Wanlass, S.P. Ahrenkiel, R.K. Ahrenkiel, D.S. Albin, J.J. Carrella, A. Duda, J. F. Geisz, S. Kurtz, T. Moriarty, R.J. Wehrer and B. Wernsman, Proceedings of *31st IEE Photovoltaics Specialist Conference and Exhibition Lake Buena Vista, Florida*, (2005).
- [36] M. Cooke, *Semiconductor Today Compounds and Advanced Silicon* **4** (2009) 73-77.
- [37] P. Too, S. Ahmed, R. Jakiela, A. Barcz, A. Kozanecki, B. J. Sealy, R. Gwilliam, Proceedings of *11th IEEE International Symposium on Electron devices for Microwave and Optoelectronic Applications* **10** (2003) 18-23.
- [38] R.L. Mössbauer, *Hyperfine Interactions* **126** (2000) 1-12.

-
- [39] S.S. Hanna, *Hyperfine Interactions* **90** (1994) 3-20.
- [40] N.N. Greenwood and T.C. Gibb, in *Mössbauer Spectroscopy*, (Chapman and Hall Ltd, London, 1971), pg 1-67.
- [41] G.K. Wertheim, in *Mössbauer Effect*, (Academic Press INC., New York, 1964), pg 49-82.
- [42] A.G. Maddock, in *Principles and Applications of the techniques*, (Publishing limited, England, 1997).
- [43] J. Danon, in *Lectures on the Mössbauer Effect*, (Gordon and Breach, Sciences Publishers INC., New York, 1968), pg 3 & 6.
- [44] G. Schatz, and A. Weidinger, in *Nuclear Condensed Matter Physics*, (John Wiley & Sons, New York, 1995), pg 33-62.
- [45] U. Köstör, V.N. Fedoseyev, A.N. Andreyev, U.C. Bergmann, R. Catherall, J. Cederkäll, M. Dietrich, H. De Witte, D.V. Fedorov, L. Fraile, S. Franchoo, H. Fynbo, U. Georg, T. Giles, M. Garska, M. Hannawald, M. Huyse, A. Joinet, O.C. Jonsson, K.L. Kratz, K. Kruglov, Ch. Lau, J. Lettry, V.I. Mishin, M. Oinonen, K. Partes, K. Peräjärvi, B. Pfeiffer, H.L. Ravn, M.D. Seliverstov, P. Thirolf, K. Van de Vel, P. Van Duppen, J. Van, Roosbroeck, L. Weissman, IS365, IS387, and ISOLDE Collaboration, *Nuclear Instruments and Methods in Physics B* **204** (2003) 347-352.
- [46] D. Forkel-Wirth, *Report on Progress in Physics* **62** (1999) 527-597.
- [47] H.H. Bertschat, J.G. Correia, M. Deicher, M. Dietrich, G. Weyer, Th. Wichert, E. Zech *CERN-INTC-2002-006 INTC-O-008* (2002) 1-108
<http://cdsweb.cern.ch/record/536172/files/intc-o-008.pdf>
- [48] G. Weyer and the ISOLDE Collaboration, *Hyperfine Interactions* **129** (2000) 371-390.
- [49] M. Deircher, in *Europhysics news* (May/June 2002) 81-85.
- [50] D. Forkel-Wirth, *The Royal Society* **356** (1998) 2137-2162.

- [51] G. Weyer, Applications of Mössbauer Spectroscopy to Investigations of Defects in Semiconductors, Proceedings the 15th International Conference on Defects in Semiconductors, (1988) CERN-EP/88-149.
- [52] B. Tuch, *Journal Physics D: Applied Physics* **18** (1985) 557-584.
- [53] A.M.E. Alakrimi, PhD Dissertation, ⁵⁷Fe Mössbauer Spectroscopic study of the Spin-glass Transitions in Mixed Spinel Series Mg_{0.9+x}Fe_{2(1-x)}Ni_{0.1}TiO₄, Universitit Gent (2010).
- [54] E. De Grave, R.E. Vandenberghe and C. Dauwe, *Hyperfine Interactions* **161**(2005)147-160.
- [55] G. J. Long and F. Grandjean, in *Mössbauer Spectroscopy Applied to magnetism and Material Science* (Plenum Press, New York, 1996)
- [56] U. Gonser, in *Mössbauer Spectroscopy II (The Exotic Side of the Method)* (Springer, Germany, 1981), pg 140-149.
- [57] C. John, 2004, Radioactive ion beam Facility in Europe: Current status and Future Development, Proceedings 17th International Conference on Cyclotrons 2004 and their Applications (October 2004, Tokyo, Japan).
- [58] V.N. Fedoseyev, K. Bätzner, R. Catherall, A.H.M. Evensen, D. Forkel-Wirth, O.C. Jonsson, E. Kugler, J. Lettry, V.I. Mishin, H. L. Ravn, G. Weyer, the ISOLDE Collaboration., *Nuclear Instruments and Methods in Physics B* **126** (1997) 88-91.
- [59] R. Montovan, H.P. Gunnlaugsson, G. Weyer, R. Sielemann, D. Naidoo, K. Bharuth-Ram, S. Ólafsson, G. Langouche, K. Johnston, *CERN INTC-2006-005, INTC-P-203*.
- [60] T. Saito, Y. Kobayashi, M.K. Kubo, Y. Yamada, *Journal of Radioanalytical and nuclear chemistry* **255** (2003) 519-522.
- [61] S.S. Kapoor and V.S. Ramamurthy, in *Nuclear Radiation Detectors*, New Age International (P) Ltd Publishers, New Delhi,1986)) pg **76-78**.
- [62] Wikipedia, 21 May 2005, [Ferromagnetism](#) .

-
- [63] M.G. Javie and S.L. Campbell, in *Mössbauer Spectroscopy*, (Massachusetts Institute of Technology 2006), http://web.mit.edu/woodson/Public/8.14finalpapers/Duarte_mossbauer.pdf.
- [64] H.P. Gunnlaugsson, *Hyperfine Interactions* **167** (2006) 851-854.
- [65] T. Cesca, A. Verna, G. Mattei, A. Gasparotto, B. Fraboni, G. Impellizeri and F. Priolo, *Journal of Applied Physics* **100** (2006) 023539.
- [66] H.P. Gunnlaugsson, G. Weyer, M. Dietrich, M. Fanciulli, K. Bharuth-Ram, R. Sielemann, the ISOLDE Collaboration, 2003 *Physica B: Condensed Matter* **340-342** (2003) 537-540.
- [67] D. Naidoo, H.P. Gunnlaugsson, K. Bharuth-Ram, V.V. Naicker, G. Weyer, R. Sielemann, R. Mantovan, M. Fanciulli, the ISOLDE Collaboration, *Hyperfine Interactions* **188** (2009), 11-17.
- [68] H. Masenda, D. Naidoo, K. Bharuth-Ram, H.P. Gunnlaugsson, G. Weyer, W.B. Dlamini, R. Mantovan, R. Sielemann, M. Fanciulli, T. E. MØlholt, S. Ólafsson, G. Langouche, K. Johnston, Collaboration ISOLDE, *Hyperfine Interactions* **198** (2010) 15-22.
- [69] E. Kuzmann, S. Nagy, and A. Vertes, *Pure Applied Chemistry*, IUPAC, **75** (2003) 801-858.
- [70] D.G. Rancourt & J.Y. Ping, *Nuclear Instruments and Methods in Physics Research B*, **58** (1991) 85-97.
- [71] Mössbauer Effect Data Center, <http://orgs.unca.edu/medc/Resourcesisotopes/Resource-Fe.html>.
- [72] W. Wesch, *Nuclear Instruments and Methods in Physics Research Section B*, **68**(1992) 342-354.
- [73] D. Naidoo, PhD Dissertation, Mössbauer investigations in diamond, SiGe and Ge single crystals following ion implantation of ^{57}Fe and $^{57}\text{Mn}^*$, University of KwaZulu-Natal (2005).